Regional variability and turbulent characteristics of the satellite-sensed submesoscale surface chlorophyll concentrations

Eun Ae Lee[1] **and Sung Yong Kim**[1]

[1]Environmental Fluid Mechanics Laboratory, Department of Mechanical Engineering,
Korea Advanced Institute of Science and Technology,
291 Daehak-ro, Yuseong-gu, Daejeon 34141, Republic of Korea

Key Points:

- Remotely-sensed chlorophyll observations off the East/Japan Sea show seasonal blooms in spring and fall within 250 km from the coast.
- Kinetic energy spectra of submesoscale chlorophyll observations show regimes of the forward and inverse cascades and surface dissipation.
- Nearcoast chlorophyll blooms are correlated with submesoscale horizontal shear, vortical phenomena, and their cross-shore propagations.

Corresponding author: Sung Yong Kim, syongkim@kaist.ac.kr

Abstract

The regional variability and turbulent characteristics of submesoscale surface chlorophyll concentrations are examined with hourly maps of geostationary ocean color imagery-derived chlorophyll concentrations at a 0.5-km resolution for a period of five years (2011 to 2015) over the East/Japan Sea with concurrent mesoscale and submesoscale observations. Two seasonal blooms occur in the spring and fall within 250 km off the coast that are associated with constructive combinations of light exposure, nutrients, and vertical stratification. Another bloom occurs in the summer and is closely related to regional wind-driven upwelling events. The spring and fall blooms are more significant near the coast (within 40 km from the coast) than offshore because of the more energetic submesoscale horizontal shear and vortical phenomena onshore as well as their propagation in the cross-shore direction. In addition, the regional spring bloom starts offshore and migrate onshore with a time delay of one month, which may result from the onshore propagation of geostrophic currents, the deepening of the mixed layer, and favorable nutrient fluxes from the subsurface. The wavenumber-domain energy spectra of chlorophyll concentrations exhibit anisotropy, which may be closely related to bathymetric effects and regional circulations. The spectral decay slopes change from $k^{-5/3}$ to k^{-1} at the $O(10)$ km scales and from k^{-1} to $k^{\leq -3}$ at the $O(1)$ km scales and have weak seasonality. These results are consistent with the two-dimensional quasi-geostrophic turbulence theory and can be interpreted with the baroclinic instability energized from the moderate seasonal mixed layer under mesoscale regional circulations.

1 Introduction

In the assessment of ocean ecosystem productivity, remotely sensed surface chlorophyll concentrations have been used as a proxy for phytoplankton biomass and primary production in the ocean upper layer [e.g., *Falkowski et al.* [1998]; *McGillicuddy et al.* [1998]; *Behrenfeld et al.* [2005]; *McGillicuddy et al.* [2007]]. The timings of phytoplankton blooms in the upper ocean depend on the light, nutrients, and vertical stratification within the water column. In subtropical regions (or mid-latitudes of 20°N/S to 40°N/S), the phytoplankton blooms typically occur twice a year, in the spring and fall, in the coastal regions and once a year, in the spring, in the open ocean [e.g., *Townsend et al.* [1994]; *Winder and Cloern* [2010]; *Wilson and Coles* [2005]; *Chiswell et al.* [2013]; *Sigler et al.* [2014]]. Specifically, the light- and nutrient-rich conditions of a well-mixed water column lead to spring phytoplankton blooms. Then, the spring blooms end due to limited nutrients and the increased grazing pressure of the higher trophic levels in the summer. In the fall, the enhanced vertical mixing of nutrients due to episodic storm events and a deepening of the mixed layer, i.e., reduced stratification, initiate the fall phytoplankton bloom. Then, the phytoplankton becomes light-limited due to the decrease in daylight and the mixed layer becomes deeper in the winter [e.g., *Michaelsen et al.* [1988]; *Mann and Lazier* [2013]; *Chiswell et al.* [2013]; *Smith et al.* [2016]]. In addition, the long-term trends and inter-annual climate variability [e.g., *Boyce et al.* [2010]; *Rykaczewski and Dunne* [2011]], submesoscale eddies and fronts [e.g., *Mahadevan and Tandon* [2006]; *Taylor and Ferrari* [2011b]; *Omand et al.* [2015]; *McWilliams* [2016]] as well as turbulent convection [e.g., *Taylor and Ferrari* [2011a]] have been investigated as the main physical drivers of the phytoplankton blooms. For instance, *Joo et al.* [2015] reported long-term chlorophyll variability in the East/Japan Sea (EJS) based on Moderate Resolution Imaging Spectroradiometer (MODIS) observations.

Submesoscale processes, defined as geostrophic turbulence characterized by the $O(1)$ Rossby and Richardson numbers and a horizontal scale smaller than the first baroclinic Rossby deformation radius [e.g., *Thomas et al.* [2008]; *McWilliams* [2016]], have drawn attention in the oceanographic community due to their importance and contributions to the vertical transports of oceanic tracers in the upper ocean. These submesoscale processes have been further investigated with numerical simulations with advances in computing resources as well as with observations from new instruments capable of high temporal and spatial resolutions [e.g., $O(1)$ hour and $O(1)$ km]. The primary drivers of the submesoscale processes have been reported as baroclinic instability in the mixed layer (mixed layer instability), the frontogenesis associated with mesoscale eddies (i.e., strain-induced frontogenesis), turbulent thermal wind, and topographic wakes [e.g., *Callies et al.* [2015]; *McWilliams* [2016]].

In the study of geostrophic turbulence, the spectral decay slopes of the one-dimensional wavenumber domain (k) kinetic energy (KE) spectra of dynamic variables (e.g., currents or density) have been used to identify the theoretical classifications of oceanic turbulent flows [e.g., *Lesieur and Sadourny* [1981]; *Armi and Flament* [1985]; *Soh and Kim* [2018]] (Table 1). The KE spectra of the currents in the quasi-geostrophic (QG), surface QG (sQG), and semi-QG (SG) theories show spectral decay slopes of k^{-3}, $k^{-5/3}$, and $k^{-8/3}$ at the highest wavenumbers, respectively [e.g., *Charney* [1971]; *Blumen* [1978];

Hoskins [1975]] (Table 1). In contrast, the wavenumber domain energy spectra of passive tracers exhibit theoretical slopes of $k^{-5/3}$ for inverse cascades and k^{-1} for forward cascades under the QG theory [e.g., *Kraichnan* [1967]; *Gage* [1979]; *Vallis* [2006]] (Table 1).

Specifically, the wavenumber domain energy spectra of chlorophyll concentrations have been described with spectral decay slopes of k^{-1} for the two-dimensional turbulence [e.g., *Powell and Okubo* [1994]; *Denman et al.* [1977]; *Denman* [1976]; *Franks* [2005]], k^{-2} at a spatial scale of $O(1)$ km [e.g., *Denman and Abbott* [1988]; *Strass* [1992]], and between k^{-1} and k^{-2} based on a numerical simulation and the theory of growing phytoplankton in two-dimensional turbulent flows [e.g., *Holloway* [1986]]. These spectral slopes are valid up to the $O(1)$ km scale and become steeper below that scale ($k^{\leq -3}$). On a large scale, the tracer-variance spectrum asymptotically approaches a decay slope of $k^{-5/3}$ [e.g., *Obukhov* [1968]; *Franks* [2005]; *Vallis* [2006]]. In addition, *Holloway* [1986] reported the cross-shore variations of turbulent characteristics with the spectral decay slopes of k^{-2} in the offshore region and ranging from $k^{-1.5}$ to k^{-2} in the nearshore coastal area as a result of the increased energy inputs at shorter length scales near the coast associated with tidal mixing, interactions with bathymetry, and the rapid growth of phytoplankton in the coastal region.

A primary motivation of this work is to evaluate the feasibility of the use of hourly time series of geostationary ocean color imagery (GOCI)-derived chlorophyll concentration maps for the study of mesoscale and submesoscale processes [e.g., *Lim et al.* [2012]; *McWilliams* [2016]]. Thus, we conducted analyses of (1) the quality assurance and quality control (QAQC) of the chlorophyll data, including statistical analyses based on intrinsic flag definitions and the mapping of the data onto a regular grid using optimal interpolation (see Appendix A:), (2) the regional variability of the chlorophyll concentrations with concurrent observations, and (3) the geophysical turbulent characteristics of the chlorophyll concentrations using their wavenumber domain energy spectra. We chose a coastal area, i.e., Imwon, off the east coast of Korea where submesoscale filaments and eddies are frequently observed and where concurrent observations at the relevant spatial and temporal scales are available (Figure 1) [e.g., *Yoo et al.* [2018]]. In this region, two major regional currents, the North Korea Cold Current (NKCC) and East Korea Warm Current (EKWC), meet, and a regional subpolar front (SPF) forms off the east coast of Korea [e.g., *Min et al.* [2006]; *Kim et al.* [2006]; *Kim and Min* [2008]]. Particularly, concurrent mesoscale and submesoscale observations of the ocean surface and subsurface for a period of at least one year (2013) are available, including high-frequency radar-derived surface currents, chlorophyll concentration maps, seasonal stratification data, and satellite-derived geostrophic current and sea surface temperature (SST) measurements; surface wind data obtained from regional meteorological stations and a meteorological numerical model are also available [see *Yoo et al.* [2018] as a companion paper reporting the primary variances and turbulent characteristics of the surface currents observed in the identical study domain]. There are limitations to describing turbulent characteristics with spectral decay slopes of the energy spectra because physically and dynamically irrelevant fields with identical spectral decay slopes can exist [e.g., *Gower et al.* [1980]; *Armi and Flament* [1985]]. Thus, a set of concurrent observations of the surface currents and chlorophyll concentrations is examined to characterize the geostrophic turbulence [e.g., *Soh and Kim* [2018]]. Additionally, cautionary remarks on the use of chlorophyll concentration data in the analysis of the spectral decay slopes are presented in section 5.1.

This paper is divided into four sections. The datasets used to investigate the primary goals of the paper are described in section 2, including the GOCI-derived chlorophyll; the satellite-derived geostrophic currents and SST; the coastal surface currents; the profiles of the regional temperature, salinity, and nutrients; and the wind stress. The seasonal mixed layer and formulations of the one-dimensional wavenumber-domain energy spectra of chlorophyll concentrations are presented in section 3. Then, the physical conditions and variability related to the seasonal chlorophyll blooms are described in section 4. A discussion and the conclusions of the results follow in sections 5 and 6, respectively.

2 Data

2.1 Study domain

The remotely sampled chlorophyll concentrations in two regions of a coastal area [Imwon (IMW); within 40 km from the shoreline; Figures 1a and 1b] and an open ocean area [South of Ulleungdo (SUL); from 40 to 250 km from the coast; Figures 1a and 1d] off the EJS are analyzed to examine (1) the seasonal variability of chlorophyll concentrations and its potential drivers and (2) the turbulent characteristics of the regional chlorophyll concentrations as one of the observed submesoscale surface concentration datasets (Figure 1a). A map of the GOCI-derived chlorophyll concentrations and close-ups over

IMW and SUL are shown in Figure 1. In the coastal region, hourly high-frequency radar (HFR)-derived surface current maps at a spatial resolution of 1 km are available (a gray contour shows the effective spatial coverage in Figure 1b). The sampling stations of the conductivity-temperature-depth and nutrient profiles are marked for both the coastal and open ocean areas (Line 103 and 104; C0 to C11 stations) (Figures 1b and 1d). The green line (latitude of 37.15°N) is used to examine the temporal variability of the chlorophyll concentrations in the cross-shore direction as well as the variability of the submesoscale surface currents and mesoscale geostrophic currents.

2.2 Remotely sensed surface chlorophyll concentrations

2.2.1 GOCI

Hourly GOCI-derived L2A products, including maps of chlorophyll, the colored dissolved organic matter (CDOM), and the total suspended solid (TSS) concentrations; concentration-derived vector currents; and eight-band images around the Korean Peninsula with a spatial resolution of 0.5 km during daylight hours (e.g., maximum of eight snapshots a day) serve as passive mode observations [e.g., *Choi et al.* [2012]; *Yang et al.* [2014]; *Son et al.* [2015]; *Warren et al.* [2016]]. Figure 2 shows examples of the GOCI-derived chlorophyll concentration maps that capture the seasonal blooms in the spring and fall as well as a bloom due to the upwelling events in the summer. These maps are presented with the concurrently observed AVISO mesoscale geostrophic currents and sea surface height anomalies (SSHAs), SST and seasonal SST anomalies.

The raw GOCI data are subjected to multiple filters and calibrations, including an internal GOCI data processing system (GDPS) [e.g., *Ryu et al.* [2012]]. The L2A products are provided with flags, i.e., the predetermined parameters for the QAQC of the GOCI data (Table 2). Probability density functions (PDFs), presented with log-scaled chlorophyll using flags (Figure 1c), show that the Flag3 L2A chlorophyll product has a nearly Gaussian distribution with a relatively low density of outliers (Figure 1c), which can justify the techniques and analyses adopted in this paper (e.g., the maximum likelihood estimate, the covariance and correlation estimates, and the least-squares fit). The outliers in the chlorophyll concentration data mainly result from (1) errors in the atmospheric corrections and (2) mismatches in the individual wavelength products associated with fast-moving clouds [e.g., *Choi et al.* [2012]] (Figure 1c). Thus, the Flag3 chlorophyll concentration data (GDPS version 1.5) for a period of five years (2011 to 2015) are used in the following analysis with typical ranges between 10^{-2} and 300 μg L^{-1}. Note that since the chlorophyll concentrations typically follow the log-normal distribution [e.g., *Campbell and O'Reilly* [1988]; *Campbell* [1995]; *Robinson* [2004]], the difference between $\log_{10}$ and the natural log is equal to a scaling factor of $\ln 10$.

Because the GOCI-derived products have values on a non-orthogonal grid of unique longitudes and latitudes, they are optimally interpolated on a regular grid with a 0.005-degree resolution (approximately 0.5 km) to enable end users to easily analyze the data and quantify the uncertainties of the GOCI-derived products, using an exponential correlation function with an isotropic 1-km decorrelation length scale in the x and y directions to minimize the spatial smoothing (see Appendix A: for more details). In this paper, the gridded chlorophyll data are primarily analyzed, and the raw chlorophyll data are used to cross validate the gridded data. Although hourly GOCI-derived chlorophyll concentration data may resolve the diurnal variability, we focus on the seasonal variability and its potential drivers in this paper.

2.2.2 MODIS and VIIRS

The chlorophyll concentration maps obtained from the daily Level 3 MODIS and Visible Infrared Imaging Radiometer Suite (VIIRS) at a spatial resolution of approximately 3.7 km off the EJS over periods of five years (2011 to 2015) for MODIS and four years (2012 to 2015) for VIIRS are analyzed to cross validate the synoptic and seasonal variability of the regional chlorophyll concentrations [e.g., *Ocean Biology Processing Group* [2003]; *Wang et al.* [2013]; *Mikelsons et al.* [2014]] (Figure 3). The time series of the chlorophyll concentrations along the cross-shore line (Figures 3a to 3c) and their composite means derived using a 10-day bin (Figures 3d to and 3i) show nearly consistent temporal and spatial variability. Similarly, the daily Level 3 MODIS photosynthetically available radiation (PAR) data with the same spatial resolution and over the same time period are analyzed in the cross-shore direction.

2.3 Vertical stratification and nutrient profiles

The reconstructed vertical profiles of the temperature, salinity, and nutrients (phosphate, silicate, and nitrate) are used to examine the vertical stratification, thermocline, and nutrients in the cross-shore direction for a period of one year (2013) (Figures 4, 5, 6, and 7e to 7h). A regression analysis is applied to the data sampled at approximately every two months during the National Fisheries Research And Development Institute (NFRDI) hydrographic surveys of the past 20 years (1995 to 2014) using the basis functions of the temporal mean, the seasonal frequency and its five super-harmonic frequencies, and the linear trend [see *Yoo et al.* [2018] for more details and Appendix B: for uncertainty assessment of the derived climatology]. As the regressed time series are periodic over the years, the statistics of the mixed layer depth (MLD), temperature, density, and nutrient profiles for one year (2013) will be nearly identical to the statistics of those variables for multiple years (e.g., 2010 to 2014) when the contribution of the linear trend can be ignored. The linear trend has relatively small amplitudes compared to those of the seasonal and its super-harmonic variance. Thus, we present the variability of all available observations for a period of one year (2013). In this area, there is no influence from freshwater (e.g., riverine waters). Thus, the regional vertical stratification is represented using temperature profiles because density is more primarily governed by temperature than salinity

The seasonal stratifications at the open ocean stations (C7, C8, C9, and C10 stations; SUL in Figure 1d) on Line 104 are presented with the temperature profiles overlaid with isopycnals of 25.5 and 26.5 $\mathrm{kg\,m^{-3}}$ (Figure 4). In addition, phosphate, silicate, and nitrate have been sampled only within the upper 100-m and at the odd number stations (C5, C7, C9, and C11 stations). These data are regressed and reconstructed in the same way to represent the variability of the nutrient profiles in the coastal (C5 station; IMW) and open ocean areas (C7, C9, and C11 stations; SUL) (Figure 5). Note that the vertical stratification of the coastal areas (C0, C1, C4, and C6 stations; IMW in Figure 1b) has been reported in *Yoo et al.* [2018]. As the vertical stratification and nutrient profiles on Line 103 are similar to those on Line 104, the data on Line 103 are not shown in the paper.

A MLD is defined as the vertical length from the ocean surface where the nearly uniform characteristics of the water properties are still associated with air-sea interactions, including heating and cooling due to heat fluxes and responses to wind stress, and ocean processes such as turbulent mixing and dissipation [e.g., *Monterey and Levitus* [1997]; *Thomson and Fine* [2003]]. Thus, heat and momentum exchanges through the MLD have been an important aspect of elucidating ocean mixing and energy dissipation from the ocean at regional and global scales [e.g., *Monterey and Levitus* [1997]; *de Boyer Montégut et al.* [2004]; *Holte and Talley* [2009]]. Several studies have suggested approaches to quantify the MLD: (1) a vertical gradient of the given profiles of temperature [e.g., *Kara et al.* [2000]; *de Boyer Montégut et al.* [2004]; *Holte and Talley* [2009]] and density [e.g., *Brody and Lozier* [2014]; *Holte and Talley* [2009]] and (2) a threshold value of the temperature [e.g., *Dong et al.* [2008]; *Thomson and Fine* [2003]]. However, although an advanced approach has been proposed to identify the MLD via the temperature profiles with moderate vertical gradients [e.g., *Holte and Talley* [2009]], it remains difficult to clearly identify the MLD, particularly in the winter. Thus we chose the isopycnal depths of 25.5, 26.0, and 26.5 $\mathrm{kg\,m^{-3}}$ as the effective MLD and an indicator of the active mixing depth [*Yoo et al.* [2018]], which is consistent with the seasonal variability of the MLDs reported in previous studies off of the EJS [e.g., *Shim and Kim* [1981]; *Jang et al.* [1995]; *Chang et al.* [2011]].

2.4 Coastal surface wind stress

Nowcast coastal wind stress data from near the EJS at the spatial and temporal resolutions of 6 km and six hours, respectively have been obtained from the Local Data Assimilation and Prediction System (LDAPS; see the Acknowledgment), operated by the Korea Meteorological Agency (KMA).

Coastal wind-driven upwelling and down-welling are quantified with (1) the vertical velocity (w_d) as a direct wind response near the coast due to the Ekman transport by the along-shore wind stress (τ_a) and (2) the vertical velocity (w_i) as an indirect wind response beyond the near-coastal region due to the Ekman pumping by the wind stress curl ($\nabla \times \boldsymbol{\tau}$) [e.g., *Rykaczewski and Checkley* [2008]; *Risien and Chelton* [2008]]:

$$w_d = \frac{\tau_a}{\rho f_c R}, \tag{1}$$

$$w_i = \frac{\nabla \times \boldsymbol{\tau}}{\rho f_c}, \tag{2}$$

where ρ, f_c, R, and $\boldsymbol{\tau}$ denote the sea water density, local Coriolis frequency, local Rossby radius of deformation, and wind stress vector, respectively. The first column in Figure 2 shows examples of the wind stress field (arrows) overlaid on the vertical velocity (w_i; colors) field driven by the wind stress curl, which can highlight the enhanced vertical velocity near the coast in the summer (Figure 2f).

2.5 Mesoscale satellite-derived products

Altimeter (ALT)-derived daily SSHAs and geostrophic currents provided by AVISO [*Le Traon et al.* [1998]] at a resolution of approximately 0.25 degrees for a period of one year (2013) off of the EJS are analyzed (third column in Figure 2). The daily SST maps provided by the Operational Sea Surface Temperature and Sea Ice Analysis (OSTIA) at the UK Met Office (UKMO) at a resolution of 0.05 degrees over a period of one year (2013) in the same area are analyzed, as are their seasonal anomalies (fourth and fifth columns in Figure 2) [e.g., *Stark et al.* [2007]; *Yoo et al.* [2018]]. These two products are used to accommodate the broad context of the mesoscale circulation (e.g., eddies and fronts) in the study domain.

2.6 Coastal surface currents

Hourly HFR-derived submesoscale coastal surface currents are available in the coastal area (IMW) and contain low-frequency geostrophic currents, submesoscale eddies with the Rossby numbers ranging from -1 to 2.5 and their cross-shore propagations, and onshore-propagating clockwise near-inertial motions [*Yoo et al.* [2018]]. The relative vorticity (ζ; $\zeta = \partial v/\partial x - \partial u/\partial y$ denotes the vertical component of the relative vorticity) and stream function (ψ) of the submesoscale surface current maps are directly compared with the vorticity of AVISO geostrophic currents and the AVISO SSHAs to evaluate the consistency of submesoscale and mesoscale variability [e.g., *Kim et al.* [2008]; *Kim* [2010]].

3 Methods

We investigate variability of the regional chlorophyll blooms and their dynamical interpretations using concurrent observations of the wind stress, vertical stratification, nutrient profiles, SST and its seasonal anomalies, mesoscale SSHAs and geostrophic currents, and submesoscale coastal surface currents (section 4.1). Additionally, we examine the turbulent characteristics of the chlorophyll concentration maps via their wavenumber domain energy spectra (section 4.2). Prior to the presentation of the variability of the regional chlorophyll blooms and potential drivers, we include the formulations used to estimate the energy spectra and their spectral decay slopes (sections 3.1 and 3.2). Particularly, to elucidate the anisotropy and seasonality of the submesoscale turbulent flows, we examine the one-dimensional wavenumber-domain energy spectra of the chlorophyll concentrations sampled along individual grid lines and directions and their spectral decay slopes.

3.1 Estimates of energy spectra

The one-dimensional wavenumber-domain energy spectrum [$Q_x(k)$] of the chlorophyll concentrations [$d = d(x, y, t)$] in the zonal or cross-shore directions (x) is estimated using an ensemble average with respect to time (t) of the individual energy spectra [$\mathcal{Q}_x(k, t)$], which are (ensemble) averaged in the meridional or along-shore direction (y):

$$Q_x(k) = \langle \mathcal{Q}_x(k, t) \rangle_t, \tag{3}$$

$$\mathcal{Q}_x(k, t) = \langle \left| \int_{-\infty}^{\infty} d(x, y, t) e^{-ikx} \mathrm{d}x \right|^2 \rangle_y, \tag{4}$$

where $\langle \cdot \rangle_{\{\cdot\}}$ denote the ensemble average with respect to the subscript. The chlorophyll concentrations have their temporal averages removed, then are normalized by their standard deviations at each temporal realization to avoid an overly dominant contribution of high values to the ensemble average prior to the spectral estimate. Specifically, since each energy spectrum is normalized by 'a constant value' regardless of wavenumber, the normalized energy spectra and their ensemble average do not impact on the estimates of the spectral decay slopes. Similarly, the energy spectrum [$Q_y(k)$] of the chlorophyll concentrations in the meridional or along-shore direction is defined as follows:

$$Q_y(k) = \langle \mathcal{Q}_y(k, t) \rangle_t, \tag{5}$$

$$\mathcal{Q}_y(k, t) = \langle \left| \int_{-\infty}^{\infty} d(x, y, t) e^{-iky} \mathrm{d}y \right|^2 \rangle_x. \tag{6}$$

Individual energy spectra [$\mathcal{Q}_x(k, t)$ and $\mathcal{Q}_y(k, t)$] are estimated from chlorophyll concentration maps for a period of five years (2011 to 2015) sampled over three regions: (1) an area completely overlapped with HFR-derived surface currents [$Q_{\mathsf{C1}}(k)$, IMW], (2) an area 35 km from the coast [$Q_{\mathsf{C2}}(k)$, IMW], and (3) an open ocean area [$Q_{\mathsf{O}}(k)$, SUL]. Note that the GOCI-derived chlorophyll concentrations are analyzed in these three regions, and the MODIS-derived and VIIRS-derived chlorophyll concentrations are analyzed only in the open ocean area due to a lack of data realizations near the coast.

3.2 Estimates of spectral decay slopes

The spectral decay slopes of the individual energy spectra [$\mathcal{Q}_x(k,t)$ and $\mathcal{Q}_y(k,t)$] are estimated for three wavenumber ranges ($0.018 \leq k_0 \leq 0.095$ km^{-1}, $0.018 \leq k_0^* \leq 0.05$ km^{-1}, $0.1 \leq k_1 \leq 0.4$ km^{-1}, and $0.5 \leq k_2 \leq 1$ km^{-1}) using a least-squares fit. The estimated spectral decay slopes are compositely bin-averaged on the day of the year axis with a spacing of 10 days, and the temporal mean and standard errors of the estimated spectral decay slopes in each bin are presented with a square and vertical bar, respectively, for the cross-shore and along-shore directional energy spectra. The colored horizontal lines indicate the expected spectral decay slopes (k^{-1}, $k^{-5/3}$, and k^{-3}) of the individual wavenumber ranges, which will be discussed to delineate the appropriate theoretical frameworks (section 4.2). The number of chlorophyll concentration maps used in the spectral decay slope estimates are presented as a histogram, and the upper bound of each histogram can vary.

4 Results

4.1 Variability of chlorophyll blooms

4.1.1 Observations of regional chlorophyll blooms

The seasonal climatology of the 10-day bin-averaged GOCI-, MODIS-, and VIIRS-derived chlorophyll concentrations along the cross-shore line (Figure 1a) for a period of five years (2011 to 2015) as measured next to the EJS exhibits the common features of (1) two seasonal blooms in the spring (from early-April to early-May) and fall (from mid-October to mid-November) and an intermediate-size bloom in the summer (from June to July), (2) the time delay of the spring bloom moving from offshore to onshore (the bloom appears offshore on April and onshore on May), (3) the lack of time delay of the fall bloom in the cross-shore direction, and (4) the enhanced chlorophyll concentrations within 50 km off the coast during the fall bloom (Figures 3). Note that the chlorophyll concentrations in SUL have distinct blooms in the spring and fall, even though SUL is considered to be an offshore region in this paper.

4.1.2 Light, stratification, wind, and nutrients

In the spring, the regional bloom is initiated by an increase of the effective amount of sun light, which serves as a primary driver of the spring bloom as shown in the anomalies of the regional PAR time series from the temporal mean over the entire year (Figures 7a and 7i), presuming a sufficient level of nutrients and well-mixed conditions, which can be maintained in the winter of the preceding year [e.g., *Mann and Lazier* [2013]]. Although the PAR contains intermittent low values during the summer due to cloud shadows, the effective amount of light required for photosynthesis at the ocean surface is available from March to mid-November (Figure 7a). The PAR is enhanced nearshore rather than offshore during the winter and moderate variations are observed in the cross-shore direction over the rest of year. Note that the high biological productivity in the upper ocean during the spring blooms off of the EJS can be associated with the atmospheric input of Asian dust [e.g., *Yuan and Zhang* [2006]; *Jo et al.* [2007]].

Conversely, the well-mixed conditions due to frequent and enhanced storm events can explain the regional fall blooms when accompanied by sufficient light conditions and the relatively limited nutriments resulting from the spring bloom and subsiding levels of chlorophyll concentrations during the summer [e.g., *Kim et al.* [2007]; *Yoo and Park* [2009]]. In this region, the vertical stratification exhibits seasonal and its super-harmonic variability (SA_1, SA_2, and SA_3), which can amplify the blooms in spring and fall due to the local deepening of the MLD, which is slightly different from the bloom initiation due to the relaxation of turbulent mixing at the end of the winter [e.g., *Huisman et al.* [1999]; *Maúre et al.* [2017]] .

The coastal upwelling and down-welling favorable winds along the east coast of Korea are set up from May to June in the summer and from November to February in the winter, respectively; these winds are associated with a regional monsoon system [e.g., *Lee* [1983]; *Lee and Na* [1985]; *Byun* [1989]; *Lee and Chang* [2014]; *Shin et al.* [2017]] (Figures 7b and 7c). The vertical velocities driven by direct (w_d) and indirect (w_i) wind stress exhibit seasonality, such that the direct one is approximately three times stronger than the indirect one. In addition, the wind stress curl off the coast appears to be positive during the summer and negative in the winter [e.g., *Yoon et al.* [2005]; *Trusenkova et al.* [2008]] (Figures 2f, 7b, and 7c). The seasonal SST anomalies along the coastline show the poleward migration of the upwelled waters (Figures 2i, 2j, and 7d).

In the winter, the reduced chlorophyll concentrations were closely related to the light-limited conditions, even though the water column contains sufficient nutrients and is well-mixed (Figures 7a and 7i) [e.g., *Michaelsen et al.* [1988]; *Chiswell et al.* [2013]; *Mann and Lazier* [2013]; *Smith et al.* [2016]].

The time series of the vertical profiles of the nutrients (phosphate, silicate, and nitrate) and their depth-integrated time series show the seasonal and its super-harmonic variability, which is consistent with the variability of temperature profiles in terms of (1) the timings to reach their enhanced magnitudes, particularly in the summer and fall, in the cross-shore direction and (2) the spatially decreasing concentrations from onshore to offshore (Figures 5 and 6). However, the seasonal variability of the nutrients show slight time lags and decoupled features in their maximum values. For instance, the phosphate concentrations were relatively low in September of 2013 when compared with those of the enhanced silicate and nitrate concentrations at the same time. Conversely, all three nutrients at the C5 station are nearly coherent (Figures 5a, 5e, and 5i), and phosphate and silicate are consistent with the upwelling events in the summer (Figures 5a to 5d and 5e to 5h). In the winter, although silicate and nitrate are relatively enriched (Figures 5e to 5h, 5i to 5l, and 6b and 6c), there is no bloom, which may result from the limited light conditions (Figure 7a). The vertical extent of the nutrients, excepting silicate and nitrate in the winter, typically reaches as far upward as 20 m from the surface, which is consistent with the variability of the MLD (Figures 4 and 5). The nutrients in the upper layer (within 100 m depth) become enriched in the summer due to the upwelling events and become enriched in the fall due to the well-mixed conditions derived from storm events (Figures 5, 6b, and 7f to 7h).

4.1.3 Horizontal advection and vorticity at the mesoscale and submesoscale

As potential drivers of phytoplankton blooms, regional horizontal advection and vorticity at the mesoscale and submesoscale are examined using (1) ALT-derived SSHAs, normalized vorticity, and geostrophic currents (Figure 8) as well as (2) HFR-derived surface stream functions, normalized vorticity, and surface currents (Figure 9), respectively [e.g., *McGillicuddy et al.* [1998]; *Mahadevan and Tandon* [2006]; *McGillicuddy et al.* [2007]; *Taylor and Ferrari* [2011b]; *Omand et al.* [2015]; *McWilliams* [2016]]. The normalized vorticity or Rossby numbers ($R_o = \zeta/|f_c|$) is referred to as the vorticity normalized by the Coriolis frequency (f_c). Note that the positive SSHAs ($\eta > 0$; red), negative vorticity ($\xi = \zeta/|f_c| < 0$; red), and negative stream function ($\psi < 0$; red) indicate clockwise rotational flows.

The ALT-derived SSHAs can be equivalent to the HFR-derived surface stream functions when the divergence of the surface current fields becomes negligible. The signs of the SSHAs (or stream function), the normalized vorticity (ζ), and the current components at the mesoscale and submesoscale are nearly consistent in the cross-shore direction; only slight differences in their magnitudes are observed (Figure 10). The scaled stream functions (ψ_S / ψ_S^*) of the observed surface currents are correlated with the SSHAs near the coast (Figure 10a), which can be used as a tool to estimate the low-frequency SSHA maps from the HFR-derived surface current maps [e.g., *Yoo et al.* [2018]]. Because the mesoscale vorticity is estimated from geostrophic currents at a resolution of 25 km, the mismatch of the vorticity in two independent observations can be expected as a result of spatial scale differences and the amplification of potential contaminated altimeter signals near the coast (Figure 10b). The velocity components are nearly correlated in their low-frequency variance (Figures 10c and 10d). The differences between the two independent observations can be considered to be contributions of the ageostrophic components of the HFR-derived surface current observations, including coastally trapped signals, ageostrophic circulations (e.g., wind-driven surface currents, intermittent eddies and fronts), and near-inertial currents [e.g., *Kim* [2010]; *Kim et al.* [2013]; *Yoo et al.* [2018]; *Kim and Kosro* [2013]] or the observational noise and errors.

The mesoscale circulation off of the EJS is characterized by the northeastward EKWC and southward NKCC [e.g., *Kim and Kim* [1983]; *Yun et al.* [2004]; *Lie et al.* [2001]]. Moderate seasonal or seasonal super-harmonic variability in the open ocean area is represented by the clockwise Ulleung Warm Eddy and East Sea Intermediate Water [e.g., *Chang et al.* [2004]; *Cho et al.* [1990]; *Kim and Kim* [1999]; *Chang et al.* [2002]; *Hu et al.* [1991]; *Hur et al.* [1999]]. For instance, a 100-km-diameter warm (clockwise) eddy stays near the Ulleungdo from January to April, and appears as meridional shear currents and clockwise vorticity. This feature then migrates southeastward and disappears (Figures 8b and 8d). Then, two 50-km-diameter cold (counter-clockwise) eddies appear in May. A branch of the northward EKWC appears between 50 to 120 km from the coast, starting in May and lasting until November (Figures 2h and 8d). A counter-clockwise flow appears within 50 km from the coast during the same time period (Figures 2h and 8d) and is related to the generation of the SPF in May; this feature lasts for most of the summer and fall. In the transition between the weakening of the warm eddy and the generation of the SPF, the warm eddy approaches the shore, which is related to the onshore movement of the eastward currents and can lead the time-delayed spring chlorophyll blooms of the onshore and offshore areas (Figure 8c). A 100-km-diameter cold eddy approaches the onshore region from November to December (Figures 8b, 8c, and 8d).

Based on submesoscale observations, the vorticity pairs with opposite signs located at 25 km from the coast in April, October, and November are related to the meridional shear currents centered at that location (Figures 9b and 9d). The vorticity propagates offshore with time during the onset and demise of the meridional shear currents (black arrows in Figures 9a to 9d); at the same time, there are nearly stationary shear currents and zonal shear currents (Figures 9a, 9c, and 9e). In the coastal regions, current reversals are observed between June and July (Figure 9d) and could be associated with the regional variability of the boundary currents, along-shore buoyancy gradients, and sub-inertial temperature variability [e.g., *Yoo et al.* [2018]].

4.1.4 Potential drivers of regional chlorophyll blooms

In this region, the time-delayed spring chlorophyll blooms in the cross-shore direction are aligned with (1) the onshore propagating eastward geostrophic currents (and eastward surface currents) in April of 2013 (Figures 8b and 8c), (2) the onset of the deepening of the MLD (e.g., 26.0 and 26.5 $\mathrm{kg\,m^{-3}}$) (Figure 4), and (3) the conditions required for sufficient fluxes of nutrients from depths exceeding 100 m (Figure 5). The spring and fall chlorophyll blooms are more significant near the coast (within 50 km from the coast) than offshore because of (1) the increased energetic submesoscale shear and vertical circulations in the coastal region [e.g., *Taylor and Ferrari* [2011a]; *Omand et al.* [2015]] and (2) the involvement of their onshore and offshore propagations in the cross-shore direction, which can lead to enhanced vertical mixing due to frontal-scale secondary circulations and the relevant physio-biological interactions (Figures 9a and 9b) [e.g., *Demers et al.* [1986]; *Kim* [2010]]. The intermediate-size bloom in the summer is closely related to the direct and indirect wind-forced upwelling and relevant biological responses (Figures 7c and 7d) [e.g., *MacIntyre and Jellison* [2001]]. All these blooms can be initiated when a minimum level of nutrients and light is satisfied [e.g., *Mann and Lazier* [2013]].

4.2 Turbulent characteristics of chlorophyll concentrations

The spectral decay slopes of the wavenumber domain energy spectra become steeper and flatter depending on the characteristics of the turbulent flows and relevant theories (Table 1). For instance, the spectral decay slopes of the energy spectra of the currents [$E(k)$] and concentrations [$Q(k)$] are described with k^{-n} and $k^{(n-5)/2}$, respectively [e.g., *Vallis* [2006]; *Callies and Ferrari* [2013]]. Two length scales can be defined wherein the spectral decay slopes are changed corresponding to the transition of turbulent characteristics: an injection scale (λ_I) to delineate the inverse and forward cascades and a dissipation scale (λ_D) to divide the forward cascades and surface dissipation [e.g., *Vallis* [2006]; *Ferrari and Wunsch* [2009]; *Soh and Kim* [2018]].

The wavenumber domain energy spectra [$Q_{\mathsf{C1}}(k)$ and $Q_{\mathsf{C2}}(k)$] of the chlorophyll concentrations sampled in the coastal region (IMW) show consistent spectral decay slopes of k^{-1} ($\lambda > \lambda_D$; $\lambda_D = 3$ km) and $k^{\leq -3}$ ($\lambda \leq \lambda_D$) in both cross-shore and along-shore directions (Figure 11a). In the same region, the KE spectra of the (surface) currents have spectral decay slopes between k^{-2} and k^{-3} at a scale of 2 km [e.g., *Yoo et al.* [2018]]. These two submesoscale observations of the chlorophyll concentrations and surface currents can be explained by either QG theory or turbulent flows under geostrophic bathymetric effects, which have spectral decay slopes of k^{-3} and $k^{-2.5}$ at a scale of $O(1)$ km, respectively [e.g., *Tulloch and Smith* [2006, 2009]; *Nikurashin et al.* [2013]; *Vallis* [2006] and Table 1]. The energy spectra of the chlorophyll concentrations in the cross-shore and along-shore directions are consistent, but not identical (Figure 11a). The spatial anisotropy in this region has been reported in the surface current observations as a result of the circulation bounded by the coastal boundaries [e.g., *Yoo et al.* [2018]]. Although the observations of the chlorophyll concentrations are limited within the study domain, particularly in the summer (June and July) (Figure 11g), the chlorophyll data sampled from a slightly offshore domain show consistent spectral decay slopes and anisotropy with greater statistical significance, as well as having a greater number of realizations (Figures 11b and 11h). The time series of the spectral decay slopes in the forward cascade region ($\lambda > \lambda_D$) exhibits seasonality and fluctuations at seasonal super-harmonic frequencies, shown as k^{-2} for the summer and k^{-1} for the winter (Figures 11c, 11d, 11e, and 11f). These spectral decay slopes may be explained with the regional baroclinic instabilities within the moderate seasonal MLDs associated with the submesoscale eddies and circulations influenced by coastal boundaries [e.g., *Yoo et al.* [2018]]. Conversely, the spectral decay slopes below the dissipation scale ($\lambda \leq \lambda_D$) appear to be nearly out of phase those in the forward cascade region and have weak seasonality (Figures 11c, 11d, 11e, and 11f).

The GOCI-derived chlorophyll concentrations sampled in the open ocean (SUL) exhibit spectral decay slopes of $k^{-5/3}$ ($\lambda > \lambda_I$, $\lambda_I = 10$ km), k^{-1} ($\lambda_D < \lambda \leq \lambda_I$), and $k^{\leq -3}$ ($\lambda \leq \lambda_D$) based on their wavenumber domain energy spectra [$Q_{\mathrm{O}}(k)$] in both the cross-shore and along-shore directions (Figure 12a). These spectral decay slopes can be interpreted as (1) the forward cascades of enstrophy (the integral of the square of the vorticity) and inverse cascades of energy appear at the injection scale [$\lambda_I = O(10)$ km], where the baroclinic instability in the mixed layer (see above) plays a more dominant role as the driver of the submesoscale processes rather than the mesoscale eddy-derived surface frontogenesis does at a scale of $O(100)$ km [e.g., *Ferrari and Wunsch* [2009]; *Tulloch et al.* [2011]] and (2) the surface dissipation scale appears near $O(1)$ km. Note that the KE spectra of the HFR-derived surface currents do not clearly show the dissipation scale due to limited spatial scale of the observations ($\lambda \geq 2$ km) [*Yoo et al.* [2018]]. Similarly, the MODIS- and VIIRS-derived chlorophyll concentrations sampled in the same region have nearly consistent variance of their energy spectra and spectral decay slopes at spatial scales greater than 30 km in the forward cascade region (Figures 12a and 12b). Note that the spectral decay slopes in both directions are nearly identical and differ at length scales of less than 5 km (Figure 12a), which shows the length scale that characterizes the anisotropy.

Similarly, based on the energy spectra of the open ocean chlorophyll concentrations, the spectral decay slopes in the forward cascade ($\lambda > \lambda_I$; k_0 and k_0^*) and inverse cascade ($\lambda_D \leq \lambda < \lambda_I$; k_1) show seasonality (Figures 12c to 12f). The spectral decay slopes below the dissipation scale ($\lambda \leq \lambda_D$; k_2) are slightly out of phase with those within the two wavenumber ranges (k_0, k_0^*, and k_1) (Figures 12c and 12e). The amount of data used in the estimates of the energy spectra is not uniformly distributed, which may lead to temporal biases toward January, February, June, July, November, and December (Figures 12g to 12i). Excluding the estimates in these time periods, the spectral decay slopes have fluctuations at the seasonal frequency and its super-harmonic frequencies and become steeper in the summer and flatter inthe winter (Figures 12c to 12f).

In three-dimensional turbulence, the dissipation scale appears at $O(1)$ cm, which can be associated with molecular dissipation. In contrast, in two-dimensional turbulent flows, the dissipation scale is related to the scales at which the gravity waves start to break; three-dimensional effects become important at scales of $O(1-100)$ m [e.g., *Nikurashin et al.* [2013]]. Thus, the surface dissipation scale appears near $O(1)$ km, which can be an upper bound of the observations analyzed in this paper [Fig. 6 in *Ferrari and Wunsch* [2009]].

The spectral decay slopes of the currents become steeper in the summer than those in the winter because the available potential energy is less in the summer than in the winter due to the shallower MLD in the summer [e.g., *Callies et al.* [2015]; *McWilliams* [2016]]. Based on the relationship between the spectral decay slopes of the currents (n_E) and concentrations (n_Q) [e.g., *Vallis* [2006]; see Table 1],

$$n_Q = -0.5n_E - 2.5, \tag{7}$$

the spectral decay slopes of the concentrations (or passive tracers) are expected to be flatter in the summer than those in the winter. This proves that the spectral decay slopes in the dissipation wavenumber range (k_2) are out of phase with those in the other wavenumber ranges (k_0, k_0^*, and k_1; Figures 12c and 12e).

The energy spectra of the GOCI-derived chlorophyll concentrations and HFR-derived surface currents [excerpt from *Yoo et al.* [2018]] are scaled by individual constant values to present them alongside the theoretical spectral decay slopes of the currents and concentrations (Figure 13a). A schematic presentation of both energy spectra explains the turbulent characteristics of the two submesoscale observations in the two-dimensional geophysical turbulent flows (Figure 13b) [see Fig. 8.13b in *Vallis* [2006]]. The agreement between the observational and theoretical spectral decay slopes can be interpreted as complementary resources to examine the submesoscale process studies.

5 Discussion

5.1 Cautionary remarks on the use of chlorophyll concentration maps for studies of geophysical turbulence

Spectral decay slopes are estimated from the hourly sampled GOCI-derived chlorophyll concentration maps, and their individual (ensemble) estimates are averaged over 10 days to examine their seasonality related to the mixed layer variability. The remotely sensed chlorophyll concentrations may be considered non-conserved quantities because (1) they report the depth-integrated phytoplankton concentrations from the surface to the optical penetration depth, and (2) the surface concentrations may have limitations in capturing the physiological ecology of the phytoplankton within the mixed layer (e.g., growth, death, and export of phytoplankton).

The vertically integrated primary production is generally proportional to remineralization, vertical mixing, and subsurface nutrient concentrations and inversely proportional to the rate of export [e.g., *Hodges and Rudnick* [2004]; *Beckmann and Hense* [2007]; *Ryabov and Blasius* [2008]]. For instance, the depth-integrated phytoplankton concentrations change with the vertical migration of the mixed layer [e.g., Figure 8 in *Beckmann and Hense* [2007]]: the detritus concentrations increase, and the subsurface maximum layer of the phytoplankton biomass profile breaks with the deepening of the mixed layer, which leads to the increase in depth-integrated phytoplankton concentrations. Thus, the growth and death of phytoplankton will affect the horizontal distribution of remotely sensed chlorophyll concentrations. However, the energy spectra of the chlorophyll concentration maps can be averaged with a time window longer than the time scale of the phytoplankton blooms, which can minimize the effect of the physiological ecology of the phytoplankton within the mixed layer in studies of geophysical turbulent flows.

5.2 Potential influences of the internal motions on vertical mixing

Shoreward-propagating internal waves in the clockwise near-inertial frequency band and at a semi-diurnal tidal frequency have been reported in this region [e.g., *Kim et al.* [2001, 2005]; *Yoo et al.* [2018]]. Since the biological productively associated with chlorophyll blooms is closely related to the nutrient fluxes from the below and enhanced vertical mixing [e.g., *Herman and Denman* [1979]; *Demers et al.* [1986]; *Lucas et al.* [2011]; *Omand et al.* [2015]; *Mann and Lazier* [2013]], the vertical motions of the internal tides can generate more effective vertical mixing and dissipation than near-inertial internal waves.

The flattening and steepening of the spectral decay slopes in this work have similar patterns to those of the pycnocline (or oxycline) depths observed in the eastern boundary current system, such that $k^{-5/3}$ ($\lambda > \lambda_I$), k^{-1} ($\lambda_D \leq \lambda < \lambda_I$), and k^{-2} ($\lambda \leq \lambda_D$), where $\lambda_I = 2$ km and $\lambda_D = 0.5$ km [e.g., *Grados et al.* [2016]], Although the corresponding injection and dissipations scales are slightly different, the observational analyses in this paper may stimulate additional investigations of the submesoscale vertical structure associated with internal waves using subsurface observations (e.g., ADCP or CTD profiles) [e.g., *Kim* [2010]; *Pinkel* [2014]] and numerical model runs driven by individual driving forcings [e.g., *Kim et al.* [2015]]. Moreover, these resources allow us to examine the submesoscale energy spectra and KE fluxes as well as their potential associations with internal waves [e.g., *Wunsch* [1997]; *Zang and Wunsch* [2001]; *Wortham et al.* [2014]].

6 Conclusions

The regional variability and turbulent characteristics of submesoscale surface chlorophyll concentrations are examined using hourly maps of geostationary ocean color imagery-derived chlorophyll concentration maps at a 0.5-km resolution for a period of five years (2011 to 2015) off of the EJS with concurrent mesoscale and submesoscale observations. Two seasonal blooms occur in the spring and fall within 250 km off the coast that are associated with constructive combinations of light exposure, nutrients, and vertical stratification. Particularly, the spring bloom and fall bloom are primarily governed by the effective amount of sun light and the mixing condition in the water column, respectively. Additionally, an intermediate-size bloom occurs in the summer and is closely related to regional direct and indirect wind-driven upwelling events. The spring and fall blooms are more significant closer to the coast (within 40 km off the coast) than offshore because of the more energetic submesoscale horizontal shear and vortical phenomena onshore as well as their propagation in the cross-shore direction, which can lead to enhanced vertical mixing due to the frontal-scale secondary circulations and physio-biological interactions. In addition, the regional spring bloom starts offshore and migrate onshore with a one month time delay, which may result from the onshore-propagating geostrophic currents, the deepening of the mixed layer, and the favorable nutrient fluxes from the subsurface. The wavenumber-domain energy spectra of the chlorophyll concentrations exhibit anisotropy, which may be closely related to bathymetric effects and regional circulations. The spectral decay slopes of the chlorophyll concentrations change from $k^{-5/3}$ to k^{-1} at the $O(10)$ km scales of the injection scale and from k^{-1} to $k^{\leq -3}$ at the $O(1)$ km dissipation scales as well as having weak seasonality. These results are consistent with two-dimensional QG turbulence theory and can be interpreted as the baroclinic instability energized by the moderate seasonal mixed layer under mesoscale regional circulations.

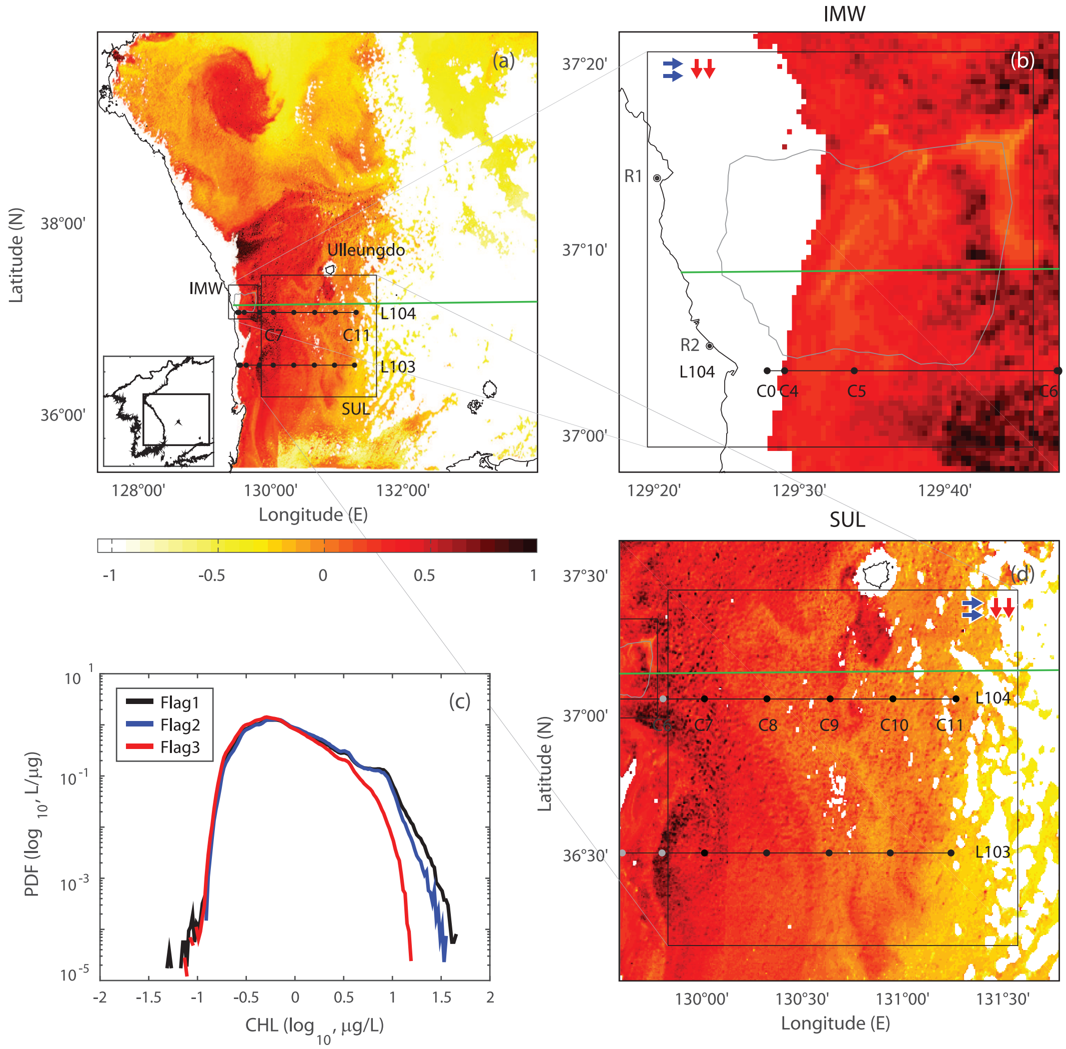

Figure 1. (a) An example of the GOCI-derived chlorophyll concentrations ($\log_{10}$, $\mu\mathrm{g\,L}^{-1}$) off the East/Japan Sea (EJS), sampled on October 12, 2013. A coastal region (Imwon; IMW) and an open ocean area (South of Ulleungdo; SUL) are marked with black boxes. Stations (C0 to C11) on two hydrographic survey lines (L103 and L104) to sample temperature, density, and nutrients are denoted. A cross-shore green line is chosen to examine seasonal variability of chlorophyll concentrations, relevant drivers (see Figures 3, 7, 8 and 9). (b) and (d): Close-up of two sub-domains [(b) IMW and (d) SUL]. The sampling directions of the one-dimensional wavenumber-domain kinetic energy spectra of chlorophyll concentrations are denoted with blue (cross-shore or zonal direction) and red (along-shore or meridional direction) arrows (see Figures 11, 12, and 13). The effective spatial coverage of HFR-derived surface currents is shown with a gray contour in Figures 1a and 1b. (c) Probability density functions (PDFs) of hourly chlorophyll concentrations ($\log_{10}$, $\mu\mathrm{g\,L}^{-1}$) in Figure 1b for a period of five years (2011 to 2015) in terms of the internal QAQC parameters (Flag1, Flag2, and Flag3; see Table 2 for more details). Figures 1a, 1b, and 1d share a colorbar on the bottom of Figure 1a.

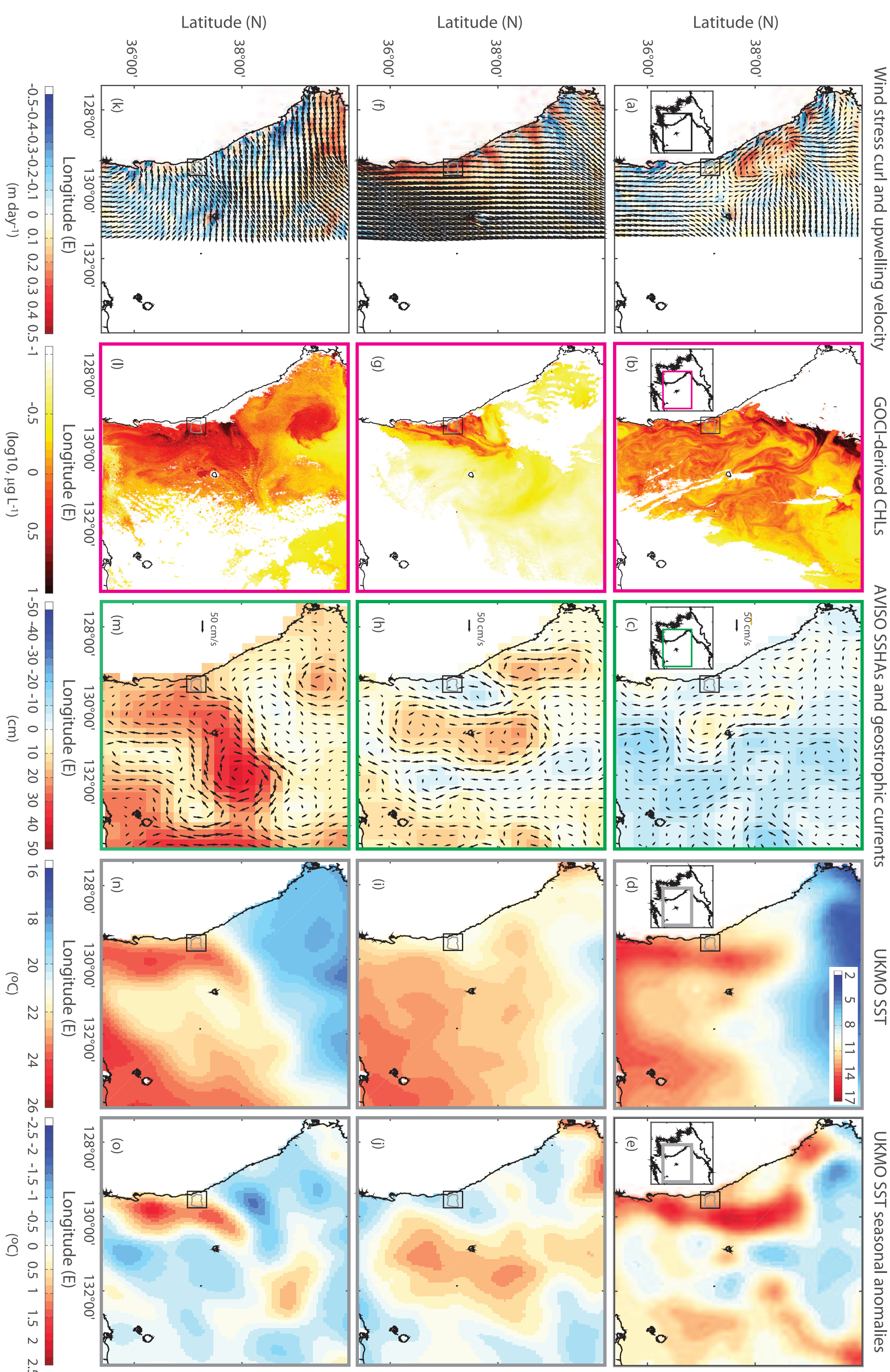
Wind stress curl and upwelling velocity
GOCI-derived CHLs
AVISO SSHAs and geostrophic currents
UKMO SST
UKMO SST seasonal anomalies
(a) (b) (c) (d) (e)
(f) (g) (h) (i) (j)
(k) (l) (m) (n) (o)
Latitude (N)
38°00'
36°00'
Longitude (E)
128°00'
130°00'
132°00'
50 cm/s
2 5 8 11 14 17
-0.5 -0.4 -0.3 -0.2 -0.1 0 0.1 0.2 0.3 0.4 0.5
(m day⁻¹)
-1 -0.5 0 0.5 1
(log10, μg L⁻¹)
-50 -40 -30 -20 -10 0 10 20 30 40 50
(cm)
16 18 20 22 24 26
(°C)
-2.5 -2 -1.5 -1 -0.5 0 0.5 1 1.5 2 2.5
(°C)

Figure 2. Examples of the seasonal chlorophyll concentrations variability and concurrent observations. Maps of [(a), (f), and (k)] KMA LDAPS wind vector and vertical velocity (w_i) associated with wind stress curl on a resolution of 1.5 km (Subsampled wind vectors with a spatial resolution of 4.5 km are only presented to avoid overlapping of arrows), [(b), (g), and (l)] GOCI-derived chlorophyll concentrations on a 0.5-km resolution grid ($\log_{10}$, μg L^{-1}), [(c), (h), and (m)] AVISO sea surface height anomalies and geostrophic currents on a quarter degree grid, and [(d), (i), and (n)] sea surface temperature (SST; OSTIA UKMO) on a 0.05 degree grid, and [(e), (j), and (o)] seasonal anomalies of the SST off East Coast of Korea on [(a) to (e)] April 3, [(f) to (j)] July 3, and [(k) to (o)] October 12, 2013. Note that figures in each column share the colorbar on the bottom except for Figure 2d.

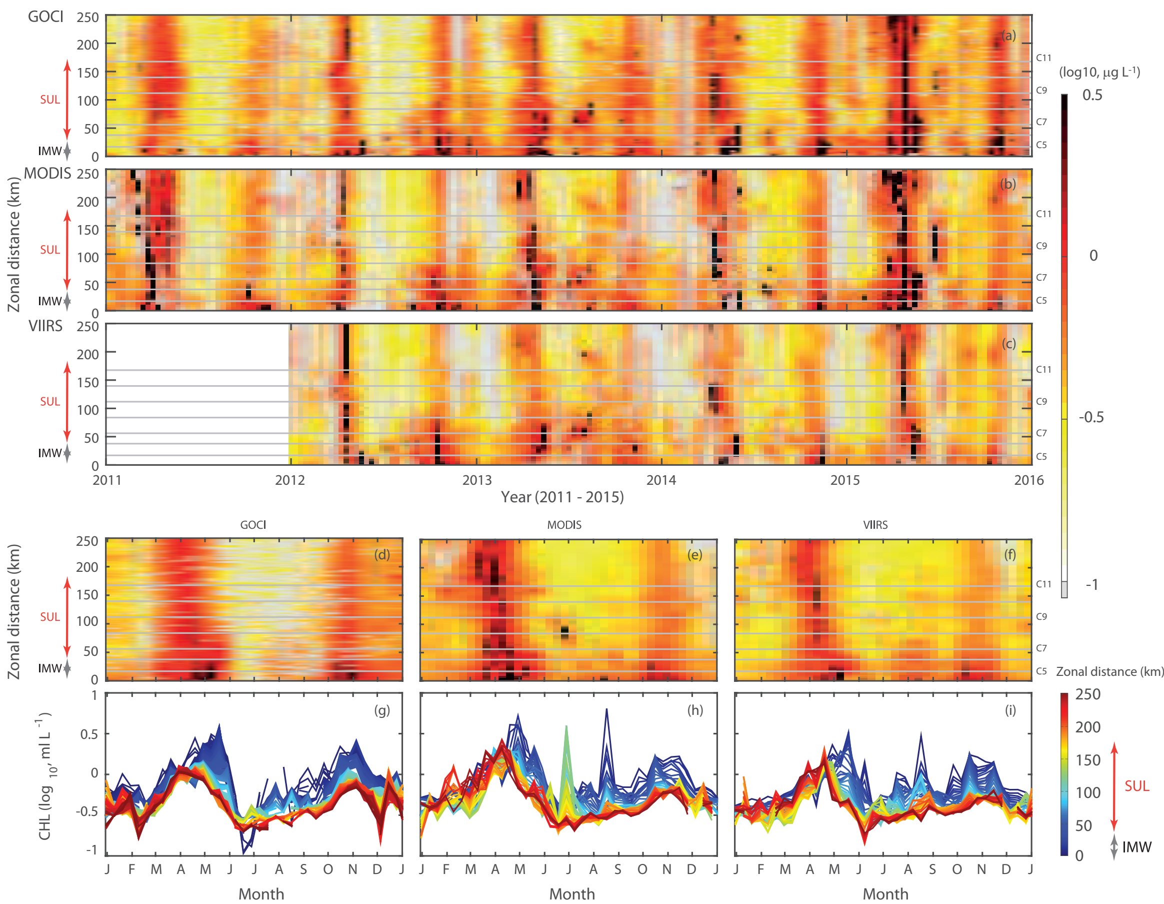

Figure 3. (a) to (c): 10-daily bin-averaged chlorophyll concentrations ($\log_{10}$, μg L^{-1}) obtained from hourly GOCI, daily MODIS, and daily VIIRS, sampled along the cross-shore line in Figure 1a, are presented as a function of time (2011 to 2015) and zonal distance (km). (d), (e), and (f): 10-daily bin-averaged two-dimensional climatology of the chlorophyll concentrations, presented as a function of months of the year and zonal distance (km). (g), (h), and (i): 10-daily bin-averaged one-dimensional climatology of the chlorophyll concentrations, color-coded by blue for nearshore and red for offshore. (a), (d), and (g): GOCI-derived chlorophyll concentrations. (b), (e), and (h): MODIS-derived chlorophyll concentrations. (c), (f), and (i): VIIRS-derived chlorophyll concentrations. Gray and white patches indicate observations with missing data and no observations, respectively. Cross-shore locations of CTD stations are marked with horizontal gray lines, and odd number stations are only denoted.

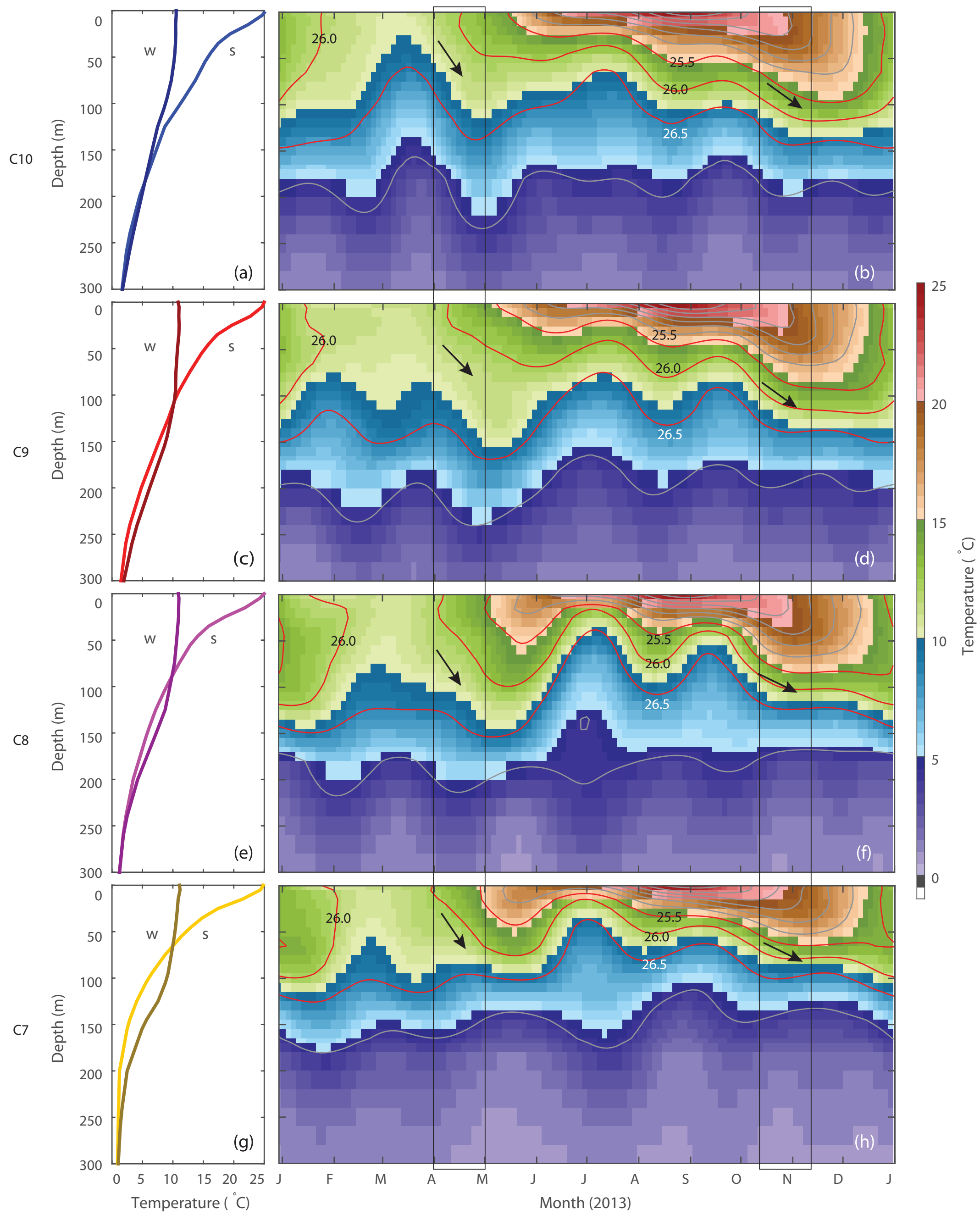
C10
C9
C8
C7
Depth (m)
0
50
100
150
200
250
300
w
s
(a)
(b)
(c)
(d)
(e)
(f)
(g)
(h)
26.0
25.5
26.5
0 5 10 15 20 25
Temperature (˚C)
J F M A M J J A S O N D J
Month (2013)
25
20
15
10
5
0
Temperature (˚C)

Figure 4. Seasonal temperature profiles and time series of the reconstructed temperature profiles (°C) on a three-daily time axis at the C7, C8, C9, and C10 stations along the hydrographic survey Line 104 (Figure 1). (a), (c), (e), and (g): Seasonal temperature profiles. Paler and darker colors indicate summer (s) and winter (w) profiles, respectively. (b), (d), (f), and (h): Time series of the temperature profiles on a three-daily time axis for a period of one year (2013), reconstructed from a regression analysis using basis functions of a temporal mean, seasonal frequency and its five harmonic frequencies on the approximately bi-monthly sampled temperature records for recent 20 years (1995 to 2014) (see section 2.3 for more details). The isopycnals are marked with a density interval of 0.5 $\mathrm{kg\,m^{-3}}$, and the constant density anomalies of 25.5, 26.0, and 26.5 $\mathrm{kg\,m^{-3}}$ are highlighted with red. Two rectangular black boxes denote two time windows of seasonal chlorophyll blooms, and black arrows indicate slopes of isopycnals.

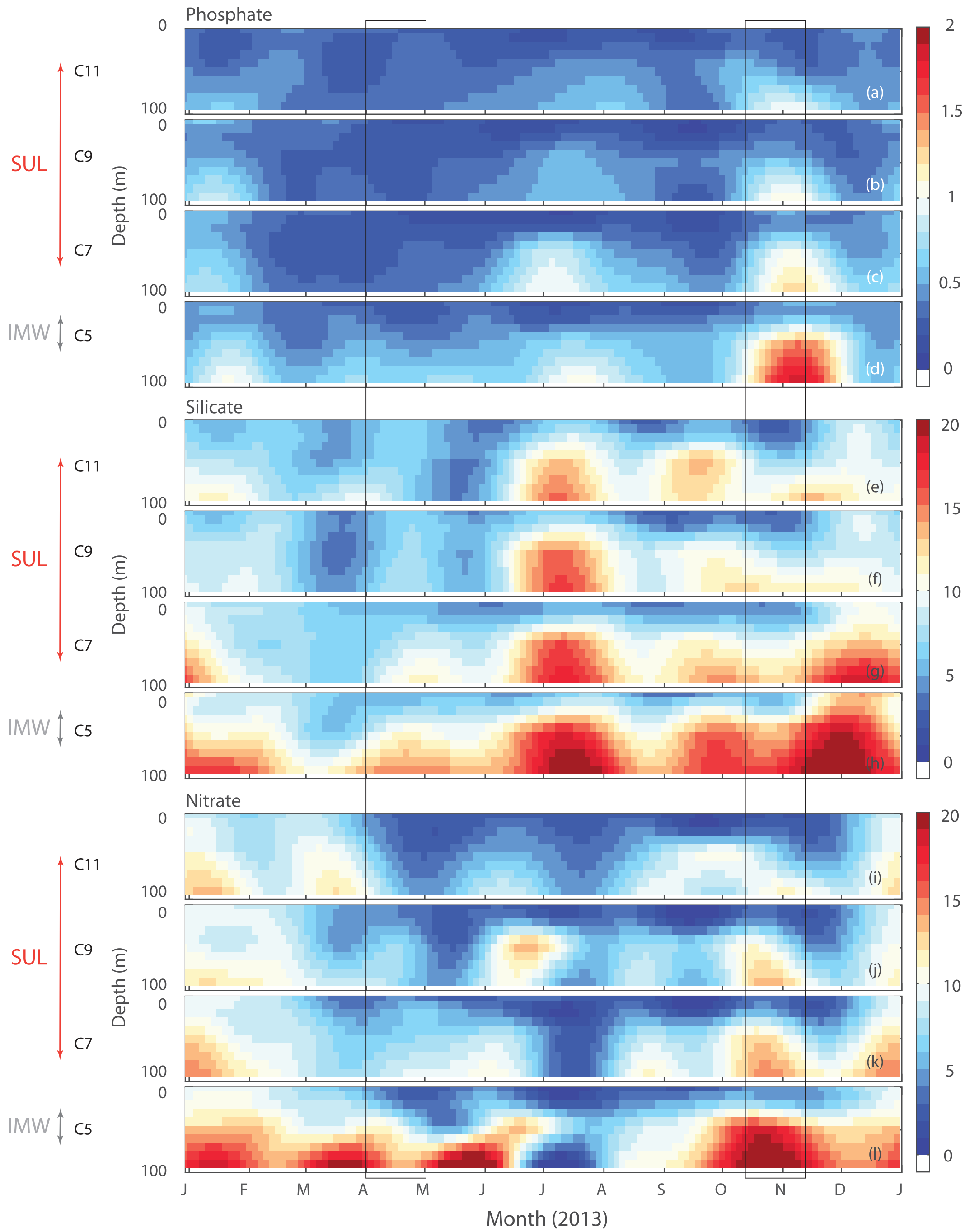

Phosphate
Silicate
Nitrate
SUL
IMW
C11
C9
C7
C5
Depth (m)
0
100
(a)
(b)
(c)
(d)
(e)
(f)
(g)
(h)
(i)
(j)
(k)
(l)
2
1.5
1
0.5
0
20
15
10
5
0
J F M A M J J A S O N D J
Month (2013)

Figure 5. Time series of the reconstructed nutrient profiles (phosphate, silicate, and nitrate) on a three-daily time axis in the upper 100 m sampled at the C5, C7, C9, and C11 stations along the hydrographic survey Line 104 (Figure 1). (a) to (d): Phosphate (μg L^{-1}). (e) to (h): Silicate (μg L^{-1}). (i) to (l): Nitrate (μg L^{-1}). (a), (e), and (i): C5 station (IMW). (b), (f), and (j): C7 station (SUL). (c), (g), and (k): C9 station (SUL). (d), (h), and (l): C11 station (SUL). Nutrient time series on a three-daily time axis for a period of one year (2013), reconstructed from a regression analysis using basis functions of a temporal mean, seasonal frequency, and five harmonic frequencies on the approximately bi-monthly sampled temperature records for recent 20 years (1995 to 2014) (see section 2.3 for more details). Two rectangular black boxes denote two time windows of seasonal chlorophyll blooms.

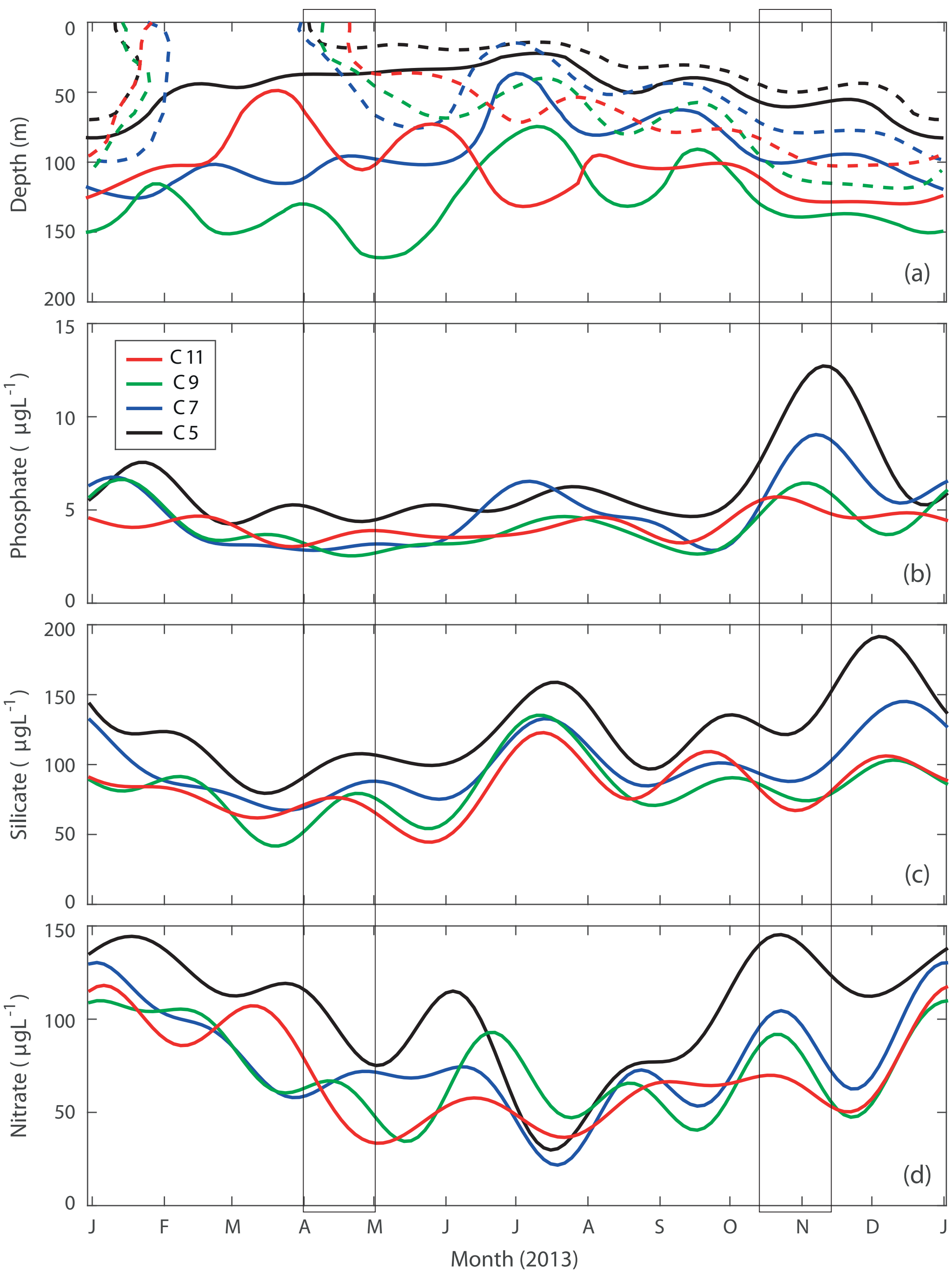

Figure 6. Time series of the mixed layer depth (MLD) [$\rho = 26.0\ \mathrm{kg\,m^{-3}}$ (dashed) and $\rho = 26.5\ \mathrm{kg\,m^{-3}}$ (solid)], the depth-integrated and reconstructed nutrient profiles (phosphate, silicate, and nitrate) on a three-daily time axis within the upper 100 m (Figure 5) sampled at the C5, C7, C9, and C11 stations along the hydrographic survey Line 104 (Figure 1). (a) MLD (m), (b) Phosphate ($\mu\mathrm{g\,L^{-1}}$), (c) Silicate ($\mu\mathrm{g\,L^{-1}}$), and (d) Nitrate ($\mu\mathrm{g\,L^{-1}}$). Two rectangular black boxes denote two time windows of seasonal chlorophyll blooms.

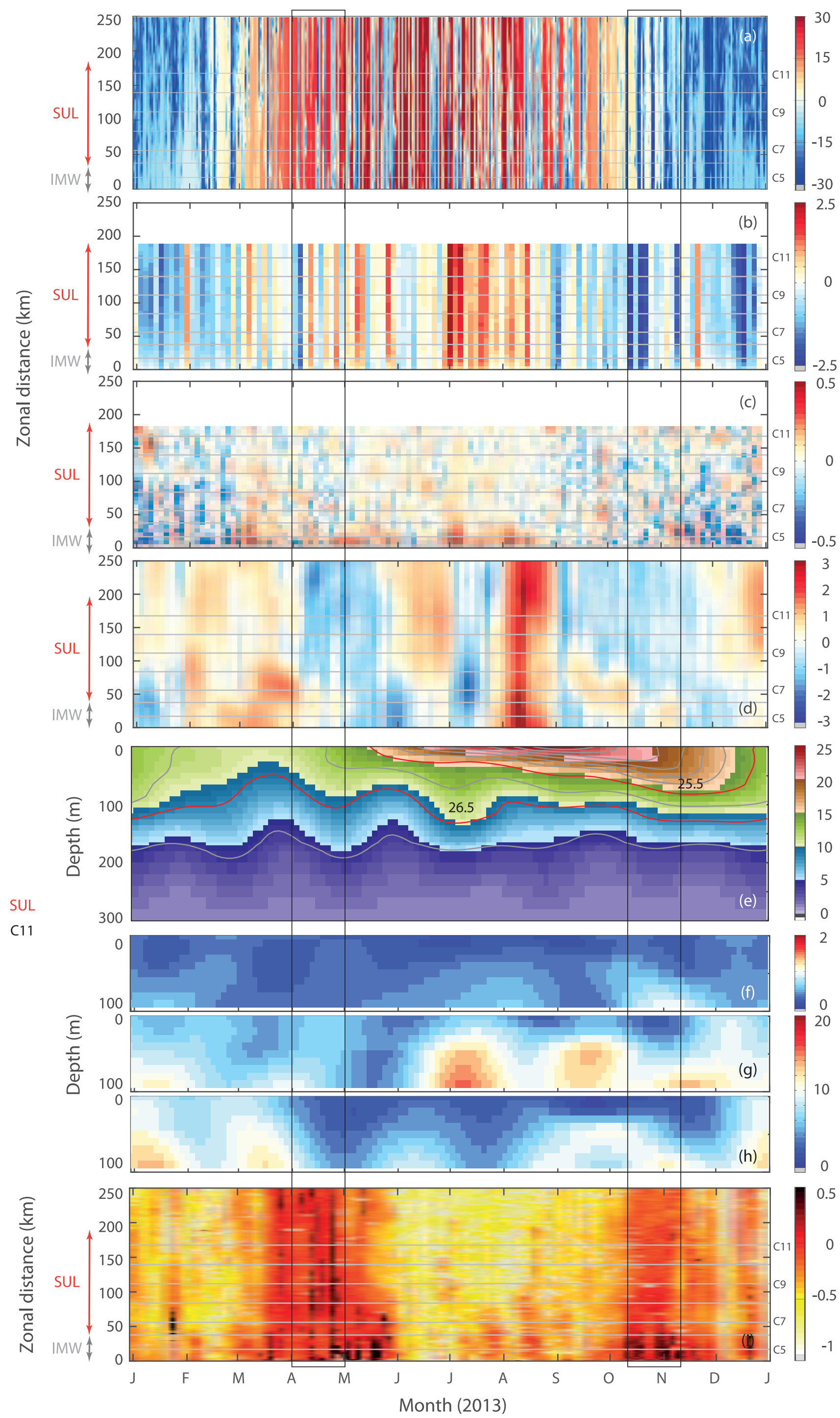

(a)
(b)
(c)
(d)
(e)
(f)
(g)
(h)
(i)
SUL
IMW
C11
C9
C7
C5
Zonal distance (km)
Depth (m)
26.5
25.5
J F M A M J J A S O N D J
Month (2013)

Figure 7. Time series of (a) anomalies of the MODIS photosynthetically available radiation (PAR; einstein $\mathrm{m^{-2}\,day^{-1}}$) from the temporal mean for the entire year, (b) and (c) direct and indirect wind-forced vertical velocity (w_d and w_i in equations 1 and 2) [KMA LDAPS; $\mathrm{m\,day^{-1}}$], (d) seasonal anomalies of the sea surface temperature [SSTA (OSTIA UKMO); °C], [(e) to (h)] reconstructed vertical profiles of (e) temperature (°C), (f) Phosphate ($\mu\mathrm{g\,L^{-1}}$), (g) Silicate ($\mu\mathrm{g\,L^{-1}}$), and (h) Nitrate ($\mu\mathrm{g\,L^{-1}}$) at the C11 station in L104 on a three-daily time axis, and (i) the three-daily bin-averaged GOCI-derived chlorophyll concentrations ($\log_{10}$, $\mu\mathrm{g\,L^{-1}}$) along the cross-shore line (a green line in Figure 1a) for a period of one year (2013). The isopycnals are marked with a density interval of 0.5 $\mathrm{kg\,m^{-3}}$, and the constant density anomalies of 25.5 and 26.5 $\mathrm{kg\,m^{-3}}$ are highlighted with red. (b) to (d) and (i) are three-daily bin-averaged time series. Cross-shore locations of CTD stations are marked with horizontal gray lines, and odd number stations are only denoted. Two rectangular black boxes denote two time windows of seasonal chlorophyll blooms.

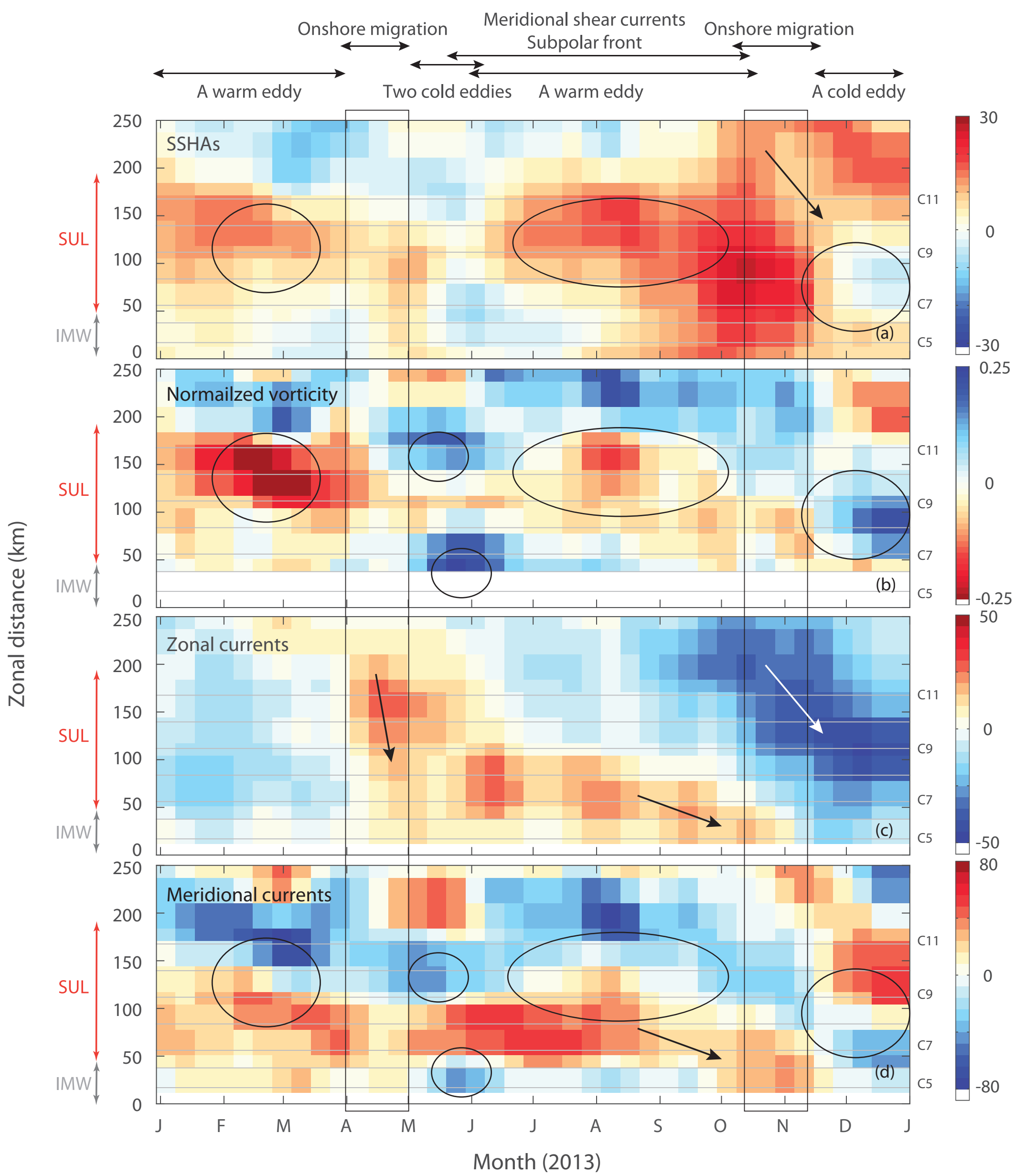

Onshore migration
Meridional shear currents
Subpolar front
Onshore migration
A warm eddy
Two cold eddies
A warm eddy
A cold eddy
SSHAs
Normailzed vorticity
Zonal currents
Meridional currents
Zonal distance (km)
SUL
IMW
250
200
150
100
50
0
C11
C9
C7
C5
(a)
(b)
(c)
(d)
30
0
-30
0.25
0
-0.25
50
0
-50
80
0
-80
J F M A M J J A S O N D J
Month (2013)

Figure 8. (a) to (d): Ten-daily bin-averaged time series of the ALT-derived mesoscale (a) sea surface height anomalies (SSHAs; η_M, cm), (b) normalized vorticity [$\xi_\mathsf{M} = \zeta/|f_c|$, where ζ and f_c denote the vertical component of relative vorticity ($\zeta = \partial v/\partial x - \partial u/\partial y$) and the local Coriolis frequency, respectively], (c) zonal geostrophic current component (u_M, cm s^{-1}), and (d) meridional geostrophic current component (v_M, cm s^{-1}) along the cross-shore line (Figure 1a). Circles and ellipses denote the rotational features including eddies and stretched shear currents or fronts. Details of the primary phenomena and relevant time windows are described on the top of each column. Positive SSHAs ($\eta > 0$; red), negative stream function ($\psi < 0$; red), and negative vorticity ($\xi < 0$; red) indicate clockwise rotational flows, and negative SSHAs ($\eta < 0$; blue), positive stream function ($\psi > 0$; blue), and positive vorticity ($\xi > 0$; blue) indicate counter-clockwise rotational flows. Note that the colorbars have different color ranges and edge colors. Black and white arrows indicate propagating features in the cross-shore direction. Cross-shore locations of CTD stations are marked with horizontal gray lines, and odd number stations are only denoted. Gray and white patches indicate observations with missing data and no observations, respectively. Two rectangular black boxes denote two time windows of seasonal chlorophyll blooms.

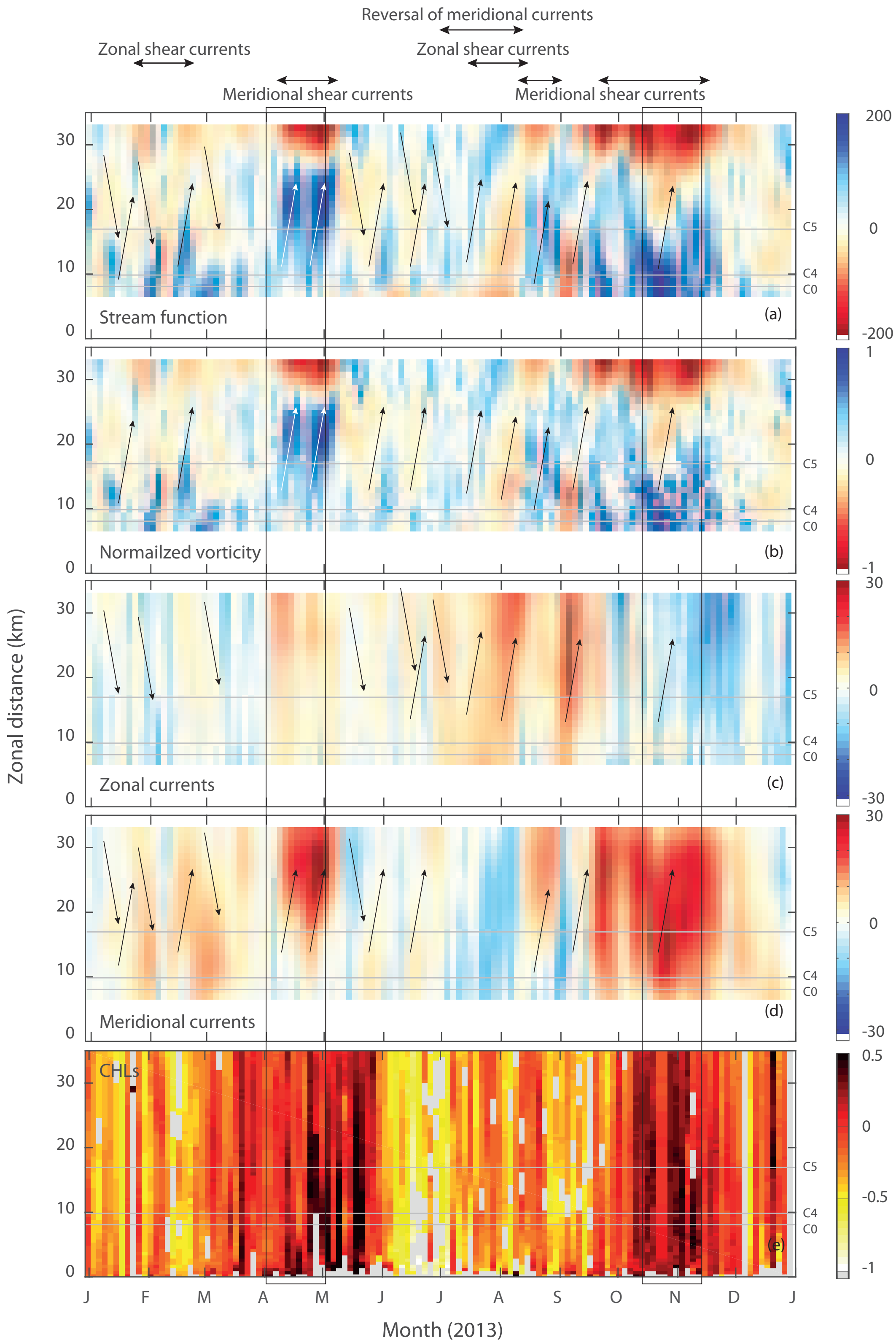
Reversal of meridional currents
Zonal shear currents
Zonal shear currents
Meridional shear currents
Meridional shear currents
Stream function
(a)
Normailzed vorticity
(b)
Zonal currents
(c)
Meridional currents
(d)
CHLs
(e)
Zonal distance (km)
Month (2013)
J F M A M J J A S O N D J
C5
C4
C0
200
0
-200
1
0
-1
30
0
-30
30
0
-30
0.5
0
-0.5
-1

Figure 9. (a) to (d): Three-daily bin-averaged time series of the HFR-derived submesoscale surface (a) stream function (ψ_S, $m^2\,s^{-1}$), (b) normalized vorticity (ξ_S), (c) zonal current component (u_S), and (d) meridional current component (v_S) along the cross-shore line (Figure 1a) [(b) and (d) are excerpted from *Yoo et al.* [2018]]. (e) Three-daily bin-averaged time series of the GOCI-derived chlorophyll concentrations along the cross-shore line (Figure 1a). Details of the primary phenomena and relevant time windows are described on the top of each column. Positive SSHAs ($\eta > 0$; red), negative stream function ($\psi < 0$; red), and negative vorticity ($\xi < 0$; red) indicate clockwise rotational flows, and negative SSHAs ($\eta < 0$; blue), positive stream function ($\psi > 0$; blue), and positive vorticity ($\xi > 0$; blue) indicate counter-clockwise rotational flows. Note that the colorbars have different color ranges and edge colors. Black and white arrows indicate propagating features in the cross-shore direction. Cross-shore locations of CTD stations are marked with horizontal gray lines, and odd number stations are only denoted. Gray and white patches indicate observations with missing data and no observations, respectively. Two rectangular black boxes denote two time windows of seasonal chlorophyll blooms.

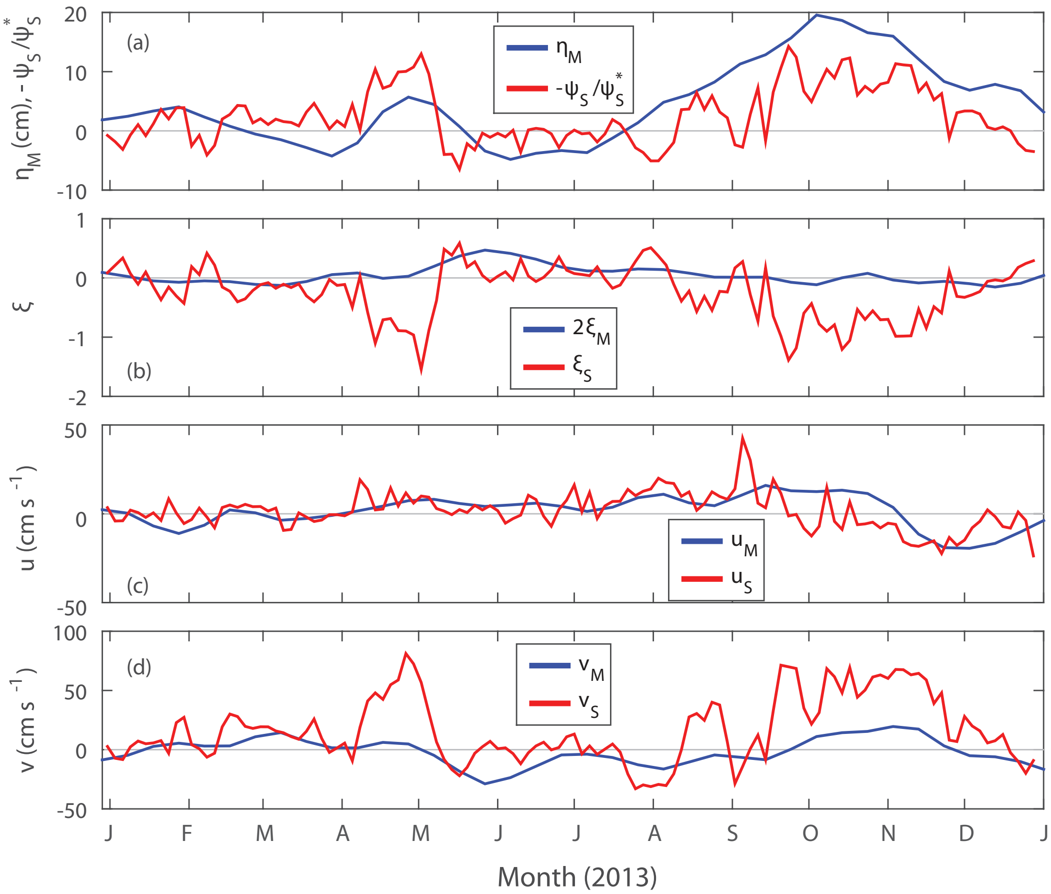

Figure 10. A comparison of time series of (a) sea surface height anomalies (η_M, cm) and scaled stream function ($\psi_\mathrm{S}/\psi_\mathrm{S}^*$, $\psi_\mathrm{S}^* = 200\ \mathrm{m^2\,s^{-1}}$), (b) normalized vorticity ($2\xi_\mathrm{M}$ and ξ_S), (c) zonal current components (u_M and u_S, $\mathrm{cm\,s^{-1}}$), and (d) meridional current components (v_M and v_S, $\mathrm{cm\,s^{-1}}$). The 10-daily bin-averaged ALT-derived mesoscale and three-daily bin-averaged HFR-derived submesoscale properties are compared. Notet that as the stream function has an opposite sign convention to the SSHA, the sign of the stream function is reversed. Note that the mesoscale vorticity fields are estimated finite differences of geostrophic current fields and are scaled up ($2\xi_\mathrm{M}$) for a comparison of two variables.

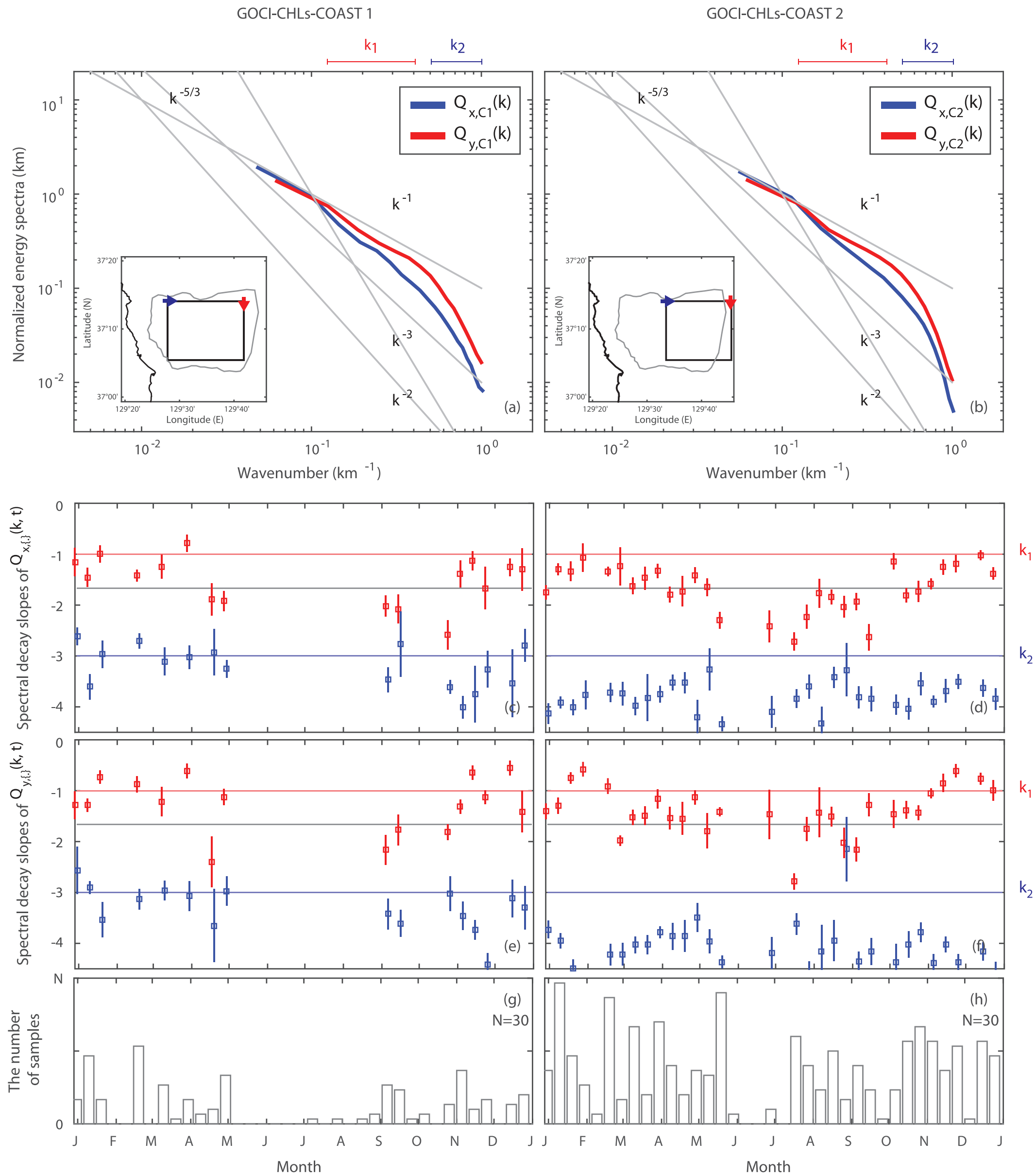

GOCI-CHLs-COAST 1
GOCI-CHLs-COAST 2
k1
k2
Normalized energy spectra (km)
Wavenumber (km -1)
Q x,C1(k)
Q y,C1(k)
Q x,C2(k)
Q y,C2(k)
k -5/3
k -1
k -3
k -2
(a)
(b)
Latitude (N)
Longitude (E)
Spectral decay slopes of Q x,{.}(k, t)
Spectral decay slopes of Q y,{.}(k, t)
(c)
(d)
(e)
(f)
The number of samples
(g)
N=30
(h)
N=30
J F M A M J J A S O N D J
Month

Figure 11. (a) and (b): Wavenumber domain energy spectra of GOCI-derived normalized chlorophyll concentrations (CHLs) for a period of five years (2011 to 2015) in two coastal regions – (a) an area completely overlapped with HFR-derived surface currents [$\mathcal{Q}_{\{\cdot\},\mathsf{C1}}(k)$, IMW] and (b) an area off 35 km from the coast [$\mathcal{Q}_{\{\cdot\},\mathsf{C2}}(k)$, IMW]. The energy spectra of the chlorophyll concentrations sampled on multiple one-dimensional cross-shore lines (x) are averaged in the along-shore direction (y) to estimate the wavenumber domain energy spectrum $[\mathcal{Q}_x(k)]$ in the cross-shore direction. Similarly, $\mathcal{Q}_y(k)$ is the cross-shore-directional (x) average of the energy spectra estimated from surface currents sampled in the along-shore direction (y). Four gray auxiliary lines of k^{-1}, $k^{-5/3}$, k^{-2}, and k^{-3} spectral decay slopes are overlaid. (c) and (d): Spectral decay slopes of $\mathcal{Q}_{x,\{\cdot\}}(k,t)$. (e) and (f): Spectral decay slopes of $\mathcal{Q}_{y,\{\cdot\}}(k,t)$. Spectral decay slopes are estimated from the individual energy spectra of chlorophyll concentrations at each realization using a least-squares fit in the wavenumber ranges [$0.1 \leq k_1 \leq 0.4$ km^{-1} (red), and $0.5 \leq k_2 \leq 1$ km^{-1} (blue) for both $\mathcal{Q}_x(k,t)$ and $\mathcal{Q}_y(k,t)$]. The temporal mean and standard errors of the estimated spectral decay slopes are 10-daily bin-averaged and presented with a colored square and vertical line, respectively. The expected spectral decay slopes [k^{-1} (red), $k^{-5/3}$ (black), and k^{-3} (blue)] are marked with colored horizontal lines. (g) and (h): The number of chlorophyll concentration maps participating in estimating the spectral decay slope of the energy spectra in Figures 11c and 11f ($N = 30$; The bin size is equal to 10 days).

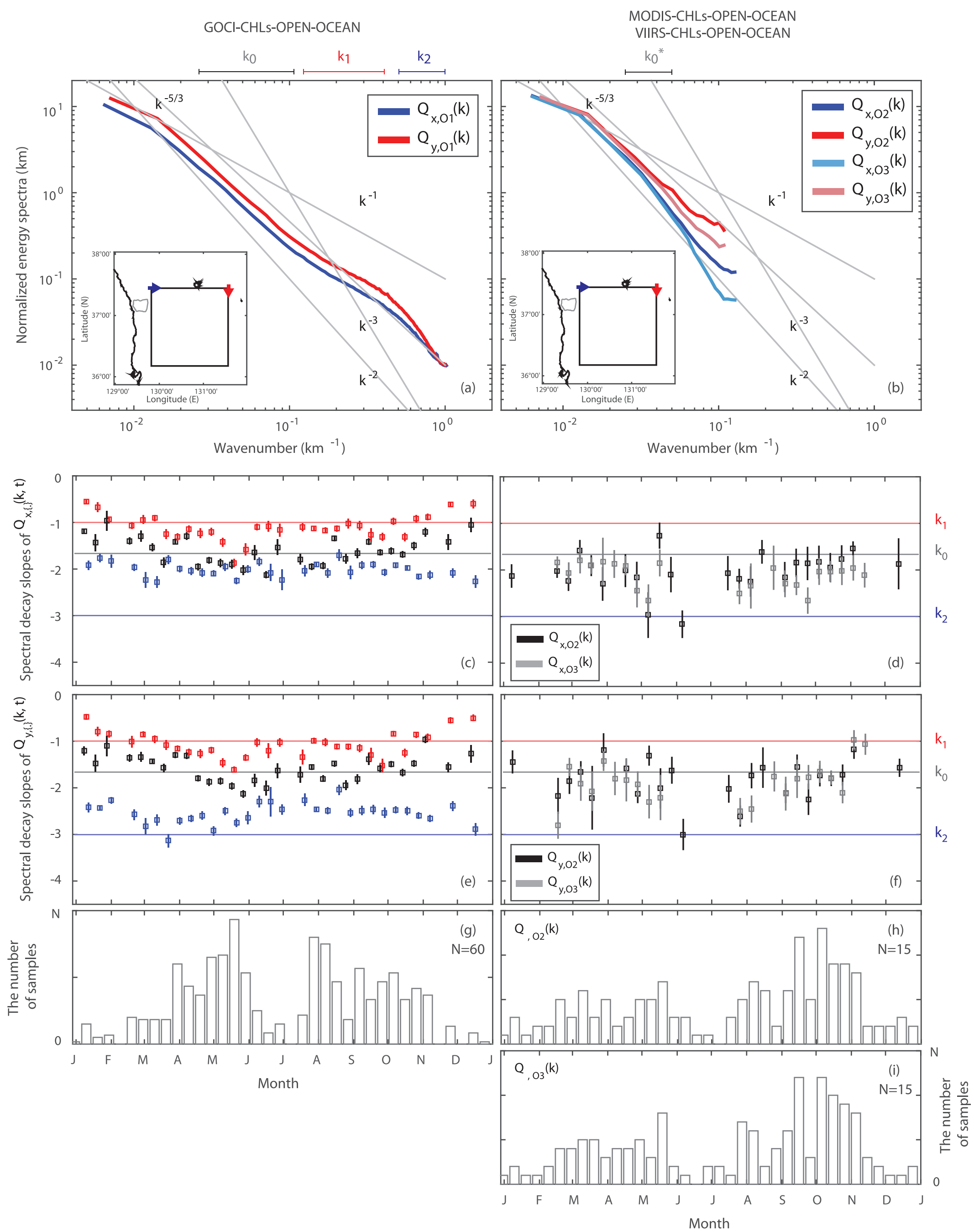

GOCI-CHLs-OPEN-OCEAN
MODIS-CHLs-OPEN-OCEAN
VIIRS-CHLs-OPEN-OCEAN
k0
k1
k2
k0*
Normalized energy spectra (km)
Wavenumber (km -1)
Qx,O1(k)
Qy,O1(k)
Qx,O2(k)
Qy,O2(k)
Qx,O3(k)
Qy,O3(k)
k-5/3
k-1
k-3
k-2
Latitude (N)
Longitude (E)
(a)
(b)
Spectral decay slopes of Qx,{.}(k, t)
Spectral decay slopes of Qy,{.}(k, t)
(c)
(d)
(e)
(f)
The number of samples
(g)
N=60
(h)
N=15
(i)
N=15
J F M A M J J A S O N D J
Month

Figure 12. (a) and (b): Wavenumber domain energy spectra of normalized chlorophyll concentrations (CHLs) for a period of five years (2011 to 2015) in the open ocean area [$\mathcal{Q}_{\{\cdot\},\mathsf{O}}(k)$, SUL]. (a) GOCI-derived chlorophyll concentrations [2011 to 2015; $\mathcal{Q}_{\{\cdot\},\mathsf{O1}}(k)$]. (b) MODIS-derived chlorophyll concentrations [2011 to 2015; $\mathcal{Q}_{\{\cdot\},\mathsf{O2}}(k)$] and VIIRS-derived chlorophyll concentrations [2012 to 2015; $\mathcal{Q}_{\{\cdot\},\mathsf{O3}}(k)$]. The energy spectra of the chlorophyll concentrations sampled on multiple one-dimensional cross-shore lines (x) are averaged in the along-shore direction (y) to estimate the wavenumber domain energy spectrum $[\mathcal{Q}_x(k)]$ in the cross-shore direction. Similarly, $\mathcal{Q}_y(k)$ is the cross-shore-directional (x) average of the energy spectra estimated from surface currents sampled in the along-shore direction (y). Four gray auxiliary lines of k^{-1}, $k^{-5/3}$, k^{-2}, and k^{-3} spectral decay slopes are overlaid. (c) and (d): Spectral decay slopes of $\mathcal{Q}_{x,\{\cdot\}}(k,t)$. (e) and (f): Spectral decay slopes of $\mathcal{Q}_{y,\{\cdot\}}(k,t)$. Spectral decay slopes are estimated from the individual energy spectra of chlorophyll concentrations at each realization using a least-squares fit in the wavenumber ranges [$0.018 \leq k_0 \leq 0.11$ km^{-1} (black), $0.018 \leq k_0^* \leq 0.05$ km^{-1} (black), $0.1 \leq k_1 \leq 0.4$ km^{-1} (red), and $0.5 \leq k_2 \leq 1$ km^{-1} (blue) for both $\mathcal{Q}_x(k,t)$ and $\mathcal{Q}_y(k,t)$]. The temporal mean and standard errors of the estimated spectral decay slopes are 10-daily bin-averaged and presented with a colored square and vertical line, respectively. The expected spectral decay slopes [k^{-1} (red), $k^{-5/3}$ (black), and k^{-3} (blue)] are marked with colored horizontal lines. (g) to (i): The number of chlorophyll concentration maps participating in estimating the spectral decay slope of the energy spectra in Figures 12e and 12f (The bin size is equal to 10 days). The maximum range (N) of individual histograms is noted. (g) $N = 60$. (h) and (i): $N = 15$.

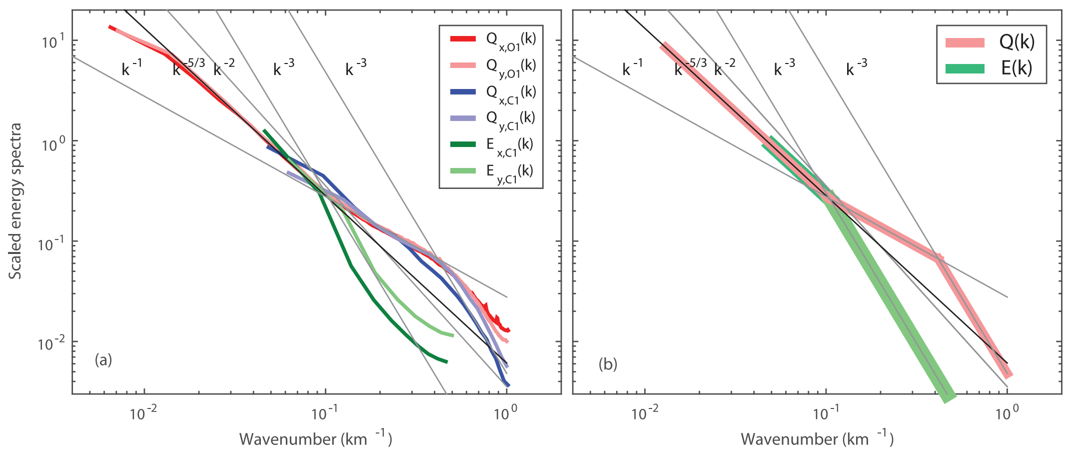

758 **Figure 13.** (a) Scaled wavenumber domain energy spectra of the the GOCI-derived chlorophyll concentrations [$\mathcal{Q}(k)$] and HFR-derived surface currents [$\mathcal{E}(k)$; excerpt from *Yoo et al.* [2018]]. (b) Primary decay slopes in the scaled wavenumber domain energy spectra of surface concentrations and surface currents are highlighted, analogous to Fig. 8.13b in *Vallis* [2006]. Three gray auxiliary lines of k^{-1}, k^{-2}, and k^{-3} spectral decay slopes and a black line of a $k^{-5/3}$ spectral decay slope are overlaid.

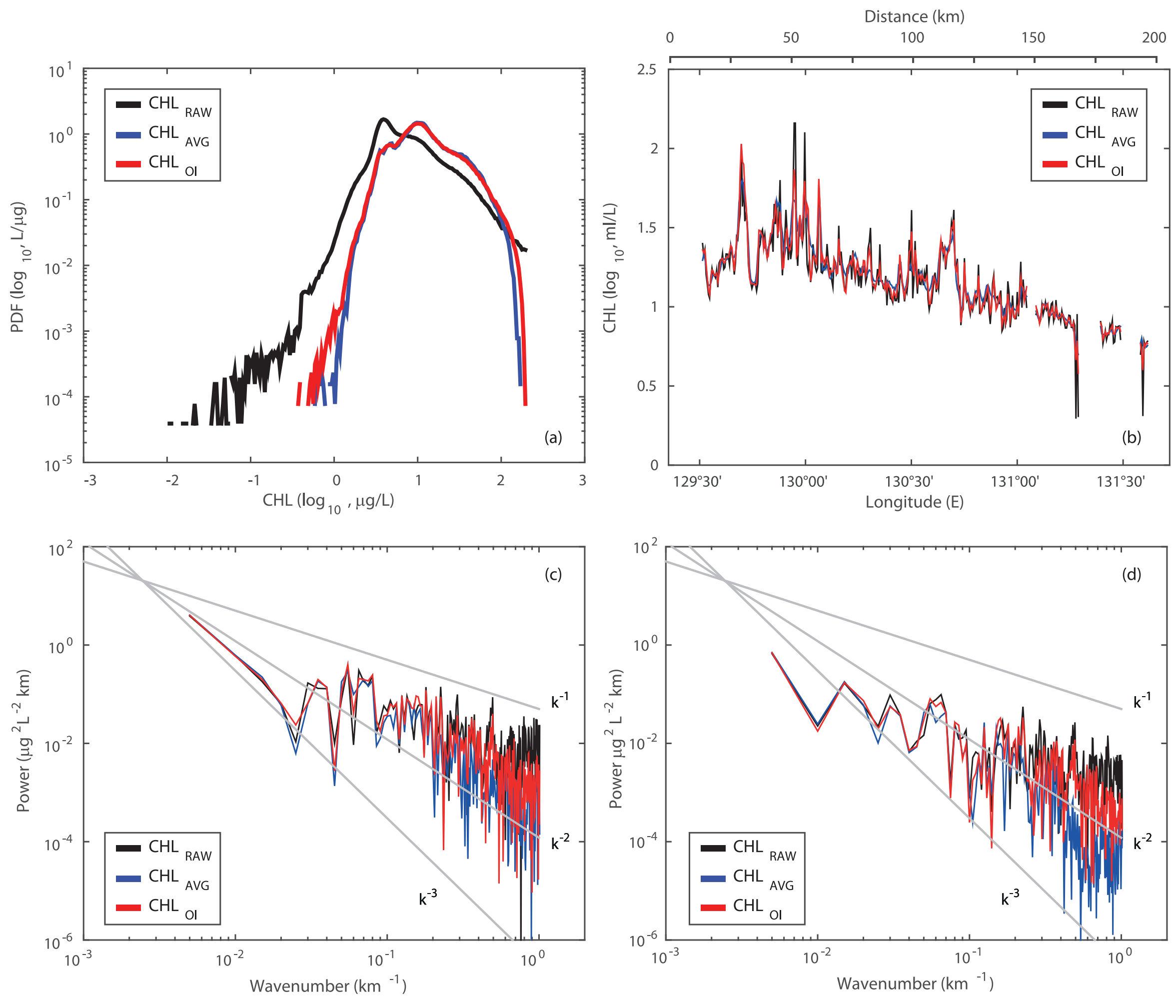

Figure A1. (a) PDFs of the non-orthogonally sampled raw (black), spatially-averaged (blue), and OI-mapped (red) chlorophyll concentrations in the entire domain in Figure 1a. (b) A direct comparison of three chlorophyll concentration data along the cross-shore line in Figure 1a, (c) and (d): Wavenumber domain energy spectra of three chlorophyll concentration data (c) without using a window function and (d) using a Hanning window function. Gray auxiliary lines denote decay slopes of k^{-1}, k^{-2}, and k^{-3}.

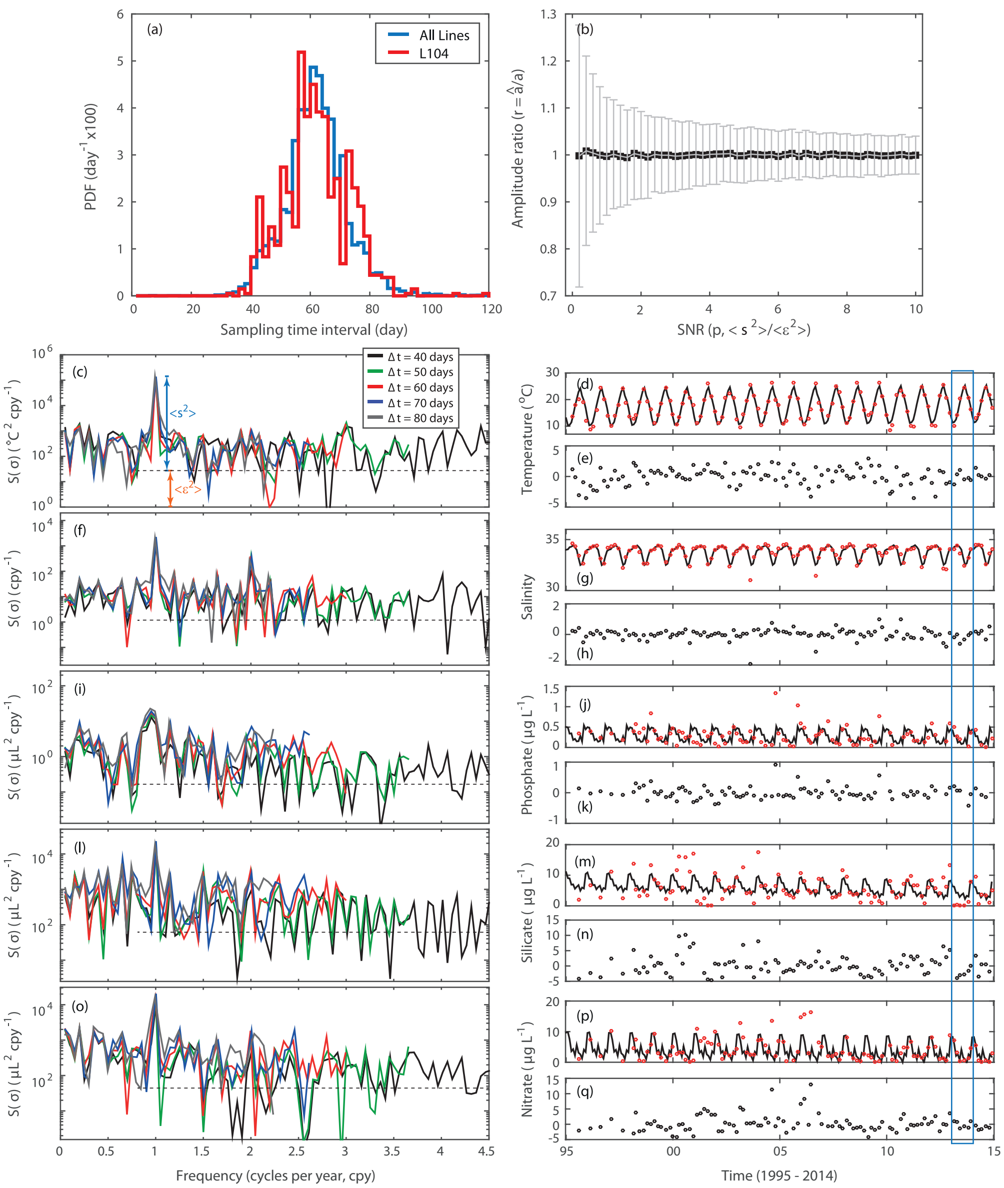

(a)
All Lines
L104
PDF (day^{-1} x100)
Sampling time interval (day)
(b)
Amplitude ratio (r = â/a)
SNR (p, < s^2>/<ε^2>)
(c)
Δt = 40 days
Δt = 50 days
Δt = 60 days
Δt = 70 days
Δt = 80 days
<s^2>
<ε^2>
S(σ) (°C^2 cpy^{-1})
(f)
S(σ) (cpy^{-1})
(i)
S(σ) (μL^2 cpy^{-1})
(l)
(o)
Frequency (cycles per year, cpy)
(d)
(e)
Temperature (°C)
(g)
(h)
Salinity
(j)
(k)
Phosphate (μg L^{-1})
(m)
(n)
Silicate (μg L^{-1})
(p)
(q)
Nitrate (μg L^{-1})
Time (1995 - 2014)

Figure B1. (a) PDFs of sampling intervals obtained from the temperature, salinity, and nutrient profiles at all Lines (blue) and Line 104 (red) for a period of recent 20 years (1995 to 2014). (b) Ensemble mean of ratios ($r = \langle \hat{a}/a \rangle$) of the estimated amplitude ($\hat{a}$) to the true amplitude (a in equation B.2) is presented as a function of SNR ($p = \langle s^2(t) \rangle / \langle \epsilon^2(t) \rangle$ in equation B.4) using randomly generated 1,000 ensemble members. (c), (f), (i), (l), and (o): Frequency-domain energy spectra [$S(\sigma)$] of the reconstructed time series of the temperature, salinity, phosphate, silicate, and nitrate, sampled at the surface ($z = 0$ m) of the C7 station on Line 104, using slow FFT are presented as a function of constant time intervals ($\Delta t = 40$, 50, 60, 70, and 80 days). As an example, the estimated signal variance ($\langle s^2 \rangle$) and noise variance ($\langle \epsilon^2 \rangle$) at the seasonal frequency are marked in Figure B1c. The noise floor level of individual energy spectra are marked with dashed black lines in Figures B1c, B1f, B1i, B1l, and B1o. (d), (e), (g), (h), (j), (k), (m), (n), (p), and (q): Time series of the raw data (red circles), reconstructed data (black curve), and residuals (black circles) at the surface ($z = 0$ m) of the C7 station on Line 104. (c) to (e): Temperature (°C). (f) to (h): Salinity. (i) to (k): Phosphate (μg L^{-1}). (l) to (n): Silicate (μg L^{-1}). (o) to (q): Nitrate (μg L^{-1}). A blue rectangular box in (f) to (k) denotes the time window of 2013, which contains approximately bi-monthly sampled five to six records.

Table 1. Spectral decay slopes of the one-dimensional wavenumber-domain energy spectra of currents $[\mathcal{E}(k)]$ and concentrations $[\mathcal{Q}(k)]$ are listed in terms of geostrophic turbulence theories [quasi-geostrophic (QG), surface QG (sQG), and finite-depth sQG (fsQG) theories] and the directions of the energy pathways (inverse cascades, forward cascades, and surface dissipation) [e.g., *Vallis* [2006]; *Tulloch and Smith* [2006]]. Two length scales that delineate the inverse cascades toward large scales and forward cascades toward small scales and divide the forward cascades and surface dissipation are called as an injection scale (λ_I) and dissipation scale (λ_D), respectively.

Energy spectra	Inverse cascades			Forward cascades			Dissipation
	QG	sQG	fsQG	QG	sQG	fsQG	
$E(k)$	$k^{-5/3}$	k^{-1}	k^{-3}	k^{-3}	$k^{-5/3}$	$k^{-5/3}$	$k^{\leq -3}$
$Q(k)$	$k^{-5/3}$	k^{-2}	k^{-1}	k^{-1}	$k^{-5/3}$	$k^{-5/3}$	$k^{\leq -3}$

Table 2. Flag parameters for GOCI data post-processing. The data to satisfy the flag parameters are excluded in the optimally interpolated products. High order flag is a more strict QAQC procedure for scientific research.

Flag tag	Parameters
Flag1	Cloud or ice, Land mask, Atmospheric algorithm failure, Wrong spectral shape of data
Flag2	Iteration divergence, High solar zenith angle, Missing ancillary data, Negative Rayleigh corrected radiance, Cloud edge contamination, Existence of bright pixel, Unavailable pixel contamination, Missing slot information, Slot edge contamination, Non-calculable chlorophyll, Statistically unreliable distribution of chlorophyll
Flag3	Extremely turbid water, High satellite zenith angle, Ancillary warning flag, High ozone concentration, High wind speed, Epsilon (869, 745) is less than 0.95, Negative water leaving irradiance, Low water leaving irradiance, Turbid water

A: Optimal interpolation of the GOCI-derived chlorophyll concentrations

A.1 Formulation

The GOCI-derived products (e.g., concentrations of chlorophyll, CDOM, and TSS) report values sampled at unique longitudes and latitudes and contain missing data, which can be cumbersome for end users to analyze. Thus, the GOCI-derived products are optimally interpolated on a regular grid with a 0.005-degree resolution (approximately 0.5 km) using an exponential correlation function, which can minimize spatial smoothing and follow the original shape of the data covariance function. The estimates ($\hat{d}$) at the ith location in the regular grid are given by the following:

$$\hat{d} = \left[\sigma_{ji}^2 \rho\left(\Delta x_{ji}, \Delta y_{ji}\right)\right]^\dagger \left[\sigma_{jk}^2 \rho(\Delta x_{jk}, \Delta y_{jk}) + \delta_{jk}\gamma_k^2\right]^{-1} \mathbf{d}, \tag{A.1}$$

where $\mathbf{d}$ is the subset of the data participating in the estimate ($\hat{d} = \hat{d}_i$) at the ith grid point ($\mathbf{d} = [d_1, d_2, \cdots, d_L]^\dagger$ and $j, k = 1, 2, \cdots, L$), which can be identified as the data within a search radius from the ith grid point. In this paper, the search radius is chosen to be 1 km. σ^2 and γ^2 denote the model and error variances of the field, respectively. Because we adopt the correlation function as a function of distance, the search radius helps to reduce the computing time and redundant estimates. Regarding the correlation function, an exponential correlation function, that is frequently used for mapping submesoscale surface current fields [e.g., *Kim et al.* [2008, 2011]], is given as follows:

$$\rho(\Delta x, \Delta y) = \exp\left(-\sqrt{\frac{\Delta x^2}{\lambda_x^2} + \frac{\Delta y^2}{\lambda_y^2}}\right), \tag{A.2}$$

where λ_x and λ_y denote the decorrelation length scales in the x and y directions, respectively, and both are chosen to be 1 km.

The normalized uncertainty ($\hat{\kappa}$; $0 \leq \hat{\kappa} \leq 1$) of each estimate, which varies between zero (certain) and one (uncertain), can be used for quality control and quality assurance (QAQC) of the data by the end users prior to data analysis:

$$\hat{\kappa} = \kappa / \gamma^2, \tag{A.3}$$

where the uncertainty (κ; $0 \leq \kappa \leq \gamma^2$) in the optimal interpolation [e.g., *Kim et al.* [2008]] is given by:

$$\kappa = \frac{\gamma^2}{\sigma^2}\left(\mathrm{cov_{mm}} - \mathrm{cov}^{\dagger}_{\mathrm{dm}}\mathrm{cov}^{-1}_{\mathrm{dd}}\mathrm{cov_{dm}}\right). \tag{A.4}$$

A.2 Evaluation

The raw, spatially averaged, and OI-mapped chlorophyll concentrations are compared (Figure A1). The spatially averaged and OI-mapped fields have more clearly defined submesoscale surface features (e.g., frontal and eddy features) than the raw data because they may have less spatial noise and more gap-filled data. Note that the spatial average of chlorophyll is estimated from the nearest 10 samplings within 0.01-degree of the search radius. Although Figure A1a can be interpreted as showing that the spatially averaged data and OI-mapped data are superior to the raw data, the raw and OI-mapped data at the same locations do not show the clear increment of data associated with averaging and mapping based on a comparison of all three datasets along the cross-shore line (Figure A1b). Moreover, their wavenumber domain energy spectra exhibit similar variance and slightly different noise and decay slopes (Figures A1c and A1d). Thus, the OI-mapped chlorophyll can be interpreted as an improvement to highlight the submesoscale features, along with the reduction of spatial noise and filling in missing observations with optimal values.

Although the spatial averaging or linear interpolation can be another candidate for gridding, the OI can provide better estimates of uncertainty of the mapped data at a specific location and time and less spatial bias due to mapping from a non-orthogonal sample grid to an orthogonal grid. Additionally, mapping is conducted with the raw and log-scaled data, showing little difference in the results (not shown).

B: Uncertainty estimates of the climatology

The climatologies of temperature, salinity, and nutrient profiles are derived from a multivariate regression analysis (Figures 4 and 5). Since the detailed descriptions of the methods can be found in *Kim and Cornuelle* [2015], we focus on the uncertainty estimates of the derived climatology of nutrients (phosphate, silicate, and nitrate) using the signal-to-noise ratio of the data.

B.1 Signal-to-noise ratio estimates

To evaluate the signal-to-noise ratio of the given time series, we generate a time series with a pure seasonal variance and an assumed noise as a substitute for the true time series,

$$d(t) = a \sin(\sigma t) + \epsilon(t), \tag{B.1}$$

$$= s(t) + \epsilon(t), \tag{B.2}$$

where a is the amplitude of the signal [$\sigma = 2\pi/365.2425$ cycles per day (cpd)]. Then, the signals are resampled at the time stamps ($\tilde{t}$) with statistics identical to the observed time series to examine how well the original variance can be reconstructed:

$$d(\tilde{t}) = a \sin(\sigma \tilde{t}) + \epsilon(\tilde{t}). \tag{B.3}$$

The signal-to-noise ratio of the data is defined as

$$p = \frac{\langle s^2(t) \rangle}{\langle \epsilon^2(t) \rangle}, \tag{B.4}$$

where $\langle \cdot \rangle$ indicates the ensemble mean. To increase the degrees of freedom in the error estimate, the time axis ($\tilde{t}$ in equation B.5) for resampling can be created from the cumulative sum of the random combinations of the time intervals (Δt_j; $j = 1, 2, \cdots, M-1$) of the observed time series:

$$\tilde{t}(k) = \mathop{}\limits_{j=1}^{k} \Delta t_j, \quad \tilde{t} \leq L, \tag{B.5}$$

where L denotes the maximum length of the time series ($L = 20$ years), and M indicates the number of time records. The PDF of the sampling time intervals of the data sampled from Line 104 follows nearly Gaussian statistics, and their mean and standard deviation are equal to 62.04 and 20.2 days, respectively (Figure B1a).

The evaluation that the original variance can be reconstructed is conducted with 1,000 independent realizations, and the ensemble mean of the ratios of the estimated amplitudes relative to the true amplitudes is presented as a function of the signal-to-noise ratio (Figure B1b):

$$r(p) = \langle \frac{\hat{a}(p)}{a(p)} \rangle. \tag{B.6}$$

B.2 Uncertainty estimates using slow FFT

The frequency-domain energy spectra of the irregularly sampled time series can be estimated with the slow finite Fourier transform (FFT), which is a least-squares fit using all orthogonal basis functions (all available frequencies) and treats the missing data and unevenly sampled time records appropriately [see *Pawlowicz et al.* [2002] for harmonic analysis and *Kim et al.* [2010] and *Kim* [2014] for examples of the slow FFT]. The frequency axis in the slow FFT is defined as

$$\sigma_n = 2\pi\left(n - N^* - 1\right)\frac{N-1}{N}\frac{1}{t_N - t_1}, \tag{B.7}$$

where N denotes the number of time records in the newly defined and evenly spaced time axis, which can be determined between aliasing and oversampling of the data, which correspond to the lower and higher numbers of the evenly spaced time stamps. Moreover, t_N and t_1 can be chosen as the beginning and ending time stamps of the observations or a nominal time window, which can cover all observations, and

$$N^* = \lfloor N/2 \rfloor \tag{B.8}$$

where $\lfloor \cdot \rfloor$ indicates the greatest integer function (or floor function) ($n = 1, 2, \cdots, N$):

$$\lfloor x \rfloor = \max\left\{m \in \mathcal{Z} \mid m \leq x\right\}. \tag{B.9}$$

Under the fixed beginning and ending time stamps, the frequency-domain energy spectra are estimated for five cases of sampling time intervals (Δt = 40, 50, 60, 70, and 80 days) of the time axis (Figures B1c, B1f, B1i, B1l, and B1o), and the optimal time interval (Δt) of the new time axis was chosen as 60 days.

Based on the estimated energy spectra, the signal-to-noise ratios are estimated to be higher than 100 at the seasonal frequency and 5 at the seasonal harmonic frequencies for temperature, salinity, and nutrients (Figures B1c, B1f, B1i, B1l, and B1o), which indicates that the irregularly sampled data sets for 20 years can resolve the true variability within 10% error (Figure B1b). The uncertainties of the temperature and salinity at the seasonal and semi-seasonal frequencies have been reported as 2.5°C and 0.7 and 0.3°C and 0.1, respectively. Similarly, the uncertainties of phosphate, silicate, and nitrate at the seasonal frequency are estimated to be 0.06, 0.99, and 1.42 $\mu\mathrm{g\,L^{-1}}$, respectively. Since the semi-seasonal variance of nutrients may not be clearly quantified due to inter-annual variability (e.g., Figure B1j), their uncertainties at the semi-seasonal frequency are not included in this paper.

To evaluate the performance of the regression analysis, the time series of the raw data, reconstructed data, and residuals of the surface temperature, salinity, phosphate, silicate, and nitrate sampled at the C7 station on Line 104 are presented (Figures B1d, B1e, B1g, B1h, B1j, B1k, B1m, B1n, B1p, and B1q). Although the residuals can be significant to some degrees, the reconstructed time series follow the raw data well. The derived climatology of the temperature, salinity, and nutrients is barely influenced by the choice of prior in solving the inverse method for multivariate regression [e.g., *Kim and Cornuelle* [2015]].

Acknowledgments

Eun Ae Lee and Sung Yong Kim were supported by grants through Basic Science Research Program through the National Research Foundation (NRF), Ministry of Education (NRF-2017R1D1A1B03028285), 'Research for Applications of Geostationary Ocean Color Imager' through Korea Institute of Marine Science and Technology Promotion (KIMST), Ministry of Oceans and Fisheries, and the Disaster and Safety Management Institute, Ministry of Public Safety and Security (KCG-01-2017-05), Republic of Korea. This work is a part of the graduate studies of the first author. The geostationary ocean color imagery (GOCI) maps are obtained from the Korea Ocean Satellite Center (KOSC), Korea Institute of Ocean Science and Technology (KIOST), and the WERA HFR-derived surface currents are provided by the Marine Information Technology (MIT) Corporation. The LDAPS wind products, based on Unified Model in UK Met Office, are provided by the Korea Meteorological Administration (KMA). The altimeter products were produced by SSALTO/DUACS and distributed by Archiving, Validation and Interpretation of Satellite Oceanographic data (AVISO) with support from CNES. The daily and monthly Level 3 Moderate Resolution Imaging Spectroradiometer (MODIS) chlorophyll concentration data at a spatial resolution of 4 km were obtained from the NASA Earth Observing System Data and Information System (EOSDIS) Physical Oceanography Distributed Active Archive Center (PO DAAC) at the Jet Propulsion Laboratory, Pasadena, CA USA. We appreciate the valuable comments in a view of biological oceanography from Dr. Sin Jae Yoo and Se Jong Ju at KIOST and Prof. Sang Heon Lee at Pusan National University and the discussion on the energy spectra of the chlorophyll concentrations with Drs. Young Gyu Park and Yeon Sik Chang at KIOST. The surface current data used in the paper will be available in `http://efml.kaist.ac.kr/archive.html` to comply with the American Geophysical Union Publications Data Policy.

References

Armi, L., and P. Flament (1985), Cautionary remarks on the spectral interpretation of turbulent flows, *J. Geophys. Res.*, *90*(C6), 11,779–11,782, doi:10.1029/JC090iC06p11779.

Beckmann, A., and I. Hense (2007), Beneath the surface: Characteristics of oceanic ecosystems under weak mixing conditions–a theoretical investigation, *Prog. Oceanogr.*, *75*(4), 771–796, doi:10.1016/j.pocean.2007.09.002.

Behrenfeld, M. J., E. Boss, D. A. Siegel, and D. M. Shea (2005), Carbon-based ocean productivity and phytoplankton physiology from space, *Global Biogeochem. Cycle*, *19*(1), GB1006, doi:10.1029/2004GB002299.

Blumen, W. (1978), Uniform potential vorticity flow: Part I. Theory of wave interactions and two-dimensional turbulence, *J. Atmos. Sci.*, *35*(5), 774–783, doi:10.1175/1520-0469(1978)035<0774:UPVFPI>2.0.CO;2.

Boyce, D. G., M. R. Lewis, and B. Worm (2010), Global phytoplankton decline over the past century, *Nature*, *466*(7306), 591–596, doi:10.1038/nature09268.

Brody, S. R., and M. S. Lozier (2014), Changes in dominant mixing length scales as a driver of subpolar phytoplankton bloom initiation in the north atlantic, *Geophys. Res. Lett.*, *41*(9), 3197–3203, doi:10.1002/2014GL059707.

Byun, S.-K. (1989), Sea surface cold water near the southeastern coast of Korea: Wind effect, *J. Oceanol. Soc. Korea*, *24*, 121–131.

Callies, J., and R. Ferrari (2013), Interpreting energy and tracer spectra of upper-ocean turbulence in the submesoscale range (1 – 200 km), *J. Phys. Oceanogr.*, *43*(11), 2456–2474, doi:10.1175/JPO-D-13-063.1.

Callies, J., R. Ferrari, J. M. Klymak, and J. Gula (2015), Seasonality in submesoscale turbulence, *Nature Commun.*, *6*, doi:10.1038/ncomms7862.

Campbell, J. W. (1995), The lognormal distribution as a model for bio-optical variability in the sea, *J. Geophys. Res.*, *100*(C7), 13,237–13,254, doi:10.1029/95JC00458.

Campbell, J. W., and J. E. O'Reilly (1988), Role of satellites in estimating primary productivity on the northwest Atlantic continental shelf, *Cont. Shelf Res.*, *8*(2), 179–204, doi:10.1016/0278-4343(88)90053-2.

Chang, K.-I., N. G. Hogg, M.-S. Suk, S.-K. Byun, Y.-G. Kim, and K. Kim (2002), Mean flow and variability in the southwestern East Sea, *Deep-Sea Res. II*, *49*(12), 2261–2279, doi:10.1016/S0967-0637(02)00120-6.

Chang, K.-I., et al. (2004), Circulation and currents in the southwestern East/Japan Sea: Overview and review, *Prog. Oceanogr.*, *61*(2), 105–156, doi:10.1016/j.pocean.2004.06.005.

Chang, P.-H., C.-H. Cho, and S.-B. Ryoo (2011), Recent changes of mixed layer depth in the East/Japan Sea: 1994–2007, *Asia-Pacific J. of Atmos. Sci.*, *47*(5), 497–501, doi:10.1007/s13143-011-0034-7.

Charney, J. G. (1971), Geostrophic turbulence, *J. Atmos. Sci.*, *28*, 1087–1095, doi:10.1175/1520-0469(1971)028<1087:GT>2.0.CO;2.

Chiswell, S. M., J. Bradford-Grieve, M. G. Hadfield, and S. C. Kennan (2013), Climatology of surface Chlorophyll-a, autumn-winter and spring blooms in the southwest Pacific Ocean, *J. Geophys. Res.*, *118*(2), 1003–1018, doi:10.1002/jgrc.20088.

Cho, K.-D., T.-J. Bang, T.-B. Shim, and H.-S. Yu (1990), Three dimensional structure of the Ullung Warm Lens, *Bull. Korean Fish. Soc*, *23*(4), 323–333.

Choi, J.-K., Y. J. Park, J. H. Ahn, H.-S. Lim, J. Eom, and J.-H. Ryu (2012), GOCI, the world's first geostationary ocean color observation satellite, for the monitoring of temporal variability in coastal water turbidity, *J. Geophys. Res.*, *117*(C9), C09004, doi:10.1029/2012JC008046.

de Boyer Montégut, C., G. Madec, A. S. Fischer, A. Lazar, and D. Iudicone (2004), Mixed layer depth over the global ocean: An examination of profile data and a profile-based climatology, *J. Geophys. Res.*, *109*(C12), doi:10.1029/2004JC002378.

Demers, S., L. Legendre, and J.-C. Therriault (1986), *Tidal Mixing and Plankton Dynamics*, Chap. Phytoplankton responses to vertical tidal mixing, pp. 1–40, Wiley Online Library, doi:10.1029/LN017.

Denman, K., A. Okubo, and T. Platt (1977), The chlorophyll fluctuation spectrum in the sea, *Limnol. Oceanogr.*, *22*(6), 1033–1038, doi:10.4319/lo.1977.22.6.1033.

Denman, K. L. (1976), The variance spectrum of phytoplankton in a turbulent ocean, *J. Mar. Res.*, *34*, 593–601.

Denman, K. L., and M. R. Abbott (1988), Time evolution of surface Chlorophyll patterns from cross-spectrum anlaysis of satellite color images, *J. Geophys. Res.*, *93*(C6), 6789–6798, doi:10.1029/93JC02149.

Dong, S., J. Sprintall, S. T. Gille, and L. Talley (2008), Southern Ocean mixed-layer depth from Argo float profiles, *J. Geophys. Res.*, *113*(C6), C06013, doi:10.1029/2006JC004051.

Falkowski, P. G., R. T. Barber, and V. Smetacek (1998), Biogeochemical controls and feedbacks on ocean primary production, *Science*, *281*(5374), 200–206, doi:10.1126/science.281.5374.200.

Ferrari, R., and C. Wunsch (2009), Ocean circulation kinetic energy: Reservoirs, sources, and sinks, *Annu. Rev. Fluid Mech.*, *41*, 253–282, doi:10.1146/annurev.fluid.40.111406.102139.

Franks, P. J. (2005), Plankton patchiness, turbulent transport and spatial spectra, *Mar. Ecol. Prog. Ser.*, *294*, 295–309, doi:10.3354/meps294295.

Gage, K. S. (1979), Evidence for a $k^{-5/3}$ law inertial range in mesoscale two-dimensional turbulence, *J. Atmos. Sci.*, *36*(10), 1950–1954, doi:10.1175/1520-0469(1979)036<1950:EFALIR>2.0.CO;2.

Gower, J. F. R., K. L. Denman, and R. J. Holyer (1980), Phytoplankton patchiness indicates the fluctuation spectrum of mesoscale oceanic structure, *Nature*, *288*, 157–159, doi:10.1038/288157a0.

Grados, D., A. Bertrand, F. Colas, V. Echevin, A. Chaigneau, D. Gutiérrez, G. Vargas, and R. Fablet (2016), Spatial and seasonal patterns of fine-scale to mesoscale upper ocean dynamics in an eastern boundary current system, *Prog. Oceanogr.*, *142*, 105–116, doi:10.1016/j.pocean.2016.02.002.

Herman, A. W., and K. L. Denman (1979), Intrusions and vertical mixing at the shelf/slope water front south of Nova Scotia, *J. Fish Res. Board of Can.*, *36*(12), 1445–1453, doi:10.1139/f79-211.

Hodges, B. A., and D. L. Rudnick (2004), Simple models of steady deep maxima in chlorophyll and biomass, *Deep-Sea Res. I*, *51*(8), 999–1015, doi:/10.1016/j.dsr.2004.02.009.

Holloway, G. (1986), Eddies, waves, circulation, and mixing: Statistical geofluid mechanics, *Annu. Rev. Fluid Mech.*, *18*(1), 91–147, doi:10.1146/annurev.fl.18.010186.000515.

Holte, J., and L. Talley (2009), A new algorithm for finding mixed layer depths with applications to ARGO data and subantartic mode water formation, *J. Atmos. Oceanic Technol.*, *26*, 1920–1939, doi:10.1175/2009JTECHO543.1.

Hoskins, B. J. (1975), The geostrophic momentum approximation and the semi-geostrophic equations, *J. Atmos. Sci.*, *32*(2), 233–242, doi:10.1175/1520-0469(1975)032<0233:TGMAAT>2.0.CO;2.

Hu, D.-X., M.-C. Cui, Y.-X. Li, and T.-D. Qu (1991), On the Yellow Sea cold water mass-related circulation, *Yellow Sea Res.*, *4*, 79–88.

Huisman, J., P. van Oostveen, and F. J. Weissing (1999), Critical depth and critical turbulence: Two different mechanisms for the development of phytoplankton blooms, *Limnol. Oceanogr.*, *44*(7), 1781–1787, doi:10.4319/lo.1999.44.7.1781.

Hur, H., G. Jacobs, and W. Teague (1999), Monthly variations of water masses in the Yellow and East China Seas, November 6, 1998, *J. Oceanogr.*, *55*(2), 171–184, doi: 10.1023/A:1007885828278.

Jang, C.-J., K. Kim, and T.-B. Shim (1995), Short-term variation of the mixed layer in the Korea Strait in Autumn, *J. Oceanol. Soc. Korea*, *30*(5), 512–521.

Jo, C. O., J.-Y. Lee, K. Park, Y. H. Kim, and K.-R. Kim (2007), Asian dust initiated early spring bloom in the northern East/Japan Sea, *Geophys. Res. Lett.*, *34*(5), doi:10.1029/2006GL027395.

Joo, H., S. Son, J.-W. Park, J. J. Kang, J.-Y. Jeong, C. I. Lee, C.-K. Kang, and S. H. Lee (2015), Long-term pattern of primary productivity in the East/Japan Sea based on ocean color data derived from MODIS-Aqua, *Remote Sens..*, *8*(1), 25, doi::10.3390/rs8010025.

Kara, A. B., P. A. Rochford, and H. E. Hurlburt (2000), An optimal definition for ocean mixed layer depth, *J. Geophys. Res.*, *105*(C7), 16,803–16,821, doi:10.1029/2000JC900072.

Kim, C. H., and K. Kim (1983), Characteristics and origin of the cold water mass along the East coast of Korea, *J. Oceanol. Soc. Korea*, *18*, 73–83.

Kim, D.-J., S. Nam, H. R. Kim, W. M. Moon, and K. Kim (2005), Can near-inertial internal waves in the East Sea be observed by synthetic aperture radar?, *Geophys. Res. Lett.*, *32*(2), L02606, doi:10.1029/2004GL021532.

Kim, H.-C., S. Yoo, and I. S. Oh (2007), Relationship between phytoplankton bloom and wind stress in the sub-polar frontal area of the Japan/East Sea, *J. Marine Syst.*, *67*(3), 205–216, doi:10.1016/j.jmarsys.2006.05.016.

Kim, H. R., S. Ahn, and K. Kim (2001), Observations of highly nonlinear internal solitons generated by near-inertial internal waves off the East Coast of Korea, *Geophys. Res. Lett.*, *28*(16), 3191–3194, doi:10.1029/2001GL013130.

Kim, S. Y. (2010), Observations of submesoscale eddies using high-frequency radar-derived kinematic and dynamic quantities, *Cont. Shelf Res.*, *30*(15), 1639–1655, doi: 10.1016/j.csr.2010.06.011.

Kim, S. Y. (2014), A statistical description on the wind-coherent responses of sea surface heights off the U.S. West Coast, *Ocean Dyn.*, *64*(1), 29–46, doi:10.1007/s10236-013-0668-3.

Kim, S. Y., and B. D. Cornuelle (2015), Coastal ocean climatology of temperature and salinity off the Southern California Bight: Seasonal variability, climate index correlation, and linear trend, *Prog. Oceanogr.*, *138*, 136 – 157, doi:10.1016/j.pocean.2015.08.001.

Kim, S. Y., and P. M. Kosro (2013), Observations of near-inertial surface currents off Oregon: Decorrelation time and length scales, *J. Geophys. Res.*, *118*(7), 3723–3736, doi:10.1002/jgrc.20235.

Kim, S. Y., E. J. Terrill, and B. D. Cornuelle (2008), Mapping surface currents from HF radar radial velocity measurements using optimal interpolation, *J. Geophys. Res.*, *113*, C10023, doi:10.1029/2007JC004244.

Kim, S. Y., B. D. Cornuelle, and E. J. Terrill (2010), Decomposing observations of high-frequency radar derived surface currents by their forcing mechanisms: Decomposition techniques and spatial structures of decomposed surface currents, *J. Geophys. Res.*, *115*, C12007, doi:10.1029/2010JC006222.

Kim, S. Y., G. Gopalakrishnan, and A. Ponte (2015), Interpretation of coastal wind transfer functions with momentum balances derived from idealized numerical model simulations, *Ocean Dyn.*, *65*(1), 115 – 141, doi:10.1007/s10236-014-0766-x.

Kim, S. Y., et al. (2011), Mapping the U.S. West Coast surface circulation: A multiyear analysis of high-frequency radar observations, *J. Geophys. Res.*, *116*, C03011, doi:10.1029/2010JC006669.

Kim, S. Y., et al. (2013), Poleward propagating subinertial alongshore surface currents off the U.S. West Coast, *J. Geophys. Res.*, *118*(12), 6791 – 6806, doi:10.1002/jgrc.20400.

Kim, Y.-G., and K. Kim (1999), Intermediate waters in the East/Japan Sea, *J. Oceanogr.*, *55*(2), 123–132, doi:10.1023/A:1007877610531.

Kim, Y. H., and H. S. Min (2008), Seasonal and interannual variability of the North Korean Cold Current in the East Sea reanalysis data, *Ocean Polar Res.*, *30*, 21–31, doi:10.4217/OPR.2008.30.1.021.

Kim, Y. H., Y.-B. Kim, K. Kim, K.-I. Chang, S. J. Lyu, Y.-K. Cho, and W. J. Teague (2006), Seasonal variation of the Korea Strait Bottom Cold Water and its relation to the bottom current, *Geophys. Res. Lett.*, *33*(24), doi:10.1029/2006GL027625.

Kraichnan, R. H. (1967), Inertial ranges in two-dimensional turbulence, *Phys. Fluid*, *10*, 1417–1423, doi:10.1063/1.1762301.

Le Traon, P. Y., F. Nadal, and N. Ducet (1998), An improved mapping method of multisatellite altimeter data, *J. Atmos. Oceanic Technol.*, *15*(2), 522–534, doi:10.1175/1520-0426(1998)015<0522:AIMMOM>2.0.CO;2.

Lee, J. C. (1983), Variations of sea level and sea surface temperature associated with wind-induced upwelling in the southeast coast of Korea in summer, *J. Oceanol. Soc. Korea*, *18*(18), 149–160.

Lee, J. C., and K.-I. Chang (2014), Variability of the coastal current off Uljin in summer 2006, *Ocean Polar Res.*, *36*, 165–177, doi:10.4217/OPR.2014.36.2.165.

Lee, J.-C., and J.-Y. Na (1985), Structure of upwelling off the southeast coast of Korea, *J. Oceanol. Soc. Korea*, *20*(3), 6–19.

Lesieur, M., and R. Sadourny (1981), Satellite-sensed turbulent ocean structure, *Nature*, *294*, 673, doi:10.1038/294673a0.

Lie, H.-J., C.-H. Cho, J.-H. Lee, S. Lee, Y. Tang, and E. Zou (2001), Does the Yellow Sea Warm Current really exist as a persistent mean flow?, *J. Geophys. Res.*, *106*(C10), 22,199–22,210, doi:10.1029/2000JC000629.

Lim, J.-H., S. Son, J.-W. Park, J. H. Kwak, C.-K. Kang, Y. B. Son, J.-N. Kwon, and S. H. Lee (2012), Enhanced biological activity by an anticyclonic warm eddy during early spring in the East Sea (Japan Sea) detected by the geostationary ocean color satellite, *Ocean Sci. J.*, *47*(3), 377–385, doi:10.1007/s12601-012-0035-1.

Lucas, A. J., P. J. Franks, and C. L. Dupont (2011), Horizontal internal-tide fluxes support elevated phytoplankton productivity over the inner continental shelf, *Limnology and Oceanography: Fluids and Environments*, *1*(1), 56–74, doi:10.1215/21573698-1258185.

MacIntyre, S., and R. Jellison (2001), Nutrient fluxes from upwelling and enhanced turbulence at the top of the pycnocline in Mono Lake, California, *Hydrobiologia*, *1*(466), 13–29, doi:10.1007/978-94-017-2934-5_2.

Mahadevan, A., and A. Tandon (2006), An analysis of mechanism for submesoscale vertical motion at ocean fronts, *Ocean Model.*, *14*, 241–256, doi:10.1016/j.ocemod.2006.05.006.

Mann, K. H., and J. R. Lazier (2013), *Dynamics of marine ecosystems: Biological-physical interactions in the oceans*, 3rd ed., John Wiley & Sons, doi:10.1002/9781118687901, http://onlinelibrary.wiley.com/book/10.1002/9781118687901.

Maúre, E., J. Ishizaka, C. Sukigara, Y. Mino, H. Aiki, T. Matsuno, H. Tomita, J. Goes, and H. Gomes (2017), Mesoscale eddies control the timing of spring phytoplankton blooms: A case study in the japan sea, *Geophys. Res. Lett.*, doi:10.1002/2017GL074359.

McGillicuddy, D. J., A. R. Robinson, D. A. Siegel, H. W. Jannasch, R. Johnson, T. D. Dickey, J. McNeil, A. F. Michaels, and A. H. Knap (1998), Influence of mesoscale eddies on new production in the Sargasso Sea, *Nature*, *394*(6690), 263–266, doi: 10.1038/28367.

McGillicuddy, D. J., et al. (2007), Eddy/wind interactions stimulate extraordinary mid-ocean plankton blooms, *Science*, *316*(5827), 1021, doi:10.1126/science.1136256.

McWilliams, J. C. (2016), Submesoscale currents in the ocean, *Proc. R. Soc. Lond. A. Math. and Phys. Sci.*, *472*(2189), doi:10.1098/rspa.2016.0117.

Michaelsen, J., X. Zhang, and R. C. Smith (1988), Variability of pigment biomass in the California Current System as determined by satellite imagery: 2. Temporal variability, *J. Geophys. Res.*, *93*(D9), 10,883–10,896, doi:10.1029/JD093iD09p10883.

Mikelsons, K., M. Wang, L. Jiang, and M. Bouali (2014), Destriping algorithm for improved satellite-derived ocean color product imagery, *Optics express*, *22*(23), 28,058–28,070, doi:10.1364/OE.22.028058.

Min, H. S., Y.-H. Kim, and C.-H. Kim (2006), Year-to-year variation of cold waters around the Korea Strait, *Ocean Sci. J.*, *41*(4), 227–234, doi:10.1007/BF03020626.

Monterey, G., and S. Levitus (1997), Seasonal variability of mixed layer depth for the World Ocean, *Tech. Rep. 96*.

Nikurashin, M., G. Vallis, and A. Adcroft (2013), Routes to energy dissipation for geostrophic flows in the Southern Ocean, *Nature Geosci.*, *6*(1), 48–51, doi:10.1038/NGEO1657.

Obukhov, A. (1968), Structure of the temperature field in turbulent flow, *Tech. rep.*, Army Biological Labs Frederick, MD.

Ocean Biology Processing Group (2003), MODIS Aqua Level 3 Global Monthly Mapped 4 km Chlorophyll-a. Ver. 6, Dataset accessed [2017-01-27].

Omand, M. M., E. A. D'Asaro, C. M. Lee, M. J. Perry, N. Briggs, I. Cetinic, and A. Mahadevan (2015), Eddy-driven subduction exports particulate organic carbon from the spring bloom, *Science*, *348*(6231), 222–225, doi:10.1126/science.1260062.

Pawlowicz, R., B. Beardsley, and S. Lentz (2002), Classic tidal harmonic analysis including error estimates in MATLAB using T_TIDE, *Computers and Geosciences*, *28*, 929–

937.

Pinkel, R. (2014), Vortical and internal wave shear and strain, *J. Phys. Oceanogr.*, *44*(8), 2070–2092, doi:10.1175/JPO-D-13-090.1.

Powell, T. M., and A. Okubo (1994), Turbulence, diffusion and patchiness in the sea, *Philos. Trans. Roy. Soc. London Ser. B: Biologi. Sci.*, *343*(1303), 11–18, doi:10.1098/rstb.1994.0002.

Risien, C. M., and D. B. Chelton (2008), A global climatology of surface wind and wind stress fields from eight years of QuikSCAT scatterometer data, *J. Phys. Oceanogr.*, *38*(11), 2379–2413, doi:10.1175/2008JPO3881.1.

Robinson, I. S. (2004), *Measuring the oceans from space: The principles and methods of satellite oceanography*, Springer Science & Business Media.

Ryabov, A., and B. Blasius (2008), Population growth and persistence in a heterogeneous environment: the role of diffusion and advection, *Mathematical Modelling of Natural Phenomena*, *3*(3), 42–86, doi:10.1051/mmnp:2008064.

Rykaczewski, R., and D. Checkley (2008), Influence of ocean winds on the pelagic ecosystem in upwelling regions, *Proc. Natl. Acad. Sci.*, *105*(6), 1965–1970, doi:10.1073/pnas.0711777105.

Rykaczewski, R. R., and J. P. Dunne (2011), A measured look at ocean Chlorophyll trends, *Nature*, *472*(7342), E5–E6, doi:10.1038/nature09952.

Ryu, J.-H., H.-J. Han, S. Cho, Y.-J. Park, and Y.-H. Ahn (2012), Overview of geostationary ocean color imager (GOCI) and GOCI data processing system (GDPS), *Ocean Sci. J.*, *47*(3), 223–233, doi:10.1007/s12601-012-0024-4.

Shim, T.-B., and K. Kim (1981), On the variation of the mixed layer depth and the heat flux in the Sea of Japan, *J. Oceanol. Soc. Korea*, *16*(2), 49–56.

Shin, J.-W., J. Park, J.-G. Choi, Y.-H. Jo, J. J. Kang, H. Joo, and S. H. Lee (2017), Variability of phytoplankton size structure in response to changes in coastal upwelling intensity in the southwestern East Sea, *J. Geophys. Res.*, *122*(12), 10,262–10,274, doi:10.1002/2017JC013467.

Sigler, M. F., P. J. Stabeno, L. B. Eisner, J. M. Napp, and F. J. Mueter (2014), Spring and fall phytoplankton blooms in the eastern Bering Sea during 1995–2011, *Alaska Fisheries Science Center, quarterly report*, pp. 1–6, http://www.afsc.noaa.gov/Quarterly/AMJ2014/amj14featurelead.htm.

Smith, K. M., P. E. Hamlington, and B. Fox-Kemper (2016), Effects of submesoscale turbulence on ocean tracers, *J. Geophys. Res.*, *121*(1), 908–933, doi:10.1002/2015JC011089.

Soh, H. S., and S. Y. Kim (2018), Diagnostic characteristics of submesoscale coastal surface currents, *J. Geophys. Res.*, *123*, doi:10.1002/2017JC013428.

Son, Y. B., B.-J. Choi, Y. H. Kim, and Y.-G. Park (2015), Tracing floating green algae blooms in the Yellow Sea and the East China Sea using GOCI satellite data and Lagrangian transport simulations, *Remote Sens. Environ.*, *156*, 21–33, doi:10.1016/j.rse.2014.09.024.

Stark, J. D., C. J. Donlon, M. J. Martin, and M. E. McCulloch (2007), OSTIA: An operational, high resolution, real time, global sea surface temperature analysis system, in *Oceans 2007-Europe*, pp. 1–4, IEEE, doi:10.1109/OCEANSE.2007.4302251.

Strass, V. H. (1992), Chlorophyll patchiness caused by mesoscale upwelling at fronts, *Deep Sea Res.*, *39*(1), 75–96, doi:10.1016/0198-0149(92)90021-K.

Taylor, J. R., and R. Ferrari (2011a), Shutdown of turbulent convection as a new criterion for the onset of spring phytoplankton blooms, *Limnol. Oceanogr.*, *56*(6), 2293–2307, doi:10.4319/lo.2011.56.6.2293.

Taylor, J. R., and R. Ferrari (2011b), Ocean fronts trigger high latitude phytoplankton blooms, *Geophys. Res. Lett.*, *38*(23), doi:10.1029/2011GL049312.

Thomas, L. N., A. Tandon, and A. Mahadevan (2008), *Ocean Modeling in an Eddying Regime*, *Geophysical Monograph Series*, vol. 177, Chap. Submesoscale processes and dynamics, pp. 17–38, American Geophysical Union, Washington, D.C.

Thomson, R. E., and I. V. Fine (2003), Estimating mixed layer depth from oceanic profile data, *J. Atmos. Oceanic Technol.*, *20*(2), 319–329, doi:10.1175/1520-0426(2003)020<0319:EMLDFO>2.0.CO;2.

Townsend, D. W., L. M. Cammen, P. M. Holligan, D. E. Campbell, and N. R. Pettigrew (1994), Causes and consequences of variability in the timing of spring phytoplankton blooms, *Deep-Sea Res. I*, *41*(5), 747–765, doi:10.1016/0967-0637(94)90075-2.

Trusenkova, O., V. Lobanov, and D. Kaplunenko (2008), Variability of sea surface temperature in the Japan Sea and its relationship to the wind-curl field, *Izvestiya, Atmospheric and Oceanic Physics*, *44*(4), 517, doi:10.1134/S0001433808040129.

Tulloch, R., and K. Smith (2006), A theory for the atmospheric energy spectrum: Depth-limited temperature anomalies at the tropopause, *Proc. Natl. Acad. Sci.*, *103*(40), 14,690–14,694, doi:10.1073/pnas.0605494103.

Tulloch, R., and K. S. Smith (2009), Quasigeostrophic turbulence with explicit surface dynamics: Application to the atmospheric energy spectrum, *J. Atmos. Sci.*, *66*(2), 450–467, doi:10.1175/2008JAS2653.1.

Tulloch, R., J. Marshall, C. Hill, and K. S. Smith (2011), Scales, growth rates, and spectral fluxes of baroclinic instability in the ocean, *J. Phys. Oceanogr.*, *41*(6), 1057–1076, doi:10.1175/2011JPO4404.1.

Vallis, G. K. (2006), *Atmospheric and Oceanic Fluid Dynamics*, 745 pp., Cambridge University Press, Cambridge, U.K.

Wang, M., X. Liu, L. Tan, L. Jiang, S. Son, W. Shi, K. Rausch, and K. Voss (2013), Impacts of VIIRS SDR performance on ocean color products, *J. Geophys. Res.*, *118*(18), 10,347 – 10,360, doi:10.1002/jgrd.50793.

Warren, M., G. Quartly, J. Shutler, P. Miller, and Y. Yoshikawa (2016), Estimation of ocean surface currents from maximum cross correlation applied to GOCI geostationary satellite remote sensing data over the Tsushima (Korea) Straits, *J. Geophys. Res.*, *121*(9), 6993–7009, doi:10.1002/2016JC011814.

Wilson, C., and V. J. Coles (2005), Global climatological relationships between satellite biological and physical observations and upper ocean properties, *J. Geophys. Res.*, *110*(C10), C10001, doi:10.1029/2004JC002724.

Winder, M., and J. E. Cloern (2010), The annual cycles of phytoplankton biomass, *Philos. Trans. Roy. Soc. London Ser. B: Biologi. Sci.*, *365*(1555), 3215–3226, doi:10.1098/rstb.2010.012.

Wortham, C., J. Callies, and M. G. Scharffenberg (2014), Asymmetries between wavenumber spectra of along- and across-track velocity from tandem-mission altimetry, *J. Phys. Oceanogr.*, *44*(4), 1151–1160, doi:10.1175/JPO-D-13-0153.1.

Wunsch, C. (1997), The vertical partition of oceanic horizontal kinetic energy, *J. Phys. Oceanogr.*, *27*(8), 1770–1794, doi:10.1175/1520-0485(1997)027<1770:TVPOOH>2.0.CO;2.

Yang, H., J.-K. Choi, Y.-J. Park, H.-J. Han, and J.-H. Ryu (2014), Application of the Geostationary Ocean Color Imager (GOCI) to estimates of ocean surface currents, *J. Geophys. Res.*, *119*(6), 3988–4000, doi:10.1002/2014JC009981.

Yoo, J. G., S. Y. Kim, and H. S. Kim (2018), Spectral descriptions of submesoscale surface circulation in a coastal region, *J. Geophys. Res.*, submitted.

Yoo, S., and J. Park (2009), Why is the southwest the most productive region of the East Sea/Sea of Japan?, *J. Marine Syst.*, *78*(2), 301–315, doi:10.1016/j.jmarsys.2009.02.014.

Yoon, J.-H., K. Abe, T. Ogata, and Y. Wakamatsu (2005), The effects of wind-stress curl on the Japan/East Sea circulation, *Deep-Sea Res. II*, *52*(11), 1827–1844, doi:10.1016/j.dsr2.2004.03.004.

Yuan, W., and J. Zhang (2006), High correlations between Asian dust events and biological productivity in the western North Pacific, *Geophys. Res. Lett.*, *33*(7), doi:10.1029/2005GL025174.

Yun, J. Y., L. Magaard, K. Kim, C. W. Shin, C. Kim, and S. K. Byun (2004), Spatial and temporal variability of the North Korean Cold Water leading to the near-bottom cold water intrusion in Korea Strait, *Prog. Oceanogr.*, *60*(1), 99–131, doi:10.1016/j.pocean.2003.11.004.

Zang, X., and C. Wunsch (2001), Spectral description of low-frequency oceanic variability, *J. Phys. Oceanogr.*, *31*(10), 3073–3095, doi:10.1175/1520-0485(2001)031<3073:SDOLFO>2.0.CO;2.

Figure 1.

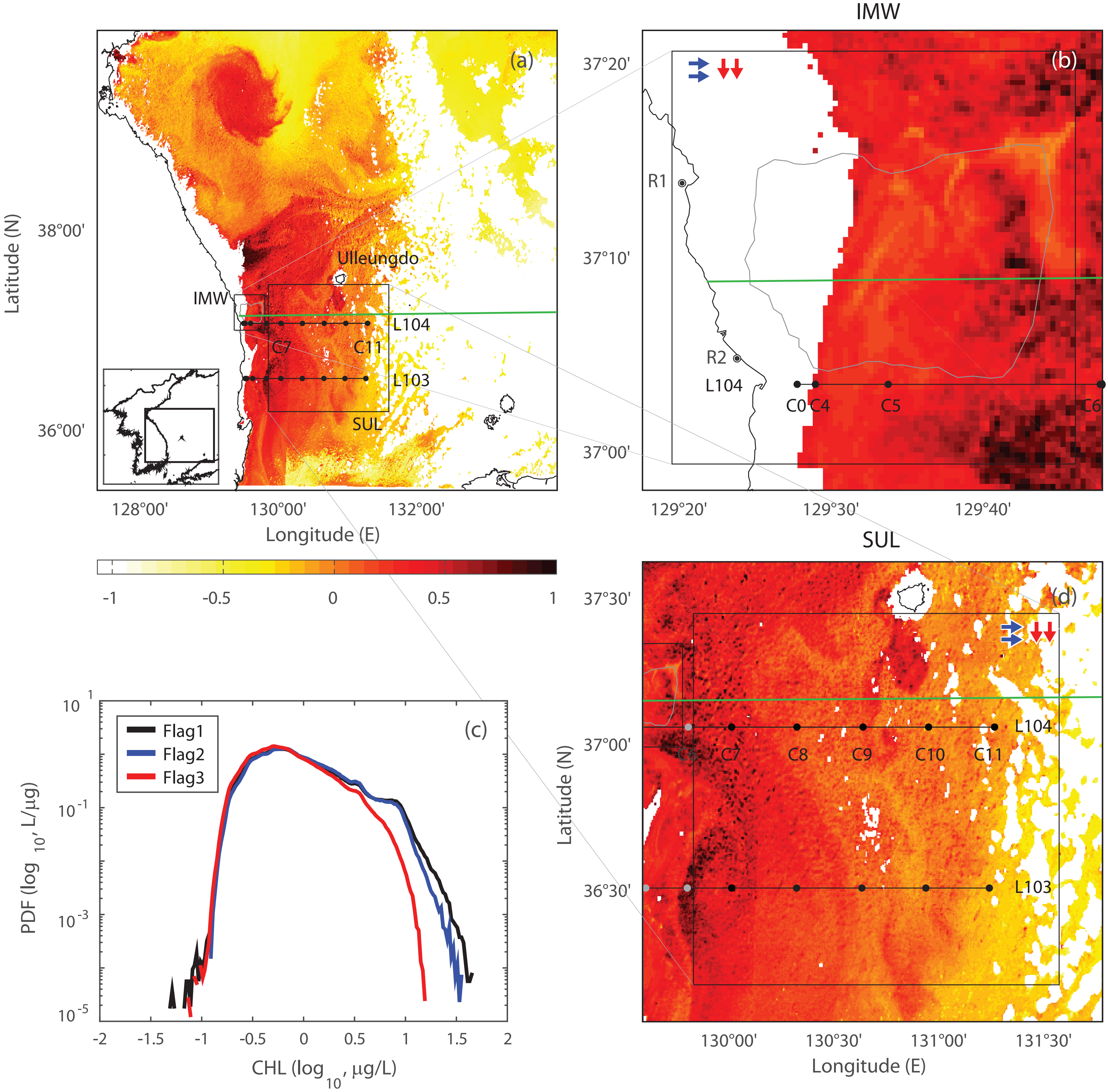

IMW
SUL
(a)
(b)
(c)
(d)
Ulleungdo
L104
L103
C7
C11
R1
R2
C0
C4
C5
C6
C8
C9
C10
Flag1
Flag2
Flag3
Latitude (N)
Longitude (E)
PDF (log10, L/µg)
CHL (log10, µg/L)
38°00'
36°00'
128°00'
130°00'
132°00'
37°20'
37°10'
37°00'
129°20'
129°30'
129°40'
37°30'
36°30'
130°30'
131°00'
131°30'

Figure 2.

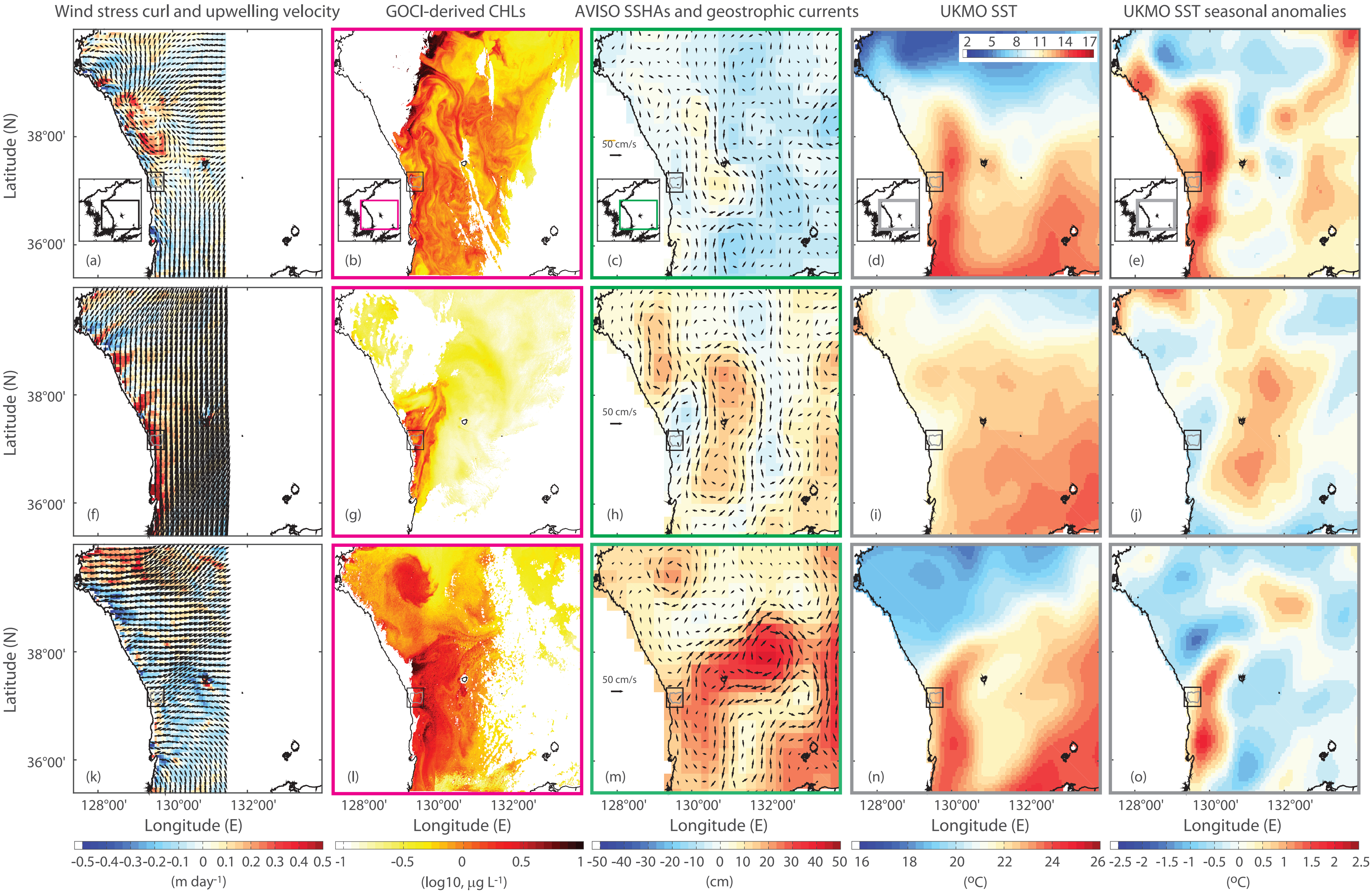

Wind stress curl and upwelling velocity
GOCI-derived CHLs
AVISO SSHAs and geostrophic currents
UKMO SST
UKMO SST seasonal anomalies
Latitude (N)
38°00'
36°00'
(a)
(b)
(c)
(d)
(e)
(f)
(g)
(h)
(i)
(j)
(k)
(l)
(m)
(n)
(o)
50 cm/s
2 5 8 11 14 17
128°00' 130°00' 132°00'
Longitude (E)
-0.5 -0.4 -0.3 -0.2 -0.1 0 0.1 0.2 0.3 0.4 0.5
(m day-1)
-1 -0.5 0 0.5 1
(log10, μg L-1)
-50 -40 -30 -20 -10 0 10 20 30 40 50
(cm)
16 18 20 22 24 26
(ºC)
-2.5 -2 -1.5 -1 -0.5 0 0.5 1 1.5 2 2.5
(ºC)

Figure 3.

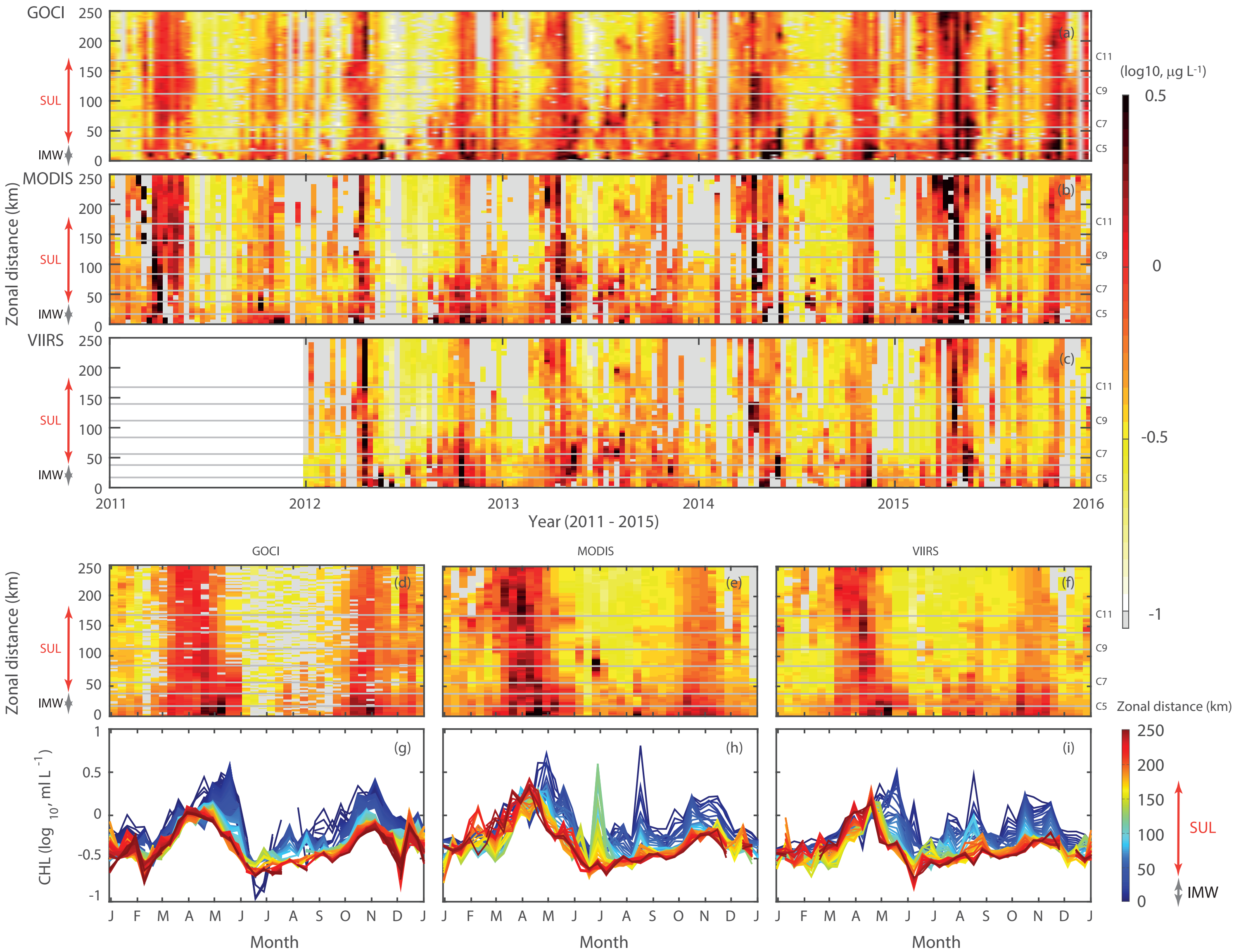

GOCI
MODIS
VIIRS
Zonal distance (km)
SUL
IMW
(a)
(b)
(c)
C11
C9
C7
C5
2011
2012
2013
2014
2015
2016
Year (2011 - 2015)
(log10, μg L-1)
0.5
0
-0.5
-1
(d)
(e)
(f)
(g)
(h)
(i)
CHL (log 10, ml L -1)
J F M A M J J A S O N D J
Month
Zonal distance (km)
250
200
150
100
50
0

Figure 4.

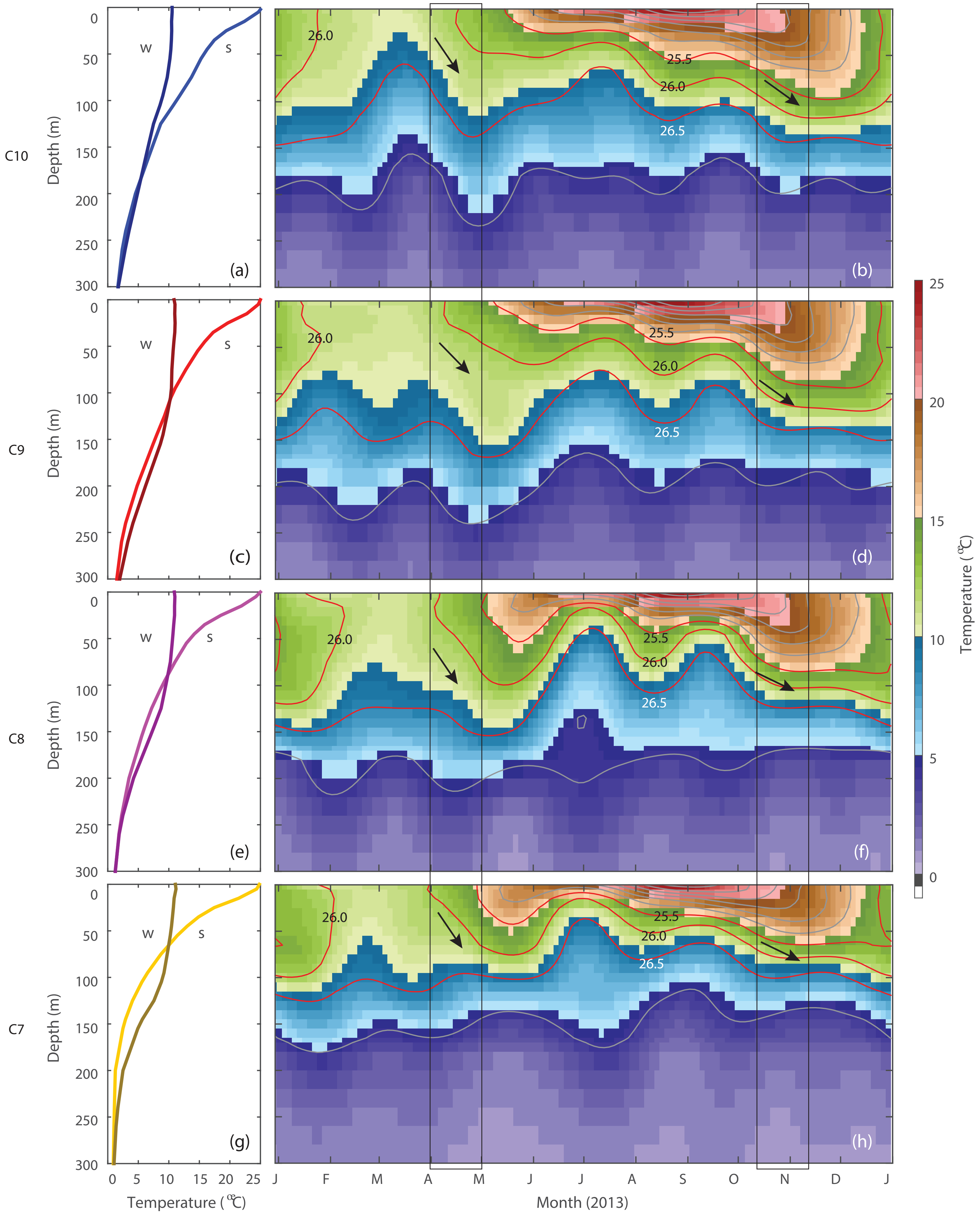
C10
C9
C8
C7
Depth (m)
Temperature (℃)
Month (2013)
(a)
(b)
(c)
(d)
(e)
(f)
(g)
(h)
w
s
26.0
25.5
26.5
J F M A M J J A S O N D J
0 5 10 15 20 25
0 50 100 150 200 250 300

Figure 5.

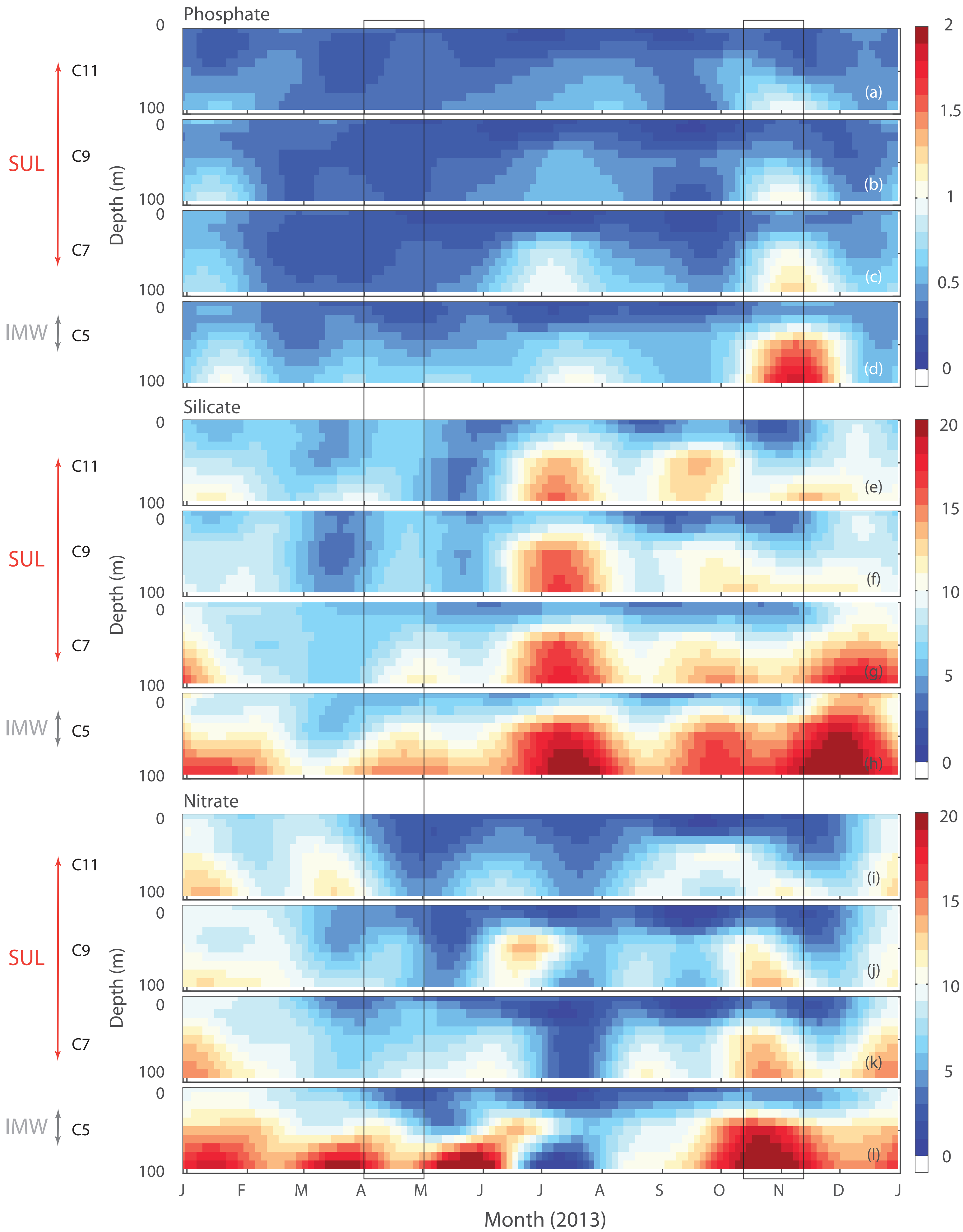

Phosphate
Silicate
Nitrate
SUL
IMW
C11
C9
C7
C5
Depth (m)
0
100
(a)
(b)
(c)
(d)
(e)
(f)
(g)
(h)
(i)
(j)
(k)
(l)
2
1.5
1
0.5
0
20
15
10
5
0
J F M A M J J A S O N D J
Month (2013)

Figure 6.

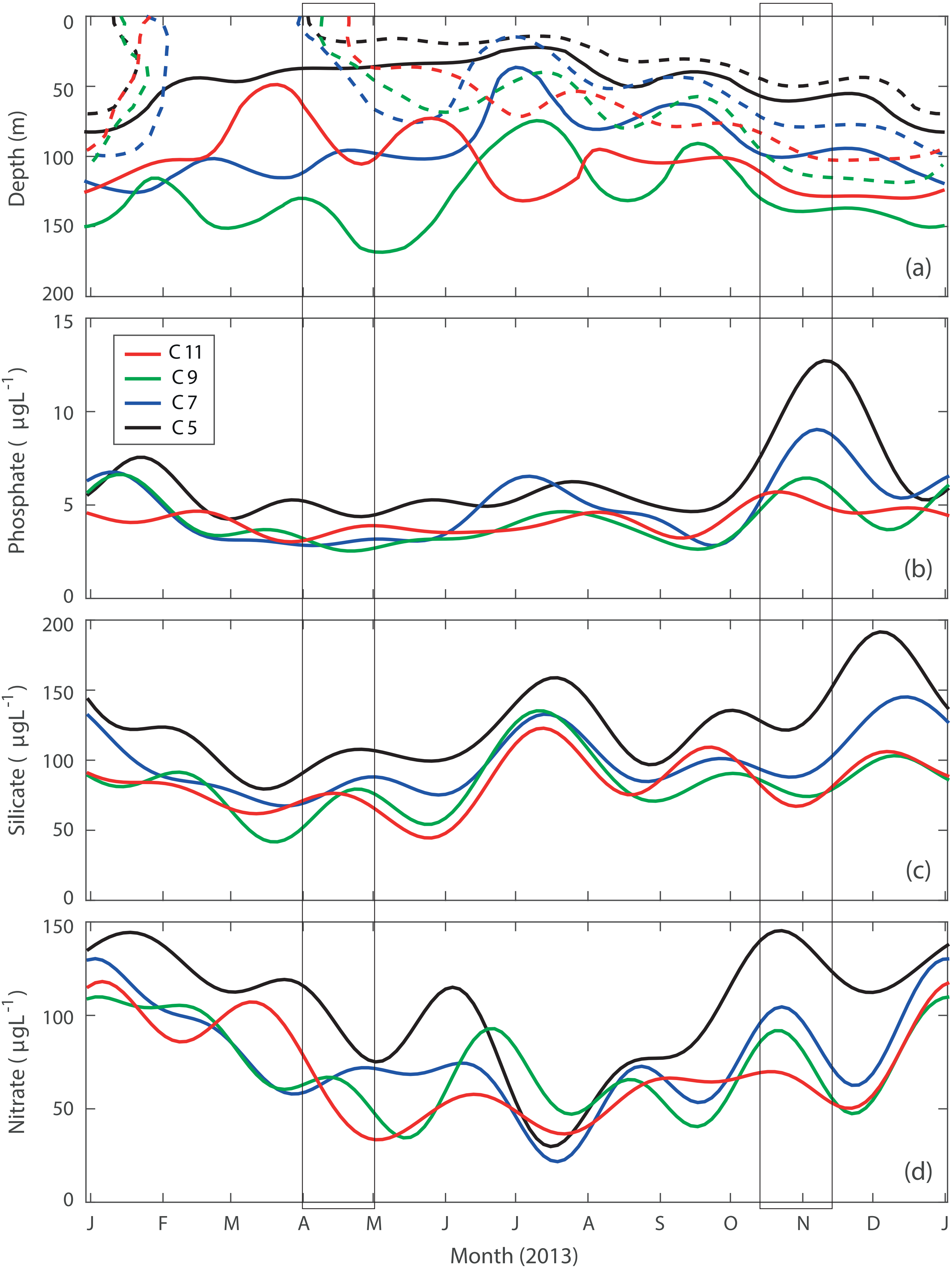

Depth (m)
(a)
Phosphate (µgL-1)
C 11
C 9
C 7
C 5
(b)
Silicate (µgL-1)
(c)
Nitrate (µgL-1)
(d)
J F M A M J J A S O N D J
Month (2013)

Figure 7.

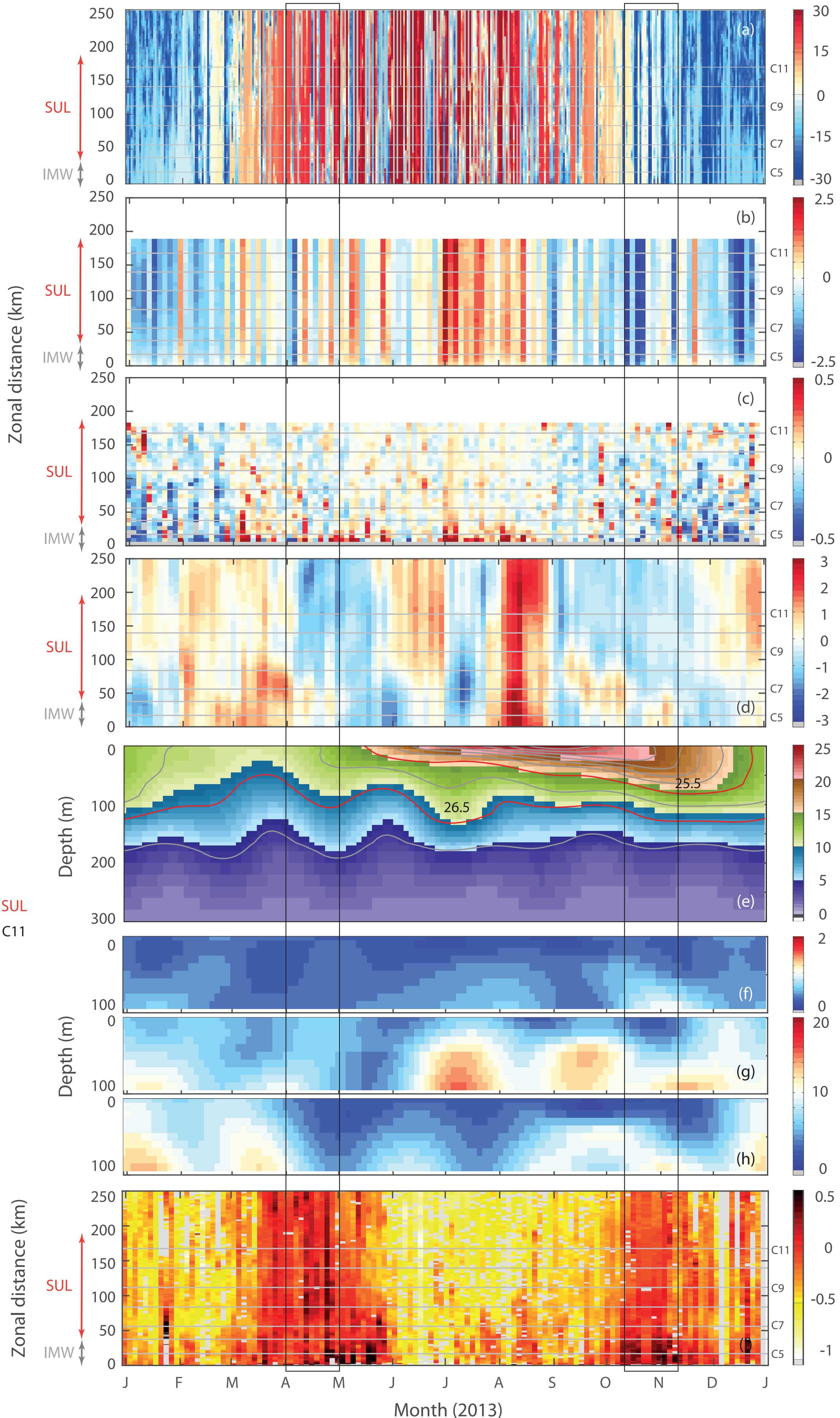

(a)
(b)
(c)
(d)
(e)
(f)
(g)
(h)
Zonal distance (km)
Depth (m)
SUL
IMW
C11
C9
C7
C5
26.5
25.5
J
F
M
A
M
J
J
A
S
O
N
D
J
Month (2013)

Figure 8.

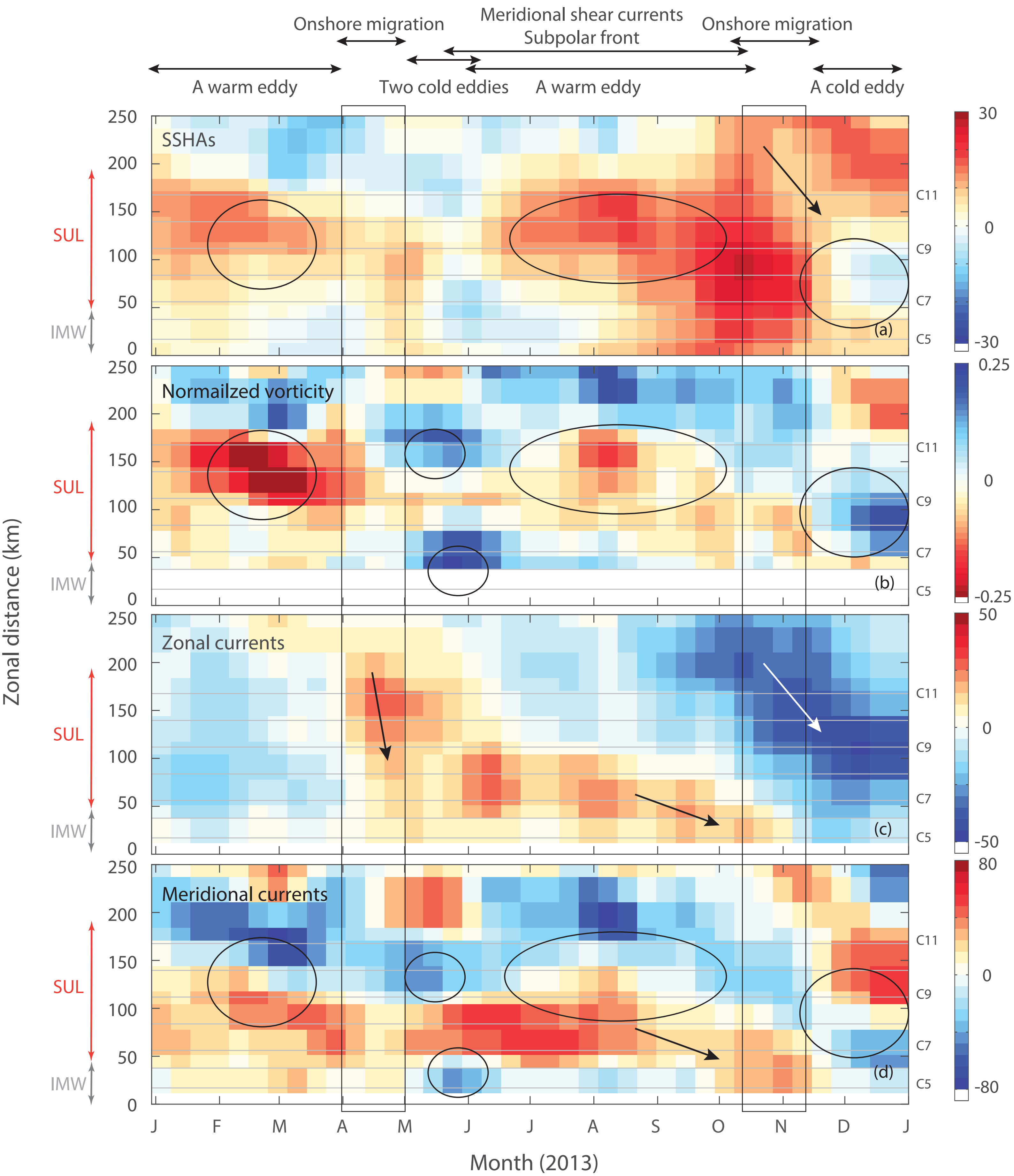

Onshore migration
Meridional shear currents
Subpolar front
Onshore migration
A warm eddy
Two cold eddies
A warm eddy
A cold eddy
SSHAs
(a)
Normailzed vorticity
(b)
Zonal currents
(c)
Meridional currents
(d)
Zonal distance (km)
SUL
IMW
C11
C9
C7
C5
250
200
150
100
50
0
30
0
-30
0.25
0
-0.25
50
0
-50
80
0
-80
J F M A M J J A S O N D J
Month (2013)

Figure 9.

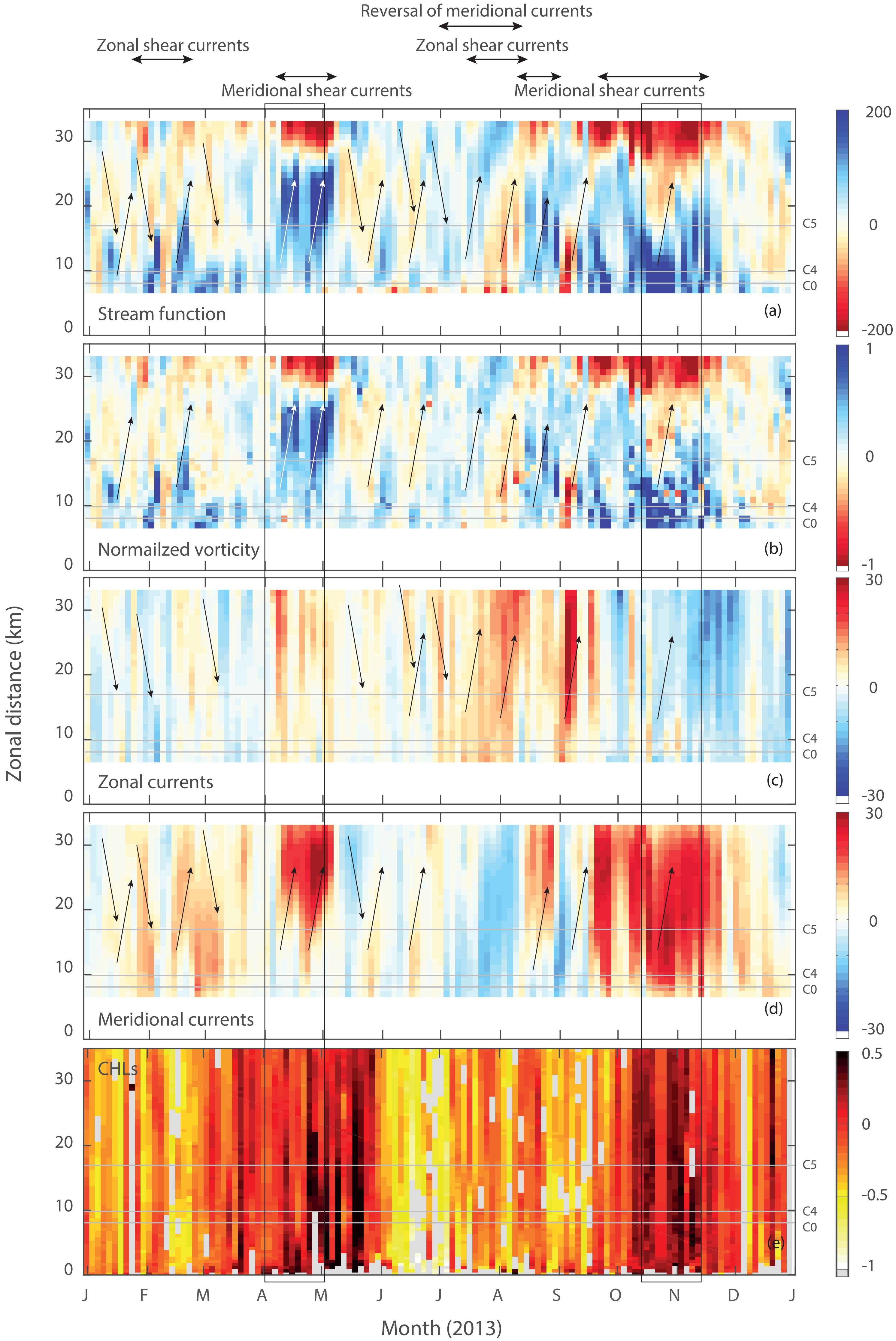

Reversal of meridional currents
Zonal shear currents
Zonal shear currents
Meridional shear currents
Meridional shear currents
Stream function
(a)
Normailzed vorticity
(b)
Zonal currents
(c)
Meridional currents
(d)
CHLs
(e)
C5
C4
C0
200
0
-200
1
0
-1
30
0
-30
30
0
-30
0.5
0
-0.5
-1
Zonal distance (km)
0
10
20
30
J
F
M
A
M
J
J
A
S
O
N
D
J
Month (2013)

Figure 10.

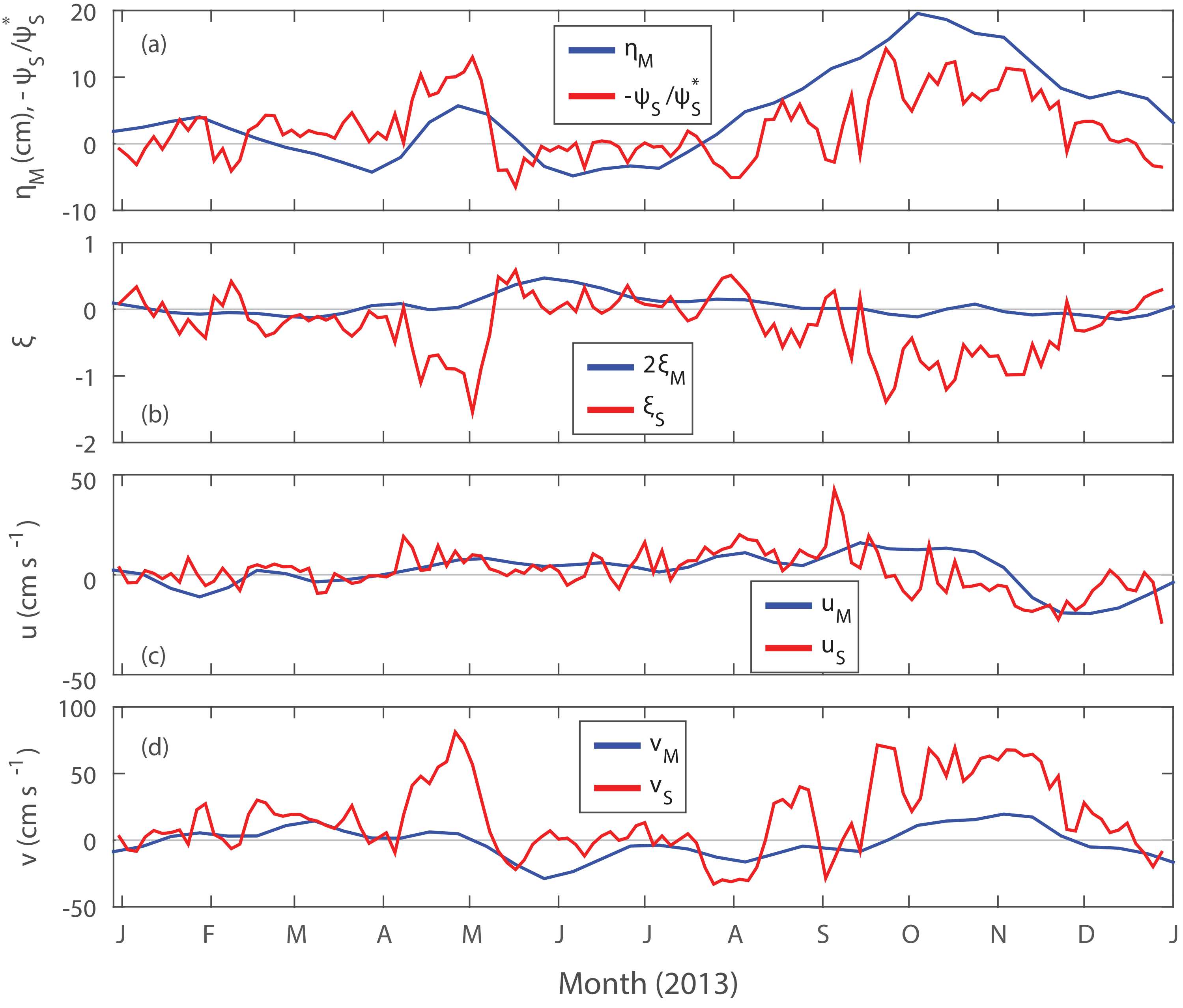

(a)
(b)
(c)
(d)
η_M (cm), $-\psi_S/\psi_S^*$
η_M
$-\psi_S/\psi_S^*$
ξ
$2\xi_M$
ξ_S
u (cm s^{-1})
u_M
u_S
v (cm s^{-1})
v_M
v_S
J F M A M J J A S O N D J
Month (2013)

Figure 11.

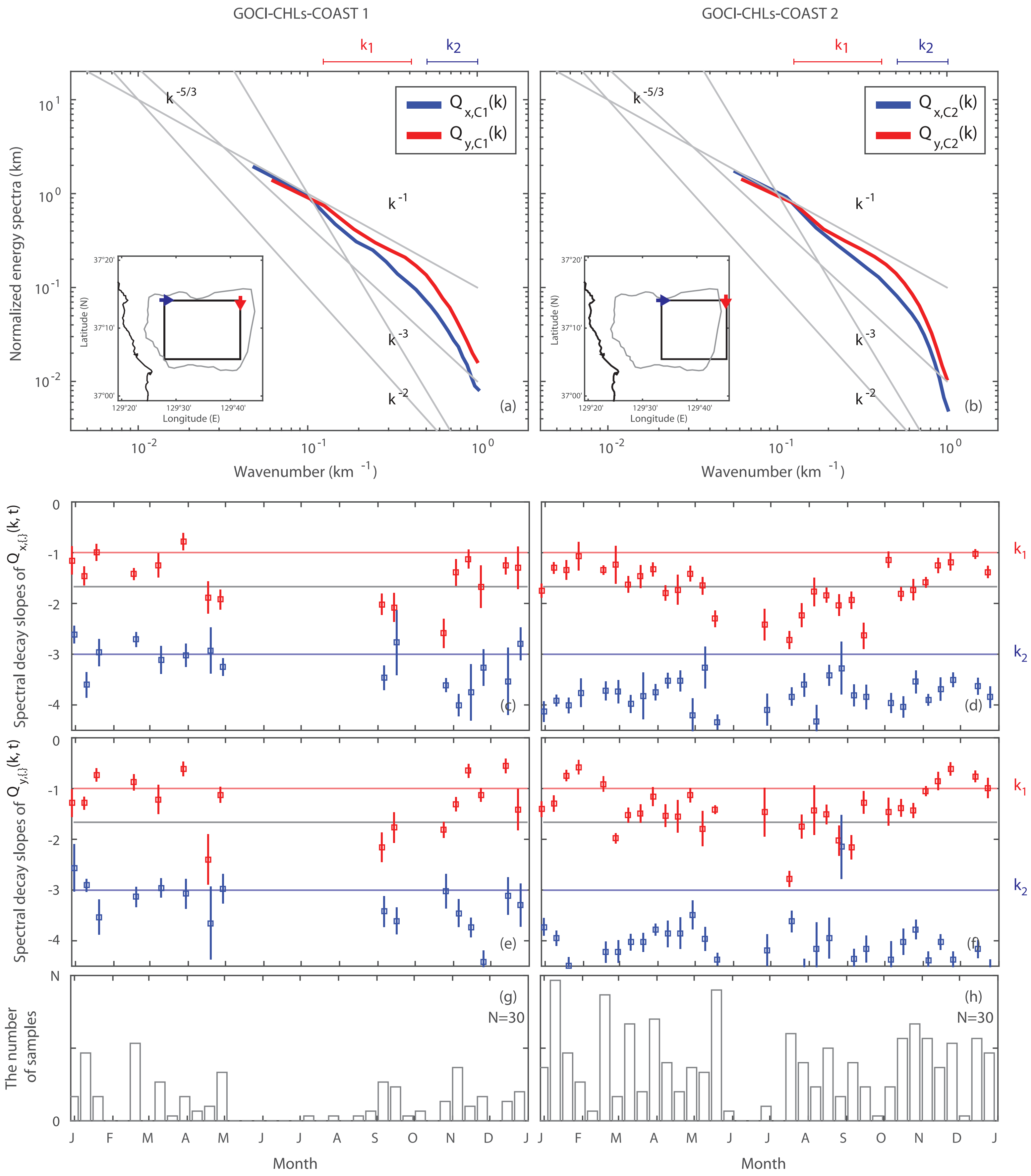

GOCI-CHLs-COAST 1
GOCI-CHLs-COAST 2
k1
k2
k -5/3
k -1
k -3
k -2
Q x,C1(k)
Q y,C1(k)
Q x,C2(k)
Q y,C2(k)
Normalized energy spectra (km)
Wavenumber (km -1)
Latitude (N)
Longitude (E)
37°20'
37°10'
37°00'
129°20'
129°30'
129°40'
(a)
(b)
Spectral decay slopes of Q x,{.}(k, t)
Spectral decay slopes of Q y,{.}(k, t)
(c)
(d)
(e)
(f)
The number of samples
(g)
N=30
(h)
N=30
J F M A M J J A S O N D J
Month

Figure 12.

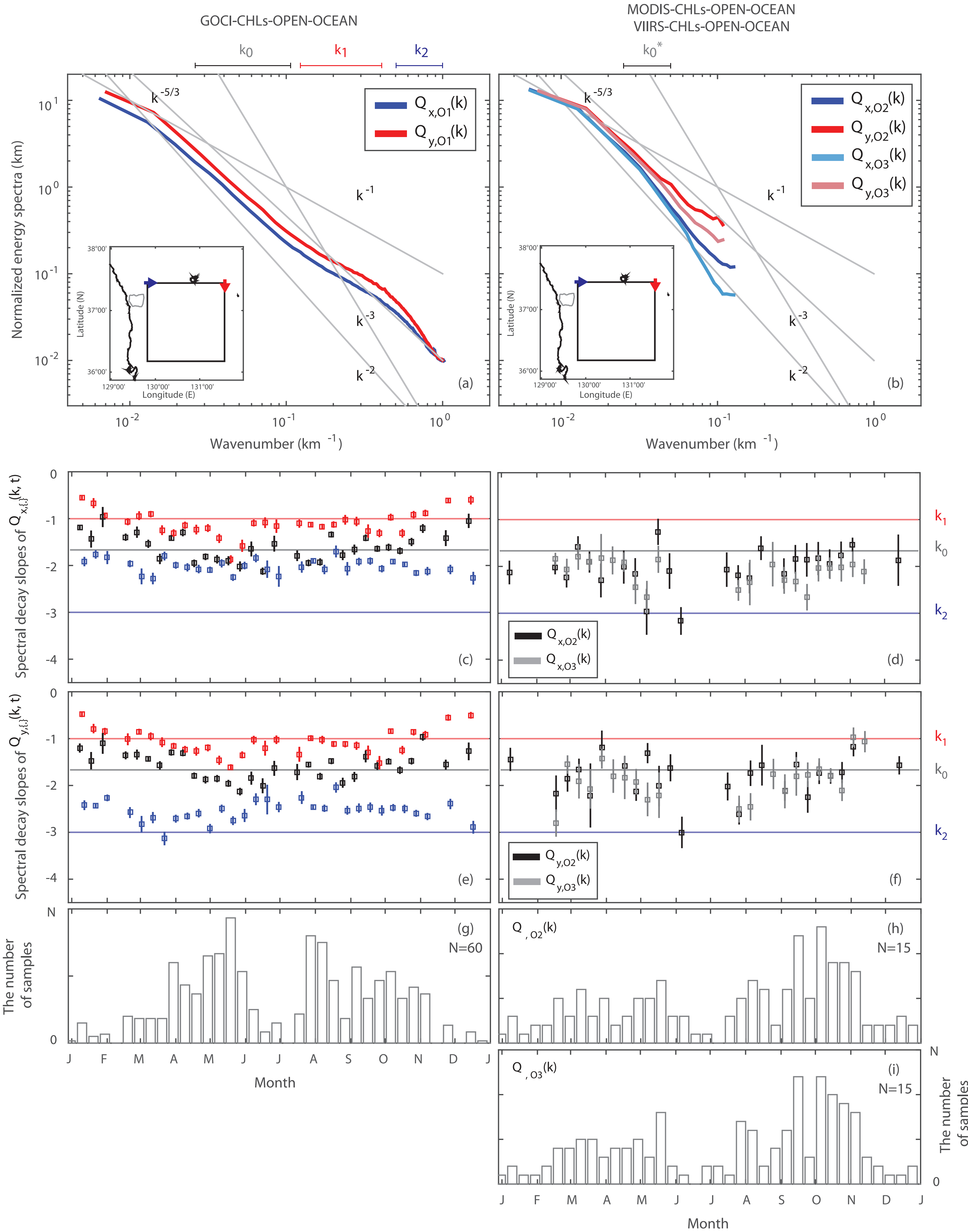

GOCI-CHLs-OPEN-OCEAN
MODIS-CHLs-OPEN-OCEAN
VIIRS-CHLs-OPEN-OCEAN
k0
k1
k2
k0*
k -5/3
k -1
k -3
k -2
Q x,O1(k)
Q y,O1(k)
Q x,O2(k)
Q y,O2(k)
Q x,O3(k)
Q y,O3(k)
Normalized energy spectra (km)
Wavenumber (km -1)
Latitude (N)
Longitude (E)
(a)
(b)
(c)
(d)
(e)
(f)
(g)
(h)
(i)
Spectral decay slopes of Q x,{.}(k, t)
Spectral decay slopes of Q y,{.}(k, t)
The number of samples
N=60
N=15
Q , O2(k)
Q , O3(k)
Month
J F M A M J J A S O N D J

Figure 13.

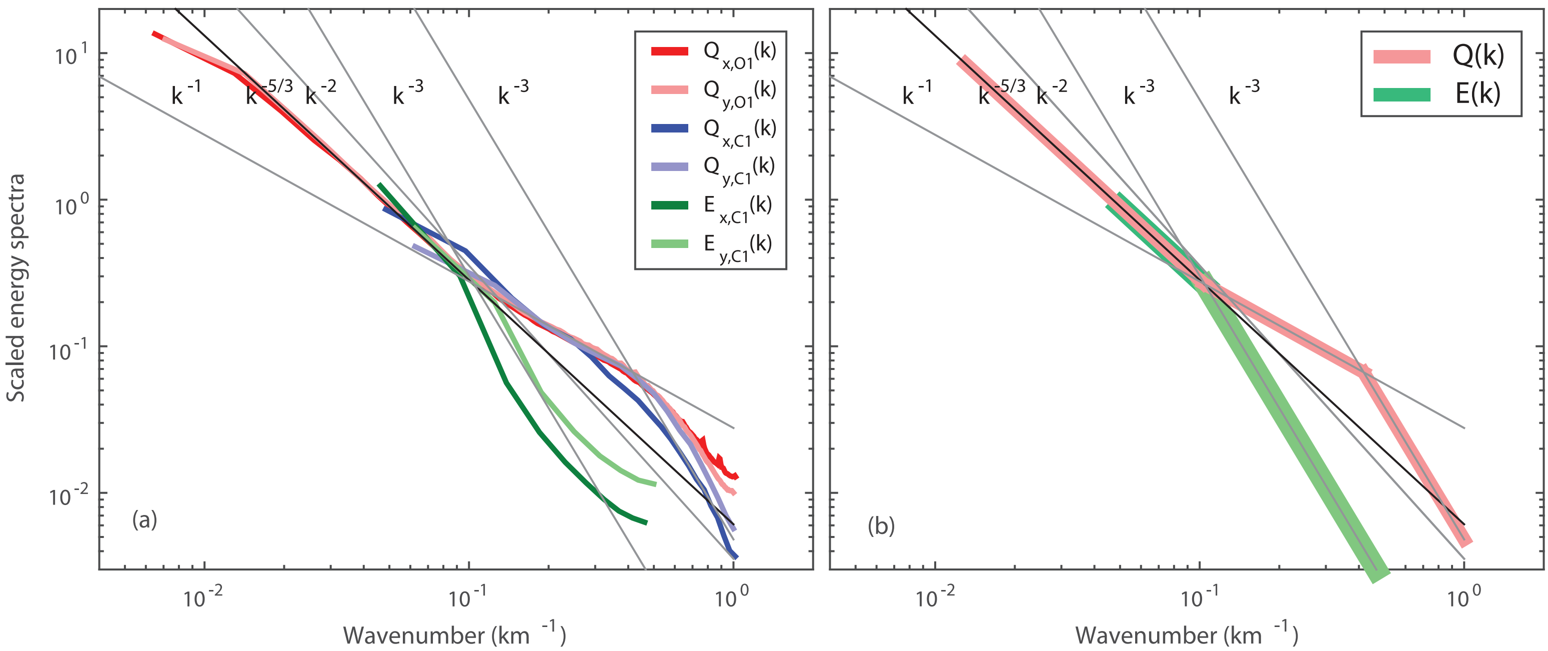

Scaled energy spectra
10^1
10^0
10^{-1}
10^{-2}
k^{-1}
$k^{-5/3}$
k^{-2}
k^{-3}
k^{-3}
$Q_{x,O1}(k)$
$Q_{y,O1}(k)$
$Q_{x,C1}(k)$
$Q_{y,C1}(k)$
$E_{x,C1}(k)$
$E_{y,C1}(k)$
(a)
10^{-2}
10^{-1}
10^0
Wavenumber (km^{-1})
k^{-1}
$k^{-5/3}$
k^{-2}
k^{-3}
k^{-3}
Q(k)
E(k)
(b)
10^{-2}
10^{-1}
10^0
Wavenumber (km^{-1})

Figure A1.

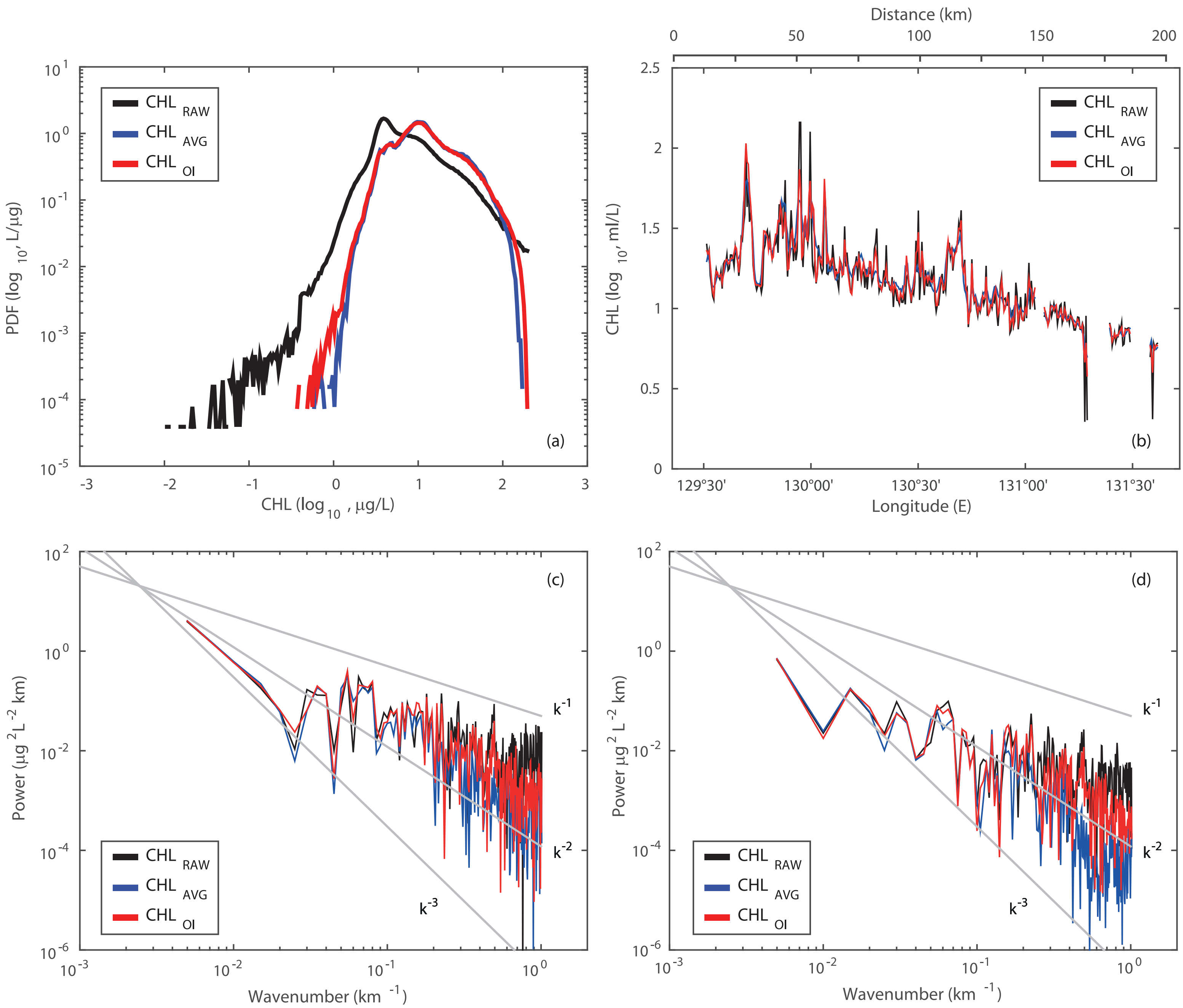

(a)
PDF ($\log_{10}$, L/μg)
CHL ($\log_{10}$, μg/L)
CHL_{RAW}
CHL_{AVG}
CHL_{OI}
(b)
Distance (km)
CHL ($\log_{10}$, ml/L)
Longitude (E)
129°30'
130°00'
130°30'
131°00'
131°30'
(c)
(d)
Power (μg^2 L^{-2} km)
Wavenumber (km^{-1})
k^{-1}
k^{-2}
k^{-3}

Figure B1.

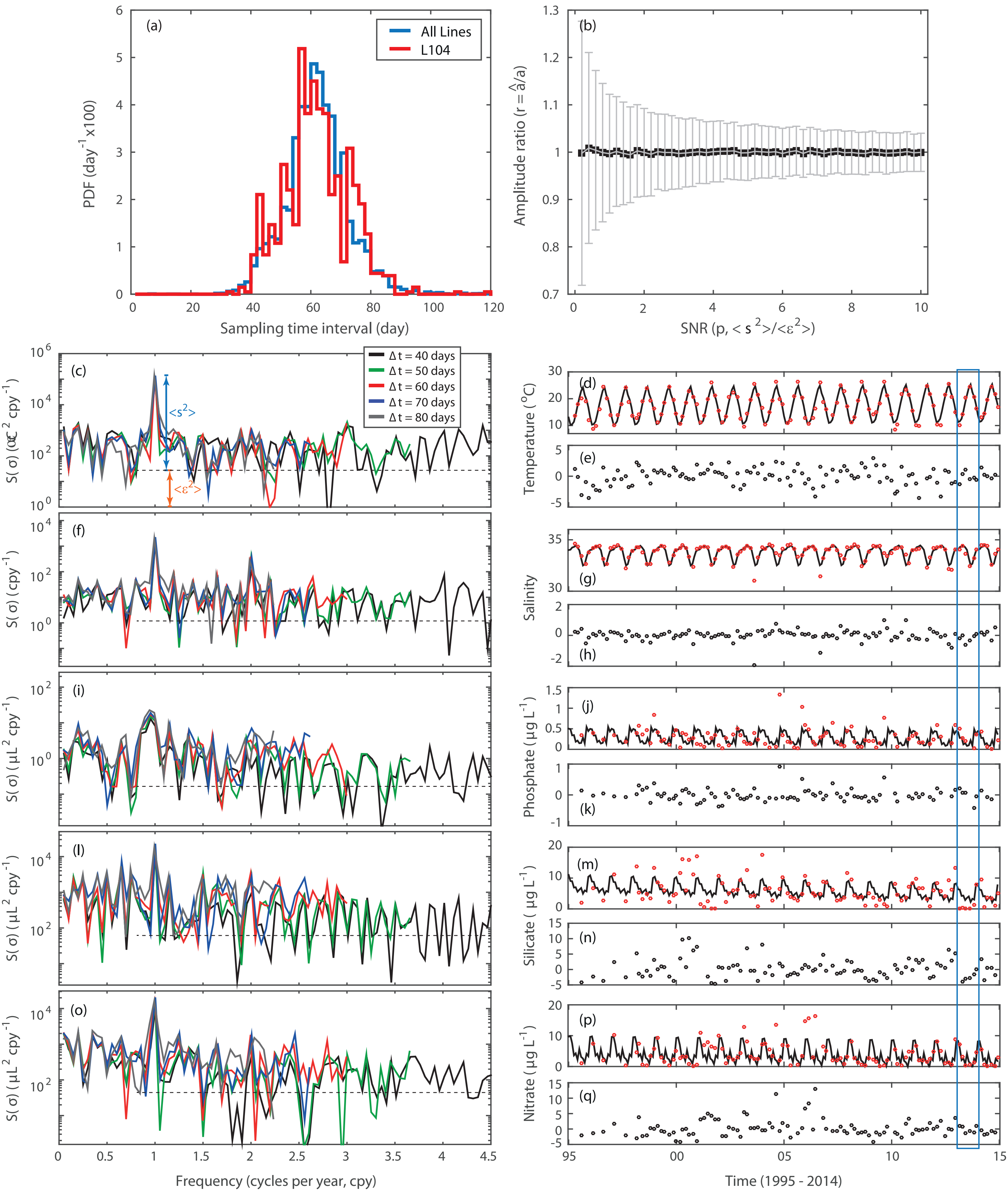

(a)
All Lines
L104
PDF (day^{-1} x100)
Sampling time interval (day)
(b)
Amplitude ratio ($r = \hat{a}/a$)
SNR (p, $\langle s^2 \rangle / \langle \varepsilon^2 \rangle$)
(c)
Δ t = 40 days
Δ t = 50 days
Δ t = 60 days
Δ t = 70 days
Δ t = 80 days
$\langle s^2 \rangle$
$\langle \varepsilon^2 \rangle$
S(σ) (cpy^{-1})
S(σ) (μL^2 cpy^{-1})
(d)
(e)
Temperature (°C)
(f)
(g)
(h)
Salinity
(i)
(j)
(k)
Phosphate (μg L^{-1})
(l)
(m)
(n)
Silicate (μg L^{-1})
(o)
(p)
(q)
Nitrate (μg L^{-1})
Frequency (cycles per year, cpy)
Time (1995 - 2014)